University of Zurich[UZH]

Modelling and Constraining Supraglacial Discharge, Channel Incision and Ice Cliff Backwasting on a Debris-Covered Glacier

GEO 511 Master's Thesis

Author
Céline Walker
17-722-877

Supervised by
Prof. Dr. Andreas Vieli
Boris Ouvry

Faculty representative
Prof. Dr. Andreas Vieli

08.06.2023
Department of Geography, University of Zurich

Table of Content

Abstract

Understanding the behaviour of debris-covered glaciers is essential for estimating their mass balances. As opposed to the expected insulating factor of debris, recent studies have observed debris-covered glaciers to have similar melt rates as clean ice glaciers. Melt hotspots on the glacier surface, such as ice cliffs, are assumed to cause these high melt rates. Their formation is investigated on the debris-covered Zmuttgletscher in Valais, Switzerland. The evolution of two cross-sections with differently oriented ice cliffs have been observed, measuring channel incision and ice cliff backwasting. The incision of the supraglacial channel in horizontal direction was detected to be 1.5 to 2 times larger than incision in vertical direction. Since the incision rate is higher than sub-debris ablation, the ice along the channel is constantly undercut. This process is observed to form ice cliffs, which follow the undercut channel. These determinations were contextualised with supraglacial discharge, which was modelled on the basis of an enhanced temperature index model and calibrated to ablation rates measured over a period of 41 days in summer 2022. Both sub-debris ablation rate and supraglacial discharge show distinct diurnal variations. An attempt to model supraglacial incision rates indicates that both heat dissipation and stream water temperature are needed to constrain incision from discharge.

List of Figures

List of Tables

1 Introduction

1.1 Motivation

Glaciers worldwide show negative mass balances (WGMS, 2021). The understanding of the melt behaviour of glaciers with climate change is relevant for various reasons such as sea level rise (Zemp *et al.*, 2019) or future water availability (Huss and Hock, 2018). Not all glaciers exhibit the same melt behaviour. Debris-covered glaciers can show less negative mass-balances than clean-ice glaciers (Mölg *et al.*, 2019). The debris cover can have an insulating or melt reinforcing effect. A very thin debris cover can increase melt due to a decreased albedo. However, a debris cover thickness of a few centimetres insulates since the energy fluxes responsible for ice melt first need to penetrate the debris layer. The insulating effect outweighs the effect of the lower albedo and melt rates decrease (Østrem 1959; Nicholson and Benn, 2006; Reid and Brock, 2010)).

The understanding of the melt behaviour of debris-covered glaciers and their incorporation in large scale glacier models is crucial, especially for regions where debris cover is substantial (Nicholson and Benn, 2006, 2013). In addition, understanding debris-covered glaciers becomes more important worldwide as the debris-covered glacierised area grows (Herreid and Pellicciotti, 2020; Compagno *et al.*, 2022). Despite their high abundance and increasing importance, debris-covered glaciers are often neglected in melt models (Hock *et al.*, 2019). A better understanding of debris-covered glaciers is therefore necessary.

Despite the insulating effect of the debris, debris-covered glaciers have also been observed to have similar melt rates as clean-ice glaciers (Kääb *et al.*, 2012; Sato *et al.*, 2021). This is described as the debris cover anomaly in literature (Bolch, Pieczonka and Benn, 2011; Kääb *et al.*, 2012). Possible explanations for the anomaly are high melt rates at melting hotspots, which are observed to be ice cliffs along supraglacial channels and in supraglacial ponds (King *et al.*, 2020; Sato *et al.*, 2021), as well as the glacier tongue (Ferguson and Vieli, 2020) and the debris emergence zone (Fyffe *et al.*, 2014). Often, these supraglacial forms, which show high ablation rates, are neglected in melt models of debris-covered glaciers (Ferguson and Vieli, 2020). To estimate the retreat on debris-covered glaciers, understanding the formation of these melt hotspots is key.

There are numerous studies on debris-covered glaciers (e.g. Kääb *et al.*, 2012; Mölg *et al.*, 2019; Nicholson *et al.*, 2021) and some on ice cliff formation (e.g. Sakai, Nakawo and Fujita, 2002; Sato *et al.*, 2021; Kneib *et al.*, 2023). However, none of the existing studies focus on channel formation and its influence on ice cliff formation on debris-covered glaciers.

This thesis presents a quantitative framework on the estimation of sub-debris ablation and supraglacial discharge and sets this into context of the formation of ice cliffs in two channel cross-sections on a debris covered glacier.

1.2 Research Gap and Aim of the Thesis

Little is known about the link between discharge and its incisive potential in supraglacial channels as well as its connection to the ice cliff backwasting along the channels on debris-covered glaciers. This thesis aims to connect an enhanced temperature index model with supraglacial discharge and the erosional processes along the supraglacial channels that can be divided into incision and ice cliff evolution. The following research questions are asked:

- Can supraglacial discharge be modelled based on an enhanced temperature-index glacier melt model (ETIM)?
- How does the diurnal supraglacial discharge vary and how is it related to the incision?
- Is there a connection between supraglacial channel incision and ice cliff backwasting?

1.3 Scientific Background

1.3.1 Abundance of Debris-Covered Glaciers

20% of earth's glaciers which are larger than 2 km² are debris-covered on more than 7% of their area. Another 59% of all glaciers show at least some debris cover (Herreid and Pellicciotti, 2020). Altogether, an area of 26'000 km² can be classified as debris-covered glaciers (Scherler, Wulf and Gorelick, 2018). Debris-covered glaciers occur all over the world. Regions with a highest abundance of debris-covered glaciers are Greenland, Alaska and High Mountain Asia. Also the Caucasus and Middle East and New Zealand show a high proportion of debris-covered glaciers (Scherler, Wulf and Gorelick, 2018; Herreid and Pellicciotti, 2020). With ongoing climate change, these numbers are expected to increase (Herreid and Pellicciotti, 2020; Compagno *et al.*, 2022).

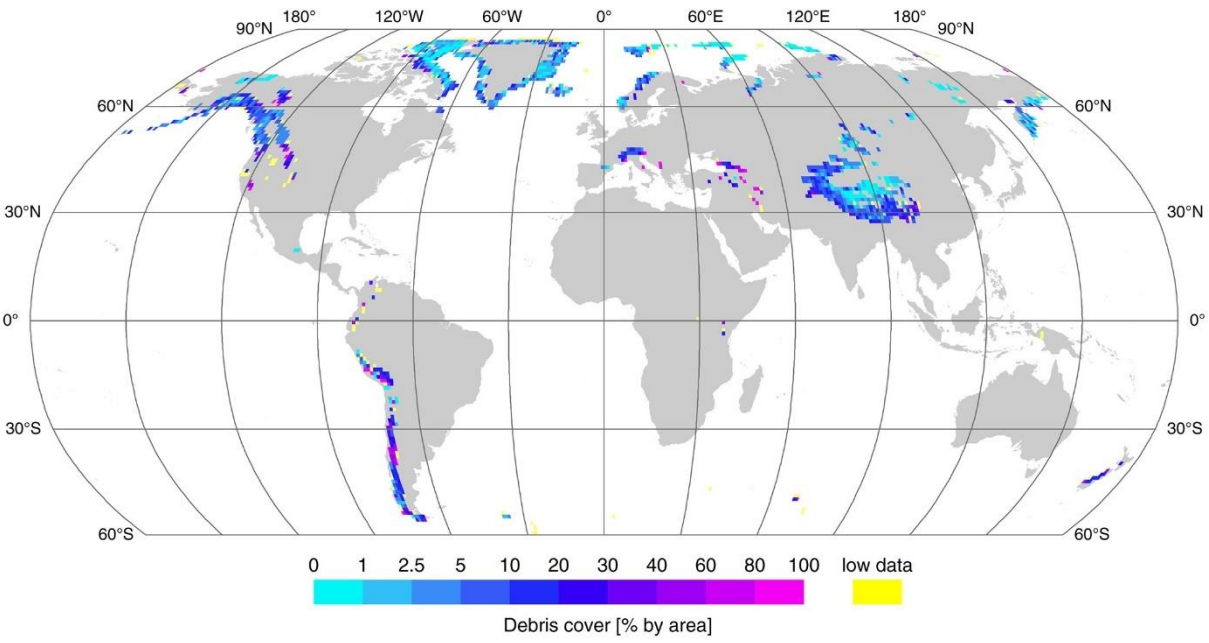

Figure 1: Worldwide abundance of debris-covered glaciers determined with Landsat 8 imagery by Scherler, Wulf and Gorelick (2018).

1.3.2 Influence of Supraglacial Debris Cover

A thin layer of debris can increase the ablation rate of a glacier, as the ablation is increased through a reduced albedo, capturing more of the shortwave radiation as energy to melt ice (Reid and Brock, 2010). The debris cover thickness where maximum melt rates are measured is often referred to as h_{eff}. If this thickness is exceeded, the debris cover starts to have an insulating effect and after a critical thickness h_{crit}, the melt rate of a debris-covered glacier is smaller than the one of a clean ice glacier (Figure 2; Østrem, 1959).

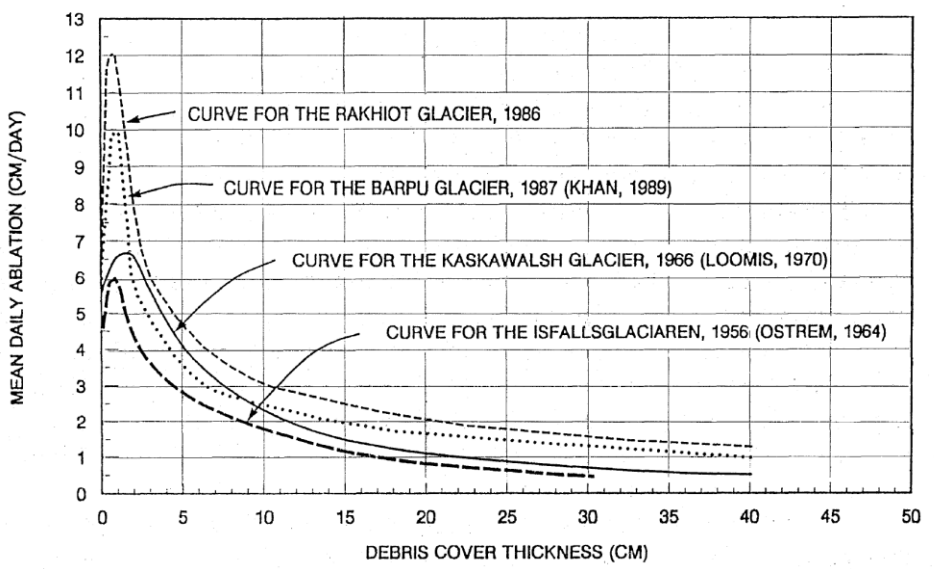

Figure 2: Østrem curves from measured mean melt rates and debris cover of various glaciers compiled by Mattson et al. (1993). The peak in the beginning of each curve shows h_{eff} and the debris cover starts being insulating (debris cover thickness > h_{crit}) for all glaciers between 2 and 3 cm.

Glaciers are not debris-covered from the beginning but get debris-covered over time. This can occur when their main mass gain is avalanches bringing in rocks from overlying steep rock walls (Ferguson and Vieli, 2020). The avalanches deposit in the accumulation zone and the deposits are gradually incorporated englacial as more ice is accumulated. In the ablation zone, the debris is melted out again and builds up at the surface. Additional debris can be deposited also directly in the ablation zone with rockfalls from unstable slopes (Ferguson and Vieli, 2020). With various debris cover thicknesses over the glacier surface, ablation can be heterogenous (Mihalcea *et al.*, 2008; Mölg *et al.*, 2020).

The length change of debris-covered glaciers is not strongly influenced by a current climate forcing but mainly by cold phases in the glacier's past (Ferguson and Vieli, 2020). Debris-covered glaciers' mass-balances are therefore strongly delayed in reacting to nowadays' warm climate and the response time is slower than for clean-ice glaciers. Furthermore, the length change is delayed in comparison to the volume change, as the ice velocity strongly decreases at the glacier tongue and the glacier loses height while the glacier length change is small (Ferguson and Vieli, 2020).

1.3.3 Ice Surface Ablation Models

Various ice melt models have been developed in the past. The Degree Day Model (DDM) is an empirical melt model based on the principle that ablation occurs if air temperatures are above the ice melting point. Below the melting point, there is no ablation (Hock, 2003). The days of positive degrees are multiplied by a factor that calibrates the temperatures to measured ablation and cumulated over the period of interest. The parameters of energy balance occurring at the ice surface are summarised in a Degree Day Factor, which is empirically determined. With a DDM the ice melt per day can be indicated, but it can also be used at an hourly basis indicating ablation per degree hour for a temporally high-resolution model. As temperature is dependent on elevation, this model melt shows a decrease in melt with increasing elevation. The advantage is the little data needed and the spatially and temporally highly resolved temperature data available (Hock, 2003; Lambrecht *et al.*, 2011).

The idea of enhanced temperature index models (ETIM) was presented by Pellicciotti *et al.* (2005) and is based on the DDM. In addition to the DDM, the ETIM incorporates shortwave incoming radiation. Similar as in the DDM, the processes of energy flux at the ice surface are represented by temperature and shortwave radiation and respective empirically determined factors. Similarly to the DDM, it usually indicates either the daily or the hourly melt rate.

Energy balance models (EBM) include the individual energy fluxes causing ice ablation (Gabbi *et al.*, 2014). The advantage of EBM is their physical basis which makes them applicable over a wide range of glaciers, as they are not depending on empirically calibrated factors. However, the disadvantage is their complexity and the numerous model input parameters that need to be measured.

Despite their simplicity, DDM and ETIM perform relatively well in comparison to more complicated physical energy balance models (Hock, 2003; Gabbi *et al.*, 2014).

This thesis aims to model supraglacial discharge and channel incision from an enhanced temperature index model. For this, an ETIM introduced by Pellicciotti *et al.* (2005) was extended by a factor to account for the insulating effect of debris-cover (Anderson and Anderson, 2016) and used to model ablation with an hourly resolution.

1.3.4 Supraglacial Melt Hotspots

Despite the insulating effect of thick debris layers, melt rates similar to clean-ice glaciers have been found on debris-covered glaciers (Kääb *et al.*, 2012; Gardelle *et al.*, 2013). It is generally assumed that these high melt rates result from melt hotspots. Melt hotspots on debris-covered glaciers are ice cliffs, supraglacial ponds or channels (Anderson *et al.*, 2021; Kneib, miles, *et al.*, 2021; Sato *et al.*, 2021) but also the debris emergence zone (Fyffe *et al.*, 2014). Overall, these are melt hotspots on the glacier where debris cover is comparably thin and the melt-amplifying effect of the thin debris layer enhances the melt rate. This comparably high melt rate at ice cliffs and at glacier ponds on debris-covered glaciers is often referred to as backwasting (e.g. Reid and Brock, 2014; Steiner *et al.*, 2015; Buri *et al.*, 2016).

Ice cliff formation and persistence are a result of ponds and supraglacial channel incision (Mölg *et al.*, 2019; Kneib, E. S. Miles, *et al.*, 2021). Ponds have been observed to form on surface depressions or slowly flowing parts of the glacier (Röhl, 2008; Kneib *et al.*, 2023). Ice cliff density is not determined by current climatic conditions but rather by the surface velocity and the state of the

glacier, and their occurrence decreases with distance to streams and ponds (Kneib *et al.*, 2023). However, ice cliffs can also be found away from streams or ponds. In these cases, they often used to be at a channel but backwasted away from streams (Kneib *et al.*, 2023).

Debris-covered glaciers can be differentiated into two states, one where debris cover is thick with a high density of ice cliffs that are pond-originated. In the other state, debris cover is comparably thin, ice cliff density is lower and ice cliffs are mainly stream-influenced (Kneib *et al.*, 2023). The appearance of these supraglacial streams have been found to be confined by lateral moraines (Mölg *et al.*, 2020; Kneib *et al.*, 2023). At the glacier tongue, often a high density of crevasse-originated ice cliffs can be found which form where there are high surface velocities (Kneib *et al.*, 2023).

The contribution of ice cliff backwasting to the total ablation of ice cliffs has been investigated in several studies. Buri *et al.* (2016) developed a grid-based model of ice cliff backwasting based on UAV DEMs using a model including long- and shortwave radiation. With their analysis they could support the argument of a high melt rate of supraglacial ice cliffs and show that the aspect of ice cliffs is important for their backwasting behaviour and could account for the complex surfaces of ice cliffs. Anderson *et al.* (2021) systematically measured ice cliff backwasting and came to similar findings that the ice cliff ablation fraction is larger than the ice cliff area fraction on the tongue of a debris-covered glacier in Alaska. Sato *et al.* (2021) observed the interannual evolution and distribution of ice cliffs and found out that interannual persisting ice cliffs are more often north-facing, and that long term surface elevation changes correlate with ice cliff density. They often develop from supraglacial meltwater channels, allowing fast melt at the dirty cliffs. Another zone where ice cliffs can appear are areas where compression of the ice is high (Anderson *et al.*, 2021).

For the formation of ice cliffs, shortwave radiation as well as direct longwave radiation from adjacent debris-covered areas are determining factors. The slope of the ice cliffs varies with aspect. Systematically detected ice cliffs tend to be north oriented (Buri *et al.*, 2021; Sato *et al.*, 2021). South facing cliffs are rare as they show a too steep angle for debris to rest and are quickly covered with debris and vanish, whereas on the north facing slopes, a thin debris layer can be deposited and the cliff melts back (Sakai, Nakawo and Fujita, 2002).

Ferguson and Vieli (2020) included ice cliffs, supraglacial ponds, and streams in a melt model of debris-covered glaciers and found that including these features decreases the glacier response time and increases the melt rate to rates that have been observed in other studies. To better comprehend the melt behaviour of debris-covered glaciers, understanding the formation of these surface features is crucial.

The formation of ice cliffs is still in investigation (Steiner *et al.*, 2015; Buri *et al.*, 2021; Sato *et al.*, 2021; Kneib *et al.*, 2023). This thesis aims to bring together supraglacial discharge and its influence on channel incision and ice cliff formation. Existing studies do not investigate the relation between discharge, incision in supraglacial channels and the effect on ice cliff backwasting on debris-covered glaciers. However, there is a theoretical framework of Fountain and Walder (1998) physically describing the influence of discharge on channel incision, where they also address the specific case of supraglacial channel downcutting. Ogier *et al.* (2021) investigated erosion and discharge in the case of a supraglacial outburst flood and Clarke (2003) did similar work on a subglacial outburst flood. Research on supraglacial discharge was compiled by Pitcher and Smith (2019), however, they do not address discharge on debris-covered glaciers.

2 Field Site

For this thesis, ablation, discharge and ice cliff formation are observed and modelled in the lower of two supraglacial catchments on Zmuttgletscher. Ice cliffs in the lower catchment are small as they are in the formation process. This makes it ideal to study the relation between discharge, channel incision and ice cliff formation. The approximate mean altitude of the lower catchment is 2490 m a. s. l. (Swisstopo, 2023).

Zmuttgletscher is one of the glaciers that got increasingly debris-covered over time (Mölg *et al.*, 2019). The glacier ranges from ~2250 m a.s.l., where it terminates in a large ice cliff, to ~4000 m a. s. l., where it is surrounded by several peaks. It flows from south to north-east (Swisstopo, 2023). It has an area of ~16 km^2 and 36% of the glacier's surface are debris-covered (Mölg *et al.*, 2019).

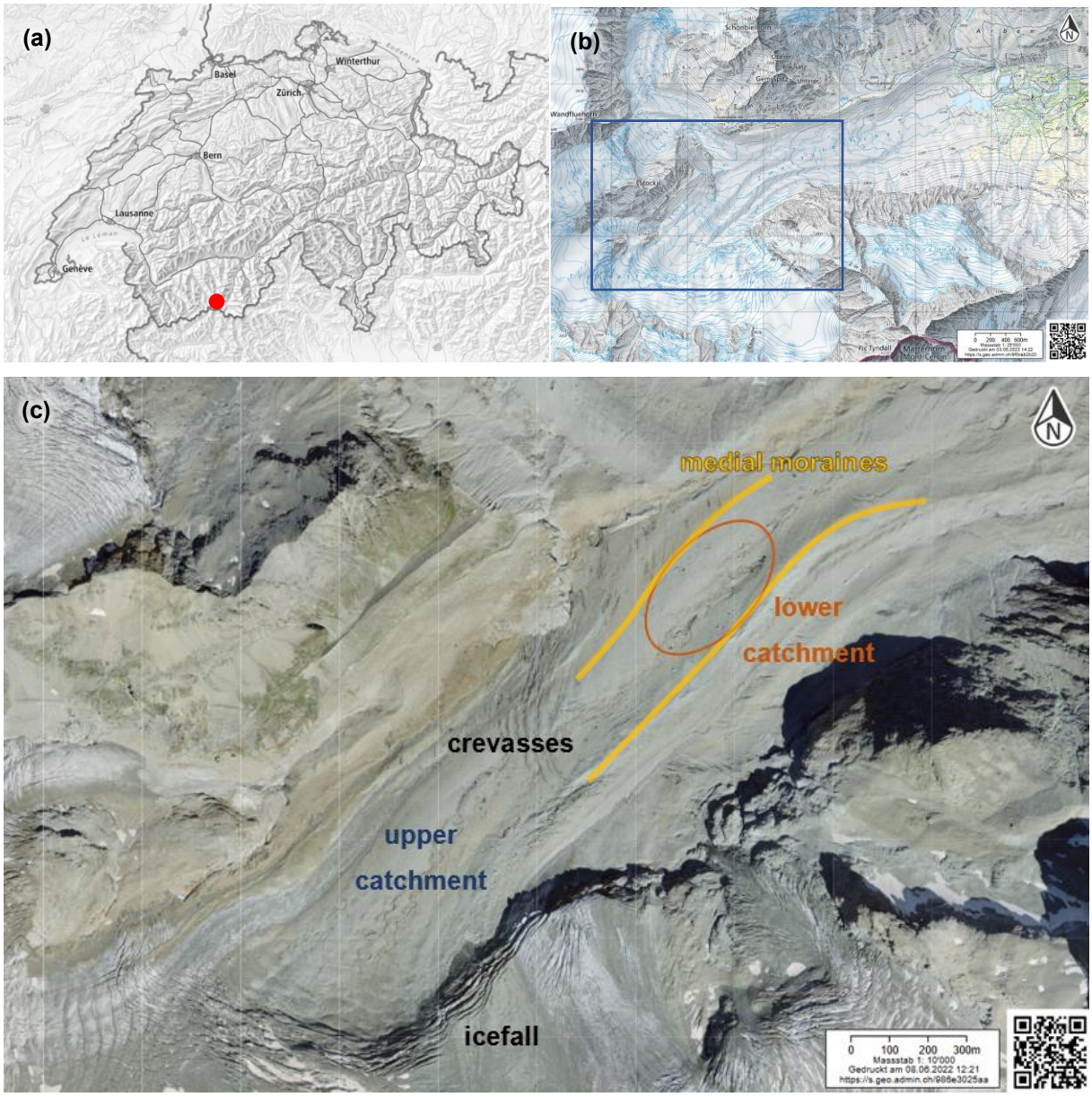

Figure 3: (a) The location of Zmuttgletscher in Switzerland. (b) A closer map from Zmuttgletscher and its surroundings in 2019 (source: Swisstopo, 2023). (c) Zmuttgletscher with the location of the two supraglacial catchments in an aerial image of 2021 (source: Swisstopo, 2023). The lower catchment is confined by two medial moraines (marked in yellow) and the upper is below the icefall. Between the two catchments, crevasses can be identified.

The top part of Zmuttgletscher is called Tiefenmattengletscher. Two tributaries, the Schönbielgletscher and the Stockjigletscher, flow into Zmuttgletscher at around 2500 m a. s. l. In the high altitudes of the glacier, clean ice can be found and the glacier and is not debris-covered. At an altitude of 2600 m a. s. l., the ice surface gets very steep and there is an icefall. Just above the icefall, the debris cover emerges. Underneath the icefall, the surface is again relatively flat. The debris cover varies over the surface of the glacier. As observed on other debris-covered glaciers (Kneib *et al.*, 2023), Zmuttgletscher shows two medial moraines parallel to the flow direction. Between the two medial moraines, a supraglacial valley has formed.

Two supraglacial catchments are identifiable on Zmuttgletscher. An upper supraglacial channel system forms in the area below the icefall (upper catchment). The focus of this thesis however lies on the catchment that emerges further down, constrained by the medial moraines in a supraglacial valley (lower catchment) (Figure 3). The channel systems in the two catchments show a similar build-up: Starting in various small waterflows, small channels are formed that turn into one large channel which eventually flows into a moulin. Along the channels, ice cliffs can be observed, showing different shapes depending on the aspect. Crevasses can be found between the two catchments, however there is no ice cliff formation observable at the crevasses. In 2022, there have not been any supraglacial ponds and ice cliffs are solely found along surface channels or melted back a few meters from the channels apart.

3 Methods

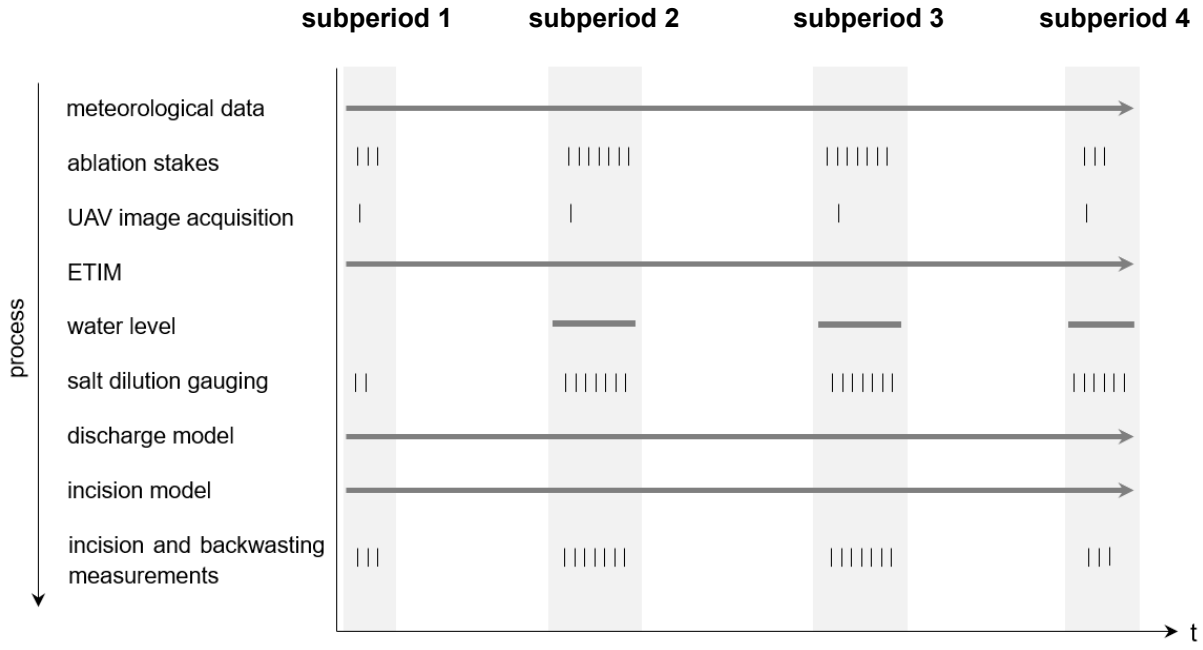

Figure 4: The thesis' structure, the in situ measurements and the models used visualised with time and their continuity.

Various in situ measurements were made in the lower supraglacial catchment (Figure 3) of Zmuttgletscher. The total measurement period is 41 days, starting on June 29, 2022, and ending on August 09, 2022. The measurements can be subdivided into meteorological measurements, ablation measurements, hydrological measurements and measurements on the erosional evolution of two cross-sections. In addition to the in situ field measurements, different models were used to connect them (Figure 4). Four bi-weekly field campaigns were made, in which high temporal resolution of measurements was achieved (Table 1). The field campaigns are further referred to as subperiods 1 to 4.

Table 1: The four field campaigns (subperiods) during the measurement period from June to August on Zmuttgletscher, when intensive measurements were made (Date format: yy-mm-dd).

	start date	end date
subperiod 1	22-06-29	22-06-30
subperiod 2	22-07-11	22-07-13
subperiod 3	22-07-25	22-07-28
subperiod 4	22-08-09	22-08-10

The parameters in Table 2 were used for the formulas presented in this chapter. The measured meltwater in the supraglacial channel was always close to 0°C, therefore, for physical constants, a water temperature of 0°C was assumed.

Table 2: Parameters and constants used in the formulas. The temperature-dependent variables apply to a temperature of 0°C and Manning's roughness coefficient applies to a smooth channel.

Variable	Parameter/constant	Value	Unit
g	Gravitational acceleration	9.81	$\mathrm{m\ s^{2}}$
ρ_i	Density of ice	900	$\mathrm{kg\ m^{-1}}$
ρ_w	Density of water	1000	$\mathrm{kg\ m^{-1}}$
k_w	Thermal conductivity of water	1000	$\mathrm{kg\ m^{-1}}$
μ	Kinematic viscosity of water	1.8×10^{-6}	$\mathrm{m^{2}\ s^{-1}}$
L_f	Latent heat of melting ice	3.33×10^{5}	$\mathrm{J\ kg^{-1}}$
ñ	Manning's roughness coefficient (clean ice channel)	0.01	$\mathrm{s\ m^{\frac{1}{3}}}$

3.1 Meteorological Measurements

The meteorological measurements were made continuous over the entire 41 days period. Air temperature, incoming shortwave radiation, precipitation, air pressure and humidity were measured. Albedo was measured next to the station with an *Apogee Albedometer*.

To keep the station in a stable and upright position, it was attached to a boulder on the glacier. Unfortunately, this boulder tilted and with it the station. Hence, it was moved to another boulder on July 25. The two stations are marked in Figure 5. Due to a malfunctioning pyranometer in the first two weeks, the shortwave incoming measurements from the meteorological station at the upper catchment (Figure 3) were used until July 11. The positions of the two meteorological stations are indicated in Figure 5.

3.2 Ablation

Cumulative ablation measurements were necessary to make to calibrate the melt model and hence determined the supraglacial discharge. It was measured in situ with ablation stakes during the 4 subperiods. Furthermore, in each subperiod, a digital elevation model (DEM) from UAV imagery was created, from which changes in the surface elevation could be detected. The meteorological data was combined with the measured ablation data in an enhanced temperature index model adapted for the debris covered Zmuttgletscher to receive a continuous ablation estimate over the entire measurement period.

3.2.1 Ablation Stakes

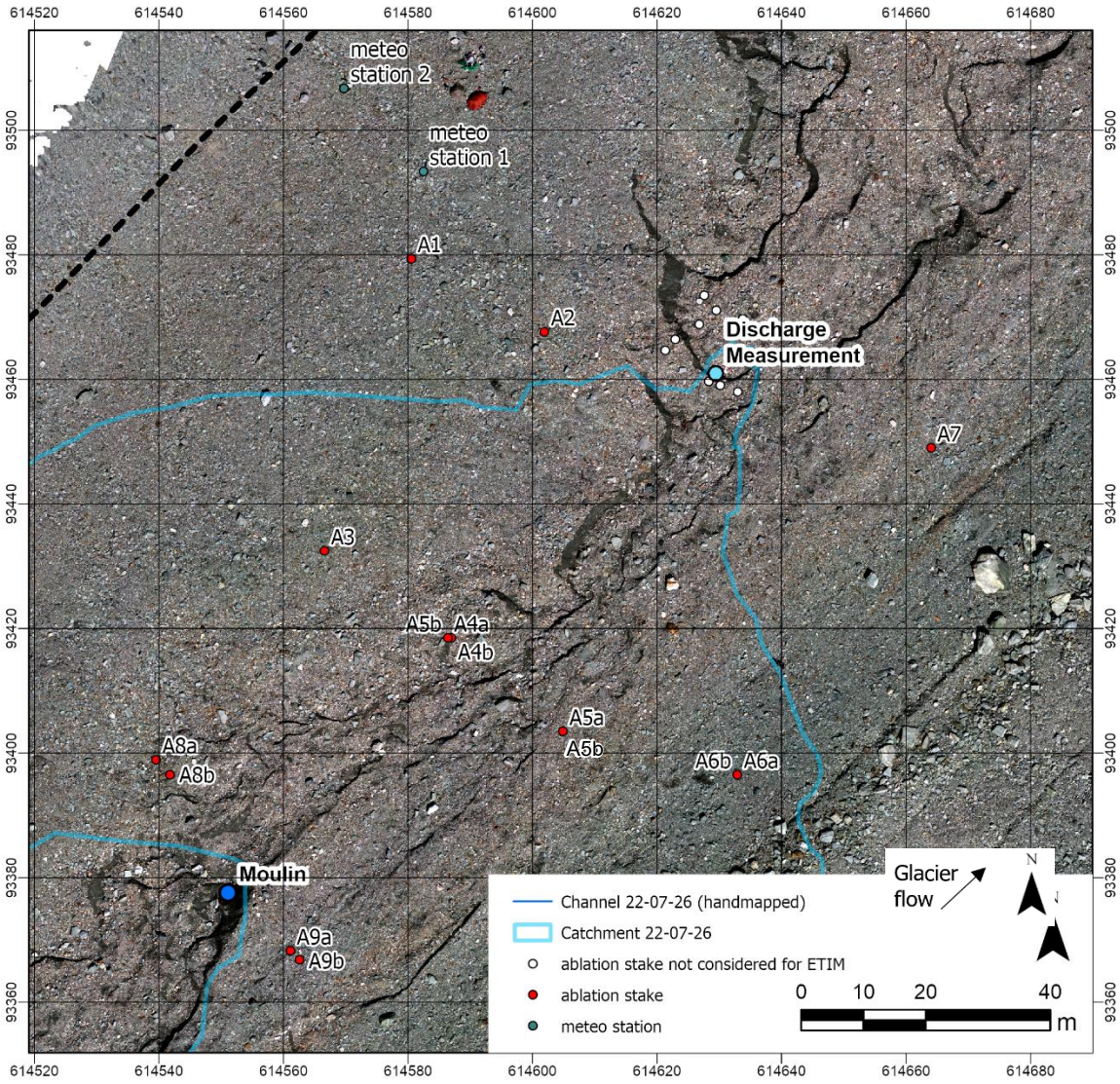

Figure 5: Setup of the ablation stake distribution around the supraglacial channel on Zmuttgletscher. Marked in red are the ablation stakes considered for the ETIM and in white the not considered ablation stakes (reference stakes and stakes influenced by channel erosion). The two meteo stations are also marked.

To measure cumulative surface ablation, 11 PVC stakes of 2m length were installed as ablation stakes around the supraglacial channel system to have a good representation of the area of

investigation (Figure 5). Additionally, 5 metal stakes, stabilised in rock piles, were installed close to the channel. These stakes were mainly used as references for the alignment of laser imagery (Chapter 3.4.2) of the area. Nevertheless, ablation was measured at these stakes too.

Measurements were taken in the morning and in the evening during each subperiod to observe the different ablation rates between night and day. Cumulative ablation was measured by putting an ablation disk over each stake and measure the height of the stake from the ablation disc. The difference between the initial height of the stake $h_{stake}(t_0)$, when it was put into the ice, to the moment of measurement $h_{stake}(t)$ was noted as cumulative ablation. To minimise measurement errors, the height was always measured on the orographic left side of the stake (Figure 6).

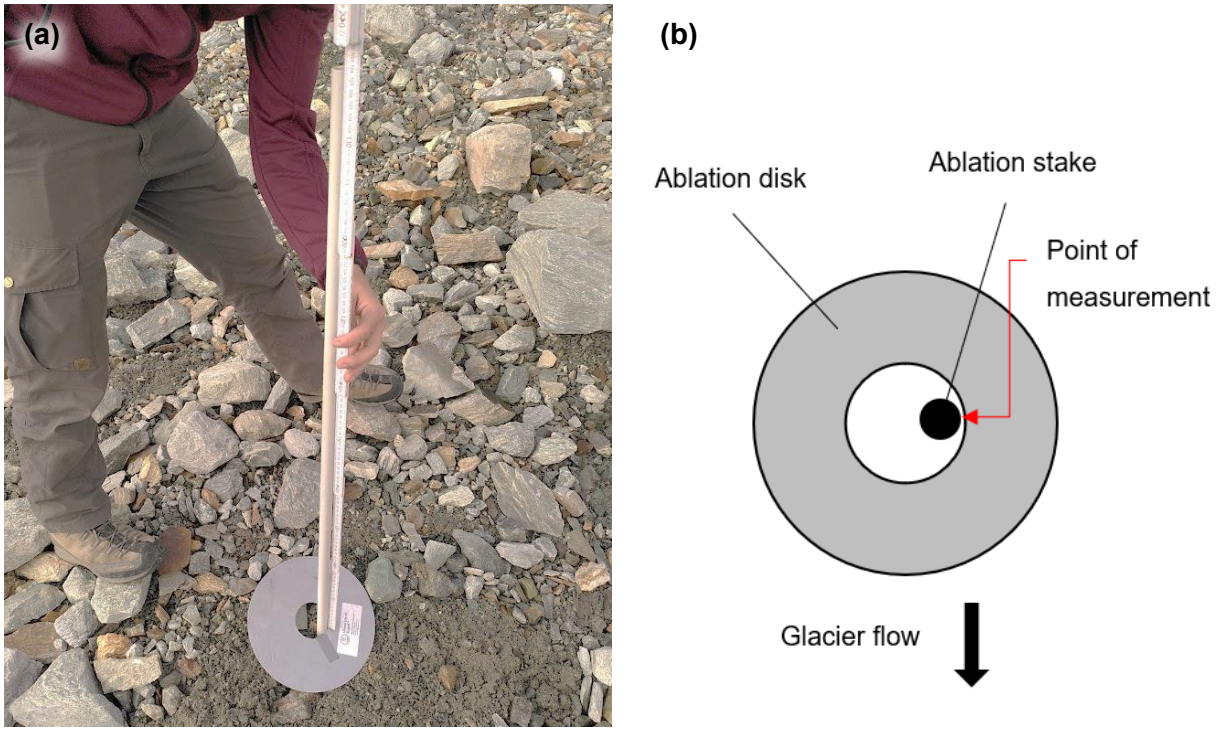

Figure 6: Measuring the ablation stake height with a measuring stick on the orographic left side of an ablation stake to determine the ablation. (a) Measuring in the field with a meter stick on the orographic left side of the ablation disc. (b) Schematic sketch of the measurement with the ablation disc.

The metallic reference stakes for the laser scans were not considered for the enhanced temperature index model (ETIM) (Chapter 3.2.3) as they were mostly stabilised by a pile of rocks which made a uniform measuring technique more difficult and the measurements less comparable. Furthermore, they were close to the channel and their melt rates were influenced by the channels, which was not desired for the ETIM.

After the first four weeks of measurements (until subperiod 3), some of the stakes had fallen out or were melted out by a large part. Thus, new ablation stakes were positioned next to the already installed ones. To differentiate the new with the already installed stakes, these new ones are indicated with *b* in Figure 5 and those that were installed in the beginning are marked with *a*. At the stakes without further indication with *a* or *b* (e.g. *A1*) measurements were taken throughout the entire period at the same stake and it was not replaced. To compare the measurements at the newly drilled stakes, the cumulative ablation of the prior stakes was added to the initial measurement of the new ones to compensate for the ice surface elevation loss since the beginning

of the measurements (e.g. from *A8b*, the previously measured cumulative ablation of *A8a* was added). The ablation measurements were fitted through y=0 on 22-06-30, which is when all meteorological measurements are available and the ETIM could start.

3.2.2 UAV Surface Elevation Difference

As an additional independent measurement to the ablation stakes, a digital elevation model (DEM) was produced from orthophotos from an unwomanned aerial vehicle (UAV) *Phantom 4 DJI V2.0* on June 29, July 12, July 26 and August 09. A real-time kinematic positioning (RTK) was used to georeference the UAV imagery with the Swiss national base reference station in Furi, Zermatt. The Swiss coordinate system CH1903 / LV03 was used. The compilation of the single images to an Orthophoto was done with the *Agisoft Metashape Professional* software. Based on the Orthophotos, DEMs were created with a spatial resolution of 2.4 cm -3.2 cm.

For the surface elevation differencing, a co-registration of the DEMs due to glacier flow was needed in a first step (Huber, McNabb and Zemp, 2020). The alignment was done with the spline transformation function in *ArcGIS* to bring the DEMs of July 11, July 26 and August 09 to the position of the first DEM.

As the glacier does not flow horizontally but also downwards along the slope, a correction for the surface elevation loss due to glacier downslope flow had to be made. The positions of 16 clearly identifiable points (in Figure 7 depicted as an ablation stake and a rock) on the glacier were marked on the first and last Orthophoto. The two positions per point were compared in the DEM of June 29 to determine the elevation difference along the slope. The average downslope movement of -0.27m was subtracted from the elevation difference. However, the standard deviation of 0.33m of the elevation difference is quite large.

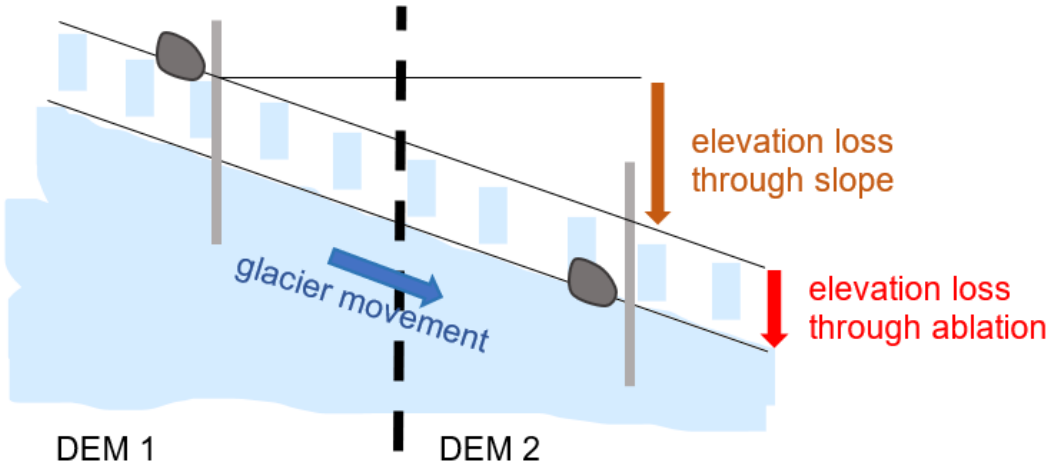

Figure 7: Downslope correction of the DEM with co-registration. The glacier flows downslope and therefore, every part moves to a lower elevation. If the surface elevation of DEM 2 is compared to the one in the DEM 1, a slope-caused elevation loss occurs.

Table 3: Total movement of glacier during the period of investigation with standard deviation and average surface ice-flow velocities in each direction. The timespan for the total movement is 41 days.

direction	total movement [m]	standard deviation for total movement [m]	average velocity [cm day^{-1}]
x (west-east)	1.35	0.16	3.292
y (south-north)	1.25	0.12	3.05
z (vertical)	-0.271	0.333	0.658

With the four DEMs aligned to the first one and corrected for the slope-caused elevation loss, the elevation differences between them were calculated. The catchment averaged ablation including the ice loss in the channel area. These values were compared to the mean ablation stake measurements. Additionally, melt rates of cliff area and of the surfaces not influenced by cliffs and channels were separately gathered from the DEM elevation differencing of the entire period.

3.2.3 Enhanced Temperature Index Model

The ablation rate was modelled with an enhanced temperature index model (ETIM) developed by Pellicciotti *et al.* (2005) for a clean ice glacier (Formula (1). The model was adapted for a debris-covered glacier (Chapter 3.2.4). The model was chosen as it uses relatively little measured input and only few parameters. At the same time, it shows good performance (Gabbi *et al.*, 2014). Furthermore, it fits the long-term ablation trend and represents diurnal variations well, which was desired for the discharge modelling described in Chapter 0. The model is based on the principle, that there is melt when temperatures are above the ice melting point T_0 and no melt when temperatures are below T_0. Temperature and incoming shortwave radiation are used as input parameters to model an hourly ablation rate (mm hour^{-1}):

$$\begin{aligned} &\text{if } T \leq T_0: && \dot{a}_c = 0 \\ &\text{if } T > T_0: && \dot{a}_c = F_T\,(T - T_0) + F_{SW}\,SW_{in}\,(1 - \alpha), \end{aligned} \tag{1}$$

where $\dot{a}_c$ is the ablation rate on a clean ice glacier, T is air temperature, T_0 the melting point of ice at $0°C$, SW_{in} the incoming shortwave radiation and. F_T (mm °C^{-1} h^{-1}) and F_{SW} (m^2 mm W^{-1} h^{-1}) are the T and SW_{in} factors, respectively. T and SW_{in} data were measured at the meteorological station. As the altitude within the catchment does not vary much (2995 – 2542 m a.s.l.), no correction with altitude was made and the same temperatures were assumed over the entire catchment. The used albedo $\alpha = 14.3 \pm 0.012$ was measured at the debris-covered glacier surface around the meteorological station and was equally adopted for the entire catchment. The hourly melt rate was modelled. Hence, all meteorological input data was set to an hourly interval using the mean value measured per hour.

3.2.4 Sub-Debris Ablation

The ETIM was conceptualised for clean-ice glaciers. As Zmuttgletscher is debris-covered, the ablation rate was extended by a debris insulating factor F_{ins} (Anderson and Anderson, 2016).

$$\begin{aligned} &\text{if } T \leq T_0: && \dot{a}_d = 0 \\ &\text{if } T > T_0: && \dot{a}_d = \dot{a}_c \, F_{ins} = F_T \, (T - T_0) + F_{SW} \, SW_{in} \, (1 - \alpha) \, \frac{D_0}{D + D_0} \end{aligned} \tag{2}$$

where $\dot{a}_d$ is the ablation rate on a debris-covered glacier (mm hour^{-1}), D_0 is determined by the Østrem curve (Østrem, 1959) and D the debris cover thickness. As ablation on clean ice was not measured on Zmuttgletscher in 2022, $D_0 = 0.1$ m determined by Farsky (2021, unpublished) on Zmuttgletscher in 2021 was used. An average debris cover thickness was chosen over a spatial interpolation as the measurements grid was not dense enough and uncertainties high and debris-cover thickness did not vary greatly (5 - 13 cm). Furthermore, the interest of the model lies on an average catchment meltwater contribution. The influence of small scale variations in debris-cover thickness should not influence the catchment averaged melt rate (Anderson *et al.*, 2021).

3.2.5 ETIM Parameter Calibration

The temperature and shortwave radiation parameters of the ETIM needed to be calibrated with the measured cumulative ablation with their respective factors (F_T and F_{SW}). The ablation measurements at the stakes were grouped into measurement cycles (i.e. morning and evening of every day measured) and the average ablation per measurement cycle was determined. As described in chapter 3.2.1, not all ablation stakes of the investigated area could be used.

The modelled ablation rate per hour was cumulated and fitted against the mean measured cumulative ablation. The best parameter combination of F_{SW} and F_T was found by fitting the model to the measurements with the non-linear least squared index (NLS). This index was used to find the parameter combination of the smallest residual sum of squares (RSS), which is calculated as:

$$RSS = \sum_{i=1}^{n} (x_{modelled} - x_{measured})^2 \tag{3}$$

The overall trend was modelled in a first step using the mean cumulative ablation of all measurement cycles. As starting parameters, the best fitting parameter combination used by Pellicciotti *et al.* (2005) of $F_T = 0.06$ and $F_{SW} = 0.0094$ was used. Fitting the ETIM to all mean cumulative ablation measurements, diurnal melt variations were badly depicted (Chapter 4.2.3). To improve the small-scale melt rate variation, the model was fitted to the subperiods. In Table 6, the RSS and parameter values for the NLS are summarised. For subperiod 1, no fit was made as the measurements were just started and uncertainties would be high.

For the representation of the daily cumulative pattern, the calibration for subperiod 4 showed the smallest RSS (Table 6) and was used for the further modelling. The sensitivity of the ETIM with different F_T and F_{SW} were analysed for the best fit.

3.3 Discharge

The discharge and its diurnal variations were of interest to observe, how it is related to the incision of the channel and the backwasting of the ice cliff. The discharge was determined with two different methods, which were later combined. The first is salt dilution gauging. In this method, a salt dilution tracer is used and the change in electrical conductivity in the channel is measured. The second is measuring water pressure with a pressure sensor to determine the water level. Both methods were combined with a rating curve (e.g. Collier, 2016) for a continuous discharge. The resulting discharge was used to model a continuous discharge from the ETIM and followingly an ice incision rate over time.

3.3.1 Salt Dilution Gauging

As the supraglacial channel on a debris-covered glacier flows turbulent, discharge was measured with salt-dilution gauging (Hubbard and Glasser, 2005). A well-mixed dilution of salt water was injected in the stream as a tracer. The volume of the dilution was known and noted, whereas the exact amount of salt added was not necessary to note, as a calibration was done for every measurement. However, the added salt amount lied between 20 and 60 grams. The volume injected in the investigated channel on Zmuttgletscher lied between 2 and 5l, depending on the visual estimation of the amount of water flowing, i.e. in the morning, there was less discharge and thus a smaller volume was injected.

Before each injection, the calibration between EC and the salt concentration was made. 10ml of the already mixed salt dilution was put in a vessel together with 1l of stream water. 100ml of stream water were put in a separate beaker. First, the background concentration of the stream water was measured in this beaker. From the 1l solution, 1 by 1 ml is injected into the beaker of 100ml of stream water. For every additional ml, the EC was noted until 10ml were added in total, which were enough measurements for the calibration (Figure 8).

For the calibration, the concentration was determined from the EC with a linear regression, where m is the slope of the regression and q the centre distance:

$$C_c = m\,EC + q \tag{4}$$

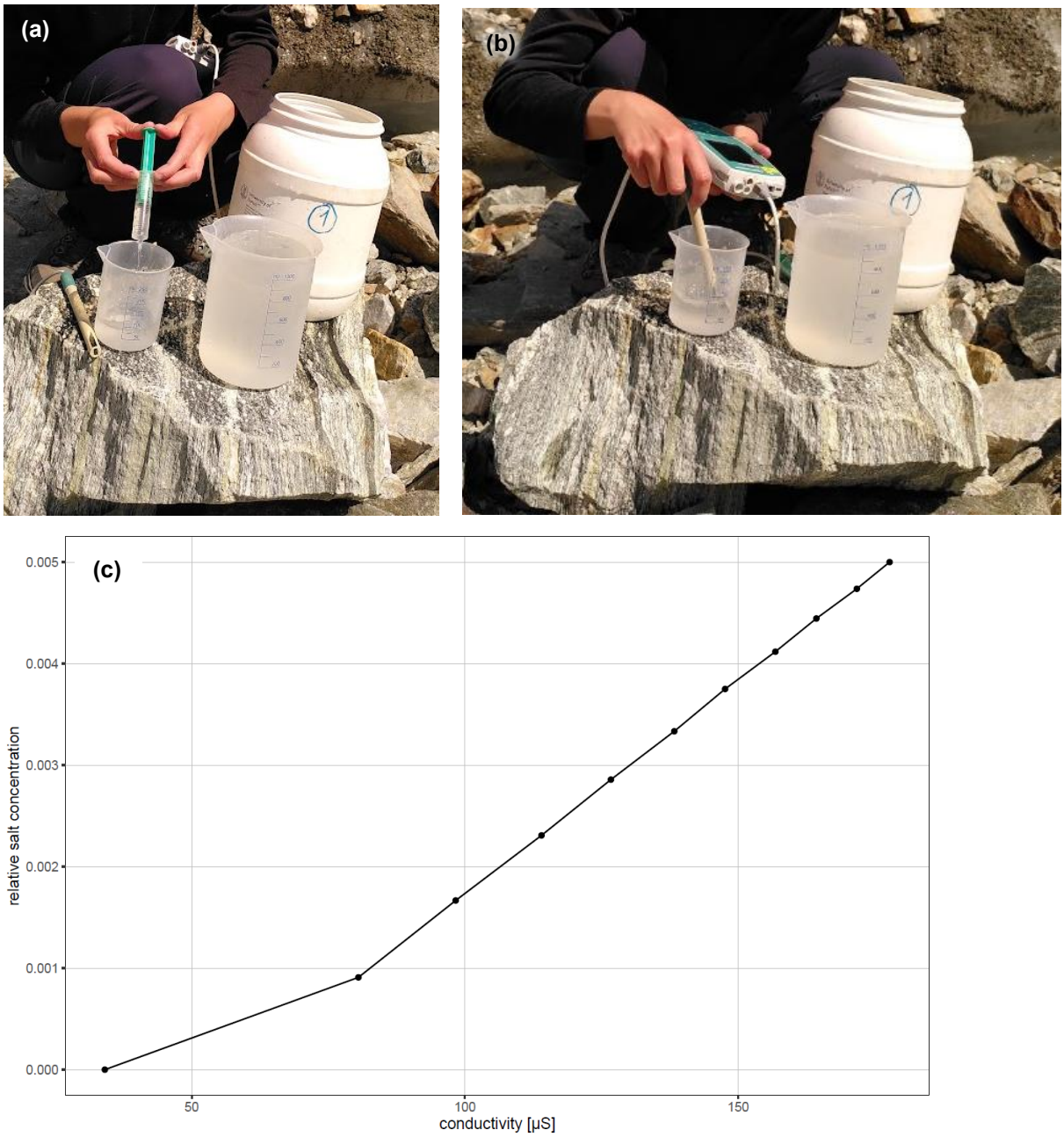

Figure 8: Calibrating the concentration of the salt dilution (in vessel no. 1). (a) 1 by 1 ml is added to 100ml of stream water (small beaker). In the larger beaker, 1l of stream water mixed with 1 ml of the salt dilution. (b) The concentration is measured with the conductometer with every ml added. (c) The conductivity-salt concentration (from the July 12 14:00 UTC measurement) calibration for the 10 ml salt dilution added in 1 ml steps to the 100ml of stream water.

Downstream of the injection, the electrical conductivity (EC) was measured with a *Metrohm* conductometer. The measurement is recorded from the moment of the injection until the EC was back to the background concentration of the channel. As a rule of thumb, the distance between EC measurement and injection of the dilution should be 10-20 times the width of the stream. For the data presented here, the distance between injection and EC measurement was roughly 10m, whereas the width of the channel was approximately 0.5m. The conductometer measured at an interval of one second (Figure 9).

The discharge was calculated with the following formula where V is the volume of the injected dilution and C_c the salt concentration:

$$Q = \frac{V}{\int C_c} \tag{5}$$

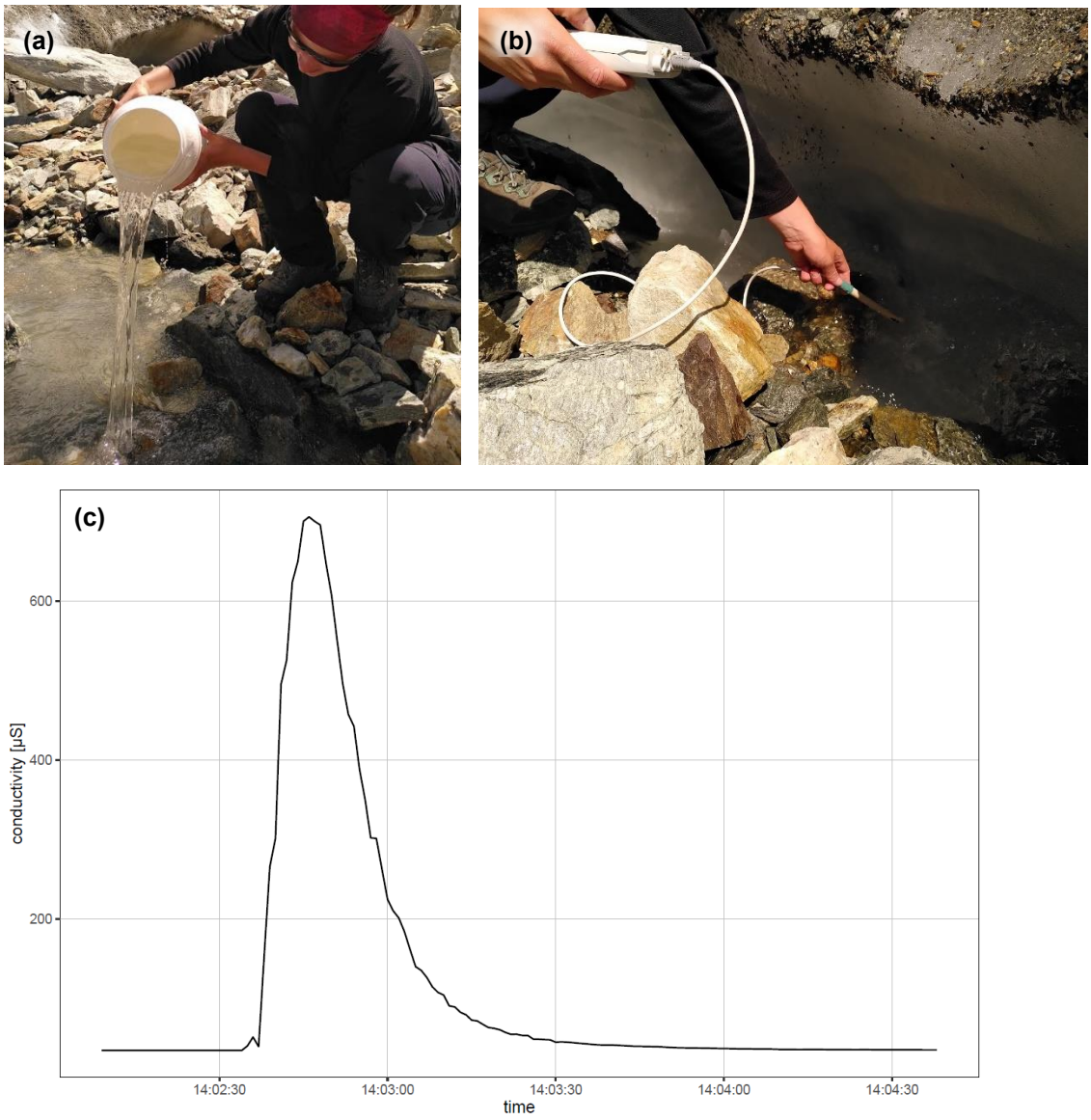

Figure 9: (a) The salt dilution is injected in the stream. (b) The conductivity of the stream is measured while the salt dilution is passing by. (c) Example of the measured conductivity on July 12 14:00 UTC forming the typical shape of a fast ascend in conductivity and a smoother decrease until the background conductivity is reached again.

In each subperiod, the aim was to have one day of intense measurements, meaning one measurement every two hours. In addition, few measurements should be conducted on the other days. Due to malfunctioning of the *Metrohm* conductometer, fewer measurements were made. As a replacement, 4 measurements on July 26 were taken with a conductivity temperature and depth (*Decagon CTD*). This did not record automatically in one-second intervals. As a quick solution,

every 5 seconds, the conductivity was measured and noted manually. However, as the devices were differently calibrated, the measurements of the CTD were eventually excluded from the discharge calculations. Overall, 14 discharge measurements were made that were further used in combination with the water level monitoring for a continuous discharge within the subperiods.

3.3.2 Water Level Monitoring

In addition to the salt dilution gauging, water pressure was measured continuously over periods of one to two days in each subperiod in July and August with a 10-minute measurement interval. To determine a continuous (10 *min* temporal resolution) discharge value, the relationship between the salt dilution gauging and the water pressure measurements needed to be established.

In a first step, the water pressure was corrected by the measured air pressure at the meteorological station. Because there is an elevation difference between the meteorological station and the site where the water pressure was measured. Thus, the measured air pressure was corrected by the elevation difference. Then from the corrected water pressure, the water level h_w (m) was calculated with the density and the gravitational acceleration:

$$h_w = \frac{p_w}{\rho_w \, g} \tag{6}$$

1.25 cm were added to the calculated h_w as the pressure sensor was in the middle of a 2.5 cm thick pipe and the lowest 1.25 cm of water are below the sensor and therefore not included in the measured overburden pressure.

Once the h_w was calculated, it could be combined with the discharge point measurements. The rating curve describes the relation between h_w and the measured Q (l s^{-1}) with the salt dilution gauging as

$$Q = c \, {h_w}^n, \tag{7}$$

where n corresponds to $\frac{3}{2}$ for a rectangular shaped channel (Manning, 1891) and c as a fitting constant determined with the NLS index (formula (3) for all measurements and for each sub-period. The c values for the best fits are summarised in Table 4. With the rating curves, a continuous discharge estimate for each subperiod could be determined.

-

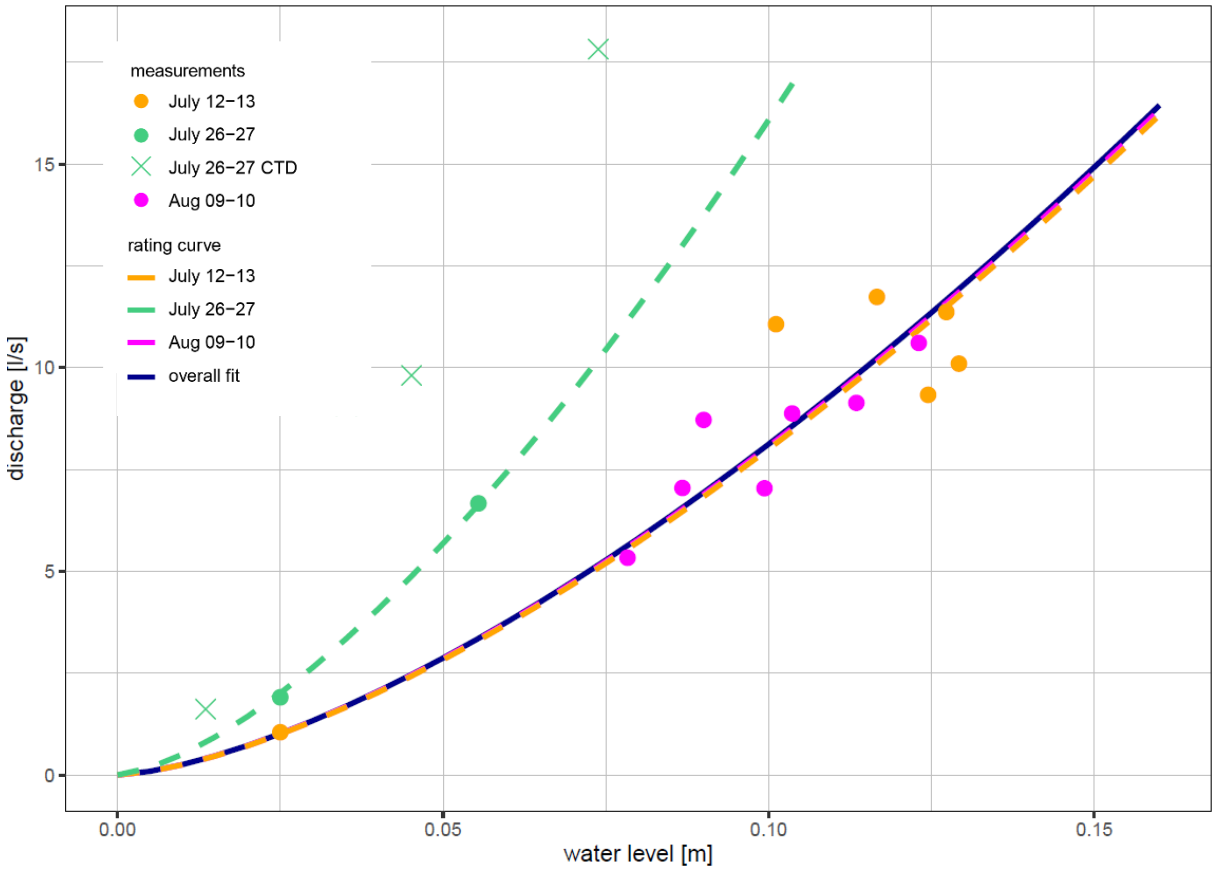

Figure 10: Discharge and water level measurements and rating curve of the different subperiods (dashed lines) and of the overall period (solid). For the three measurements that were read out by extrapolation of the water level curve, an error of +-0.005m is indicated.

Table 4: c values resulting in the RSS for the optimal parameter c for the different periods with measured h_w and the overall fit.

Time span	c	# considered discharge measurements	RSS
June 29-30	-	-	-
July 12-13	0.2532	5	17.27
July 26-27	0.5088	2	0.01159
09-10 August	0.2551	7	5.274
Overall	0.2569	14	36.83

3.3.3 Catchment-Wide Meltwater Modelling

To model the discharge from the ETIM at the spot, where the discharge measurements were made, the model results from the ETIM were cumulated over the entire catchment. The hourly ablation rate, which resulted from the ETIM, was converted to an amount of melt rate in water equivalents per second. Assuming this melt rate for the entire catchment area *A*, the total melt rate of the entire

catchment per second could be calculated. Precipitation was rare during the measurement period. Nevertheless, to model a potential discharge Q_{pot} (m^3 s^{-1}) the total melt rate per second was combined with precipitation rate per second $\dot{p}$ was considered. Precipitation was measured at the meteorological station and calculated per second. Q_{pot} was compared to the estimated discharge based on the salt dilution gauging and water-level monitoring of the subperiods.

$$Q_{pot} = \dot{a}_d \frac{\rho_i}{\rho_w} A + \dot{p} \tag{8}$$

The catchment area A was determined in *ArcGIS*. The initial DEMs were resampled to a 1m resolution. Sinks shallower than 0.5 m were filled. From the pre-processed DEM, a D8 Flow Direction raster file was calculated. This again was the base of determining drainage basins. With the Flow Accumulation tool, the flow paths of the meltwater were detected. The resulting watersheds touching the mapped channel and the basins that were surrounded by watersheds touching the mapped channel were combined to the total contributing catchment. The top of the catchment was restricted by a moulin and both assumption and computation showed that the areas above the Moulin do not contribute to the discharge at the measured spot. The catchment is confined on both sides by the medial moraines on the glacier.

This catchment determination was done for all DEMs. However, as the two DEMs from June 29 and July 12 had rather small extends, they were not used for the total contributing area A. The extents of the July 26 and August 09 were quite similar. In both cases, the catchment seemed to continue further back on the right orographic side, however, the DEMs end was reached. Based on the comparison of the catchment outlines of July 26 and August 09, the assumption was made that the catchment does not change significantly within the timescale of investigation. For this reason, the contributing area from the DEM of July 26 (Figure 11) was used for the entire modelling. The catchment from the DEM of August 09 is in Appendix V.

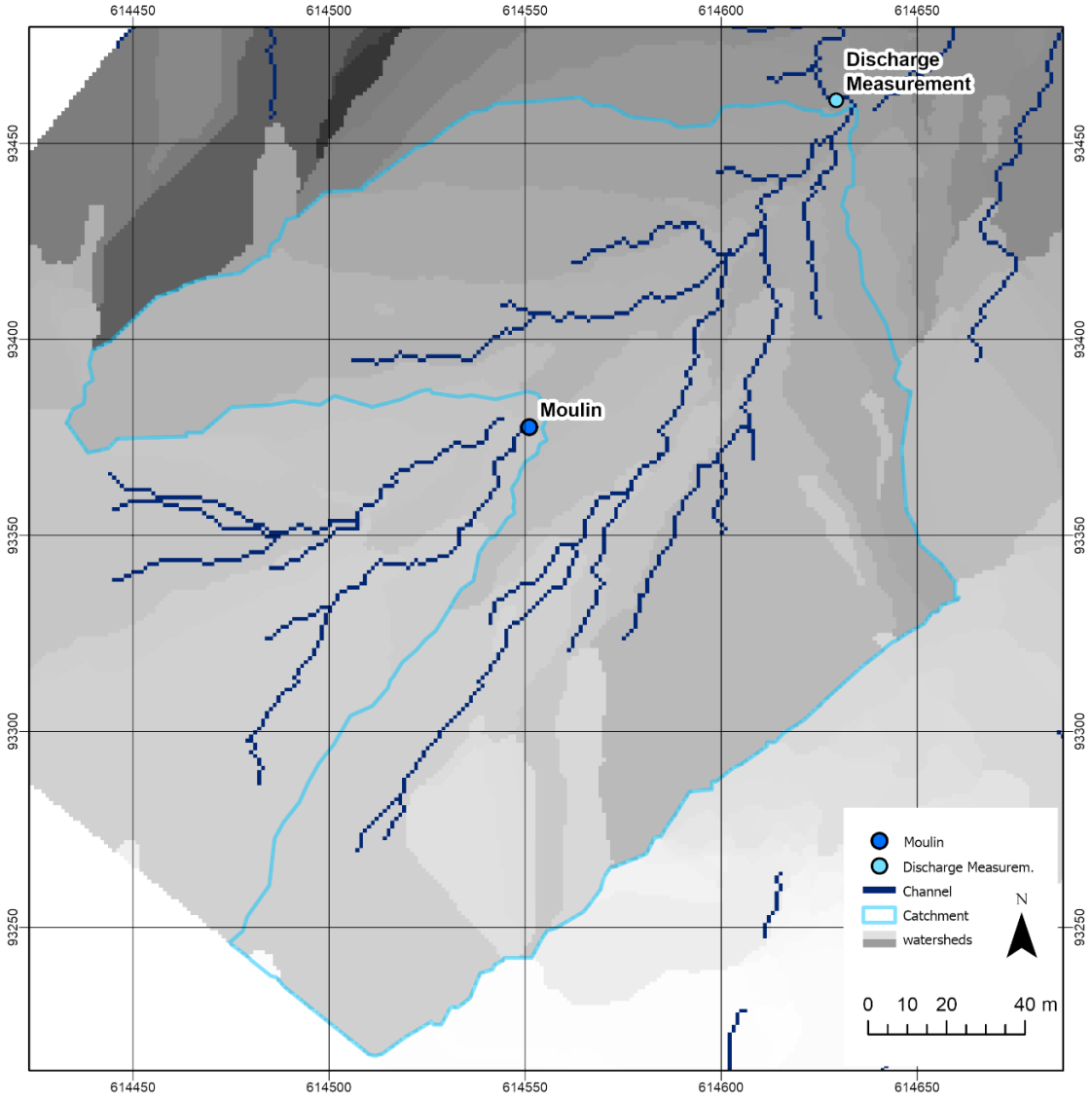

Figure 11: Catchment determination from the DEM of July 26, 2022, with the single drainage basins (watersheds) and the automatically mapped channel.

3.4 Supraglacial Channel Incision and Ice Cliff Backwasting

The modelled discharge was in a final step used to model the supraglacial channel incision and to compare it to the measured incision and ice cliff backwasting rates. The channel incision and ice cliff backwasting were measured at two cross-sections with different orientations. Channel incision and ice cliff backwasting was measured by hand and by remote sensing with a laser scanner.

3.4.1 Channel Incision and Ice Cliff Backwasting Measurements

At two locations along the channel, the change of a channel cross-section was repeatedly measured. The two locations had different aspects, one cross-section was north-west-oriented (cross-section 1) and the other north-east (cross-section 2) (Figure 12).

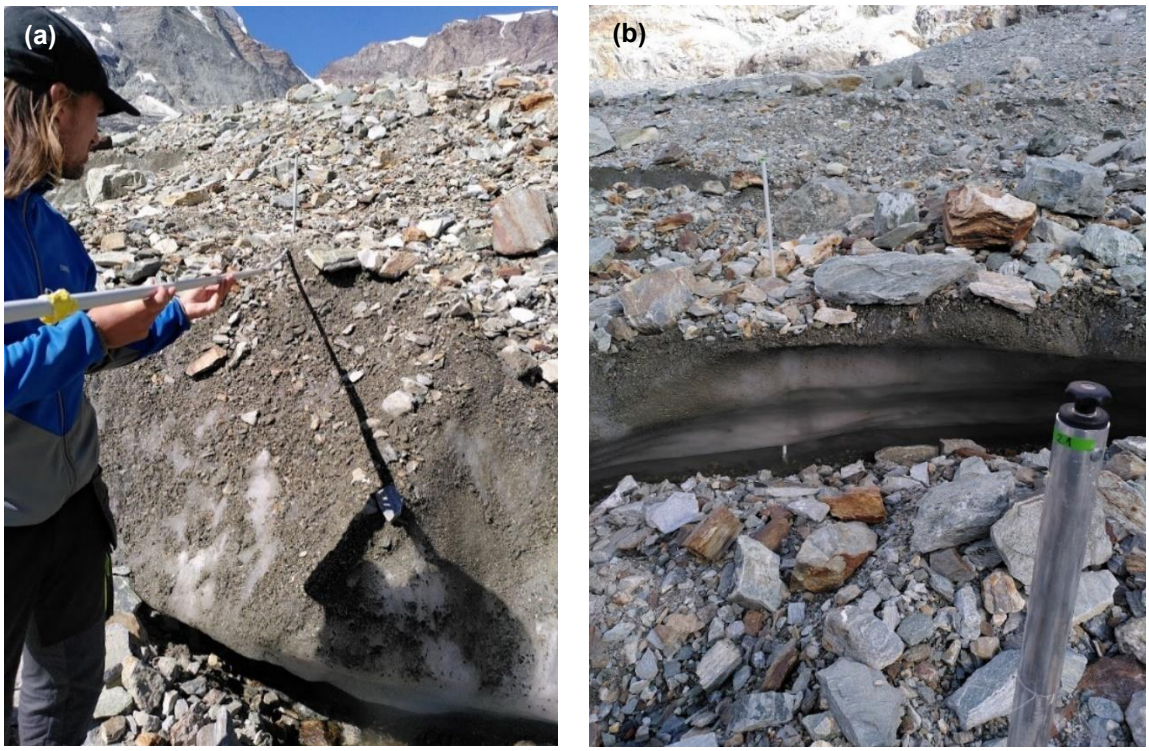

Figure 12: The two monitored cross-sections. (a) cross-section 1 with NE-facing ice cliff and (b) cross-section 2 with NW-facing ice cliff.

From a reference stake on low side of the channel, the distances and angles to the furthest point within the channel, as well as to the lower and upper edges of the ice cliff on the opposing side of the channel, were measured (Figure 13). The distance was measured with a meter stick reinforced with a PVC or aluminium stake and the angle was measured with a compass clinometer held along the stake. Several measurements in the same cross-sections were taken in each subperiod. To stay in the same profile in the channel, another reference stake at the other side of the channel was used.

The method is simple but brings uncertainties. Measuring in a slightly different spot can quickly lead to great variances, especially in the angle measurements. To reduce unwanted short-term variance, one average erosion rate per field trip were taken.

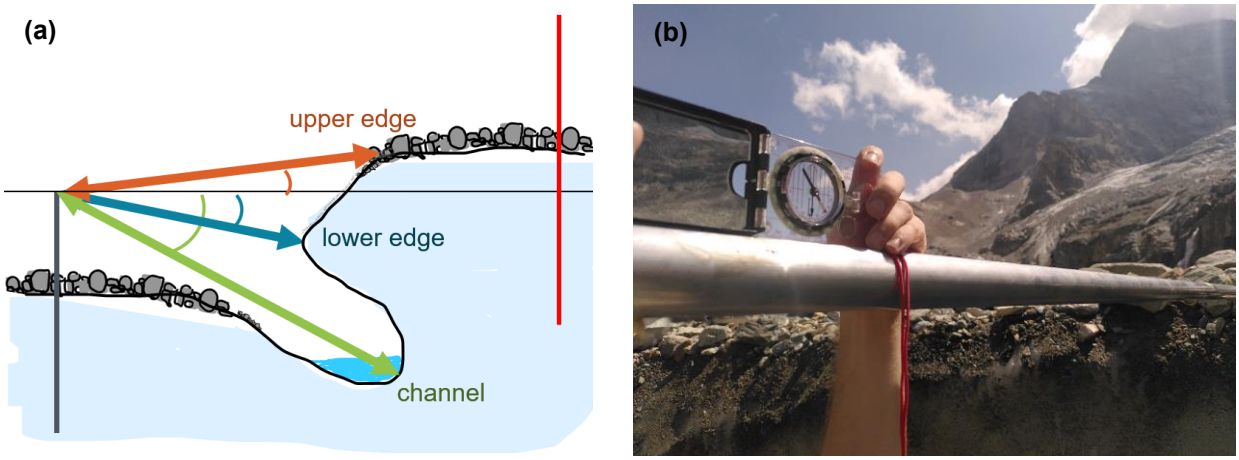

Figure 13: (a) Schematic sketch of the distances and angles measured in the channel cross section from a reference stake (grey). The red stake is the reference stake that was taken for orientation to stay in the same profile over time. (b) Measuring the angle to an upper cliff edge with a compass clinometer along the reinforced measuring stake.

3.4.2 Laser Scans of Channel Cross-sections

With a *Leica BLK 360* laser scan, overlapping scans were made in the area around the monitored cross-sections. The scans were made on one day in each of the 4 subperiods. The resulting point clouds were aligned for a continuous picture with the reference stakes in the Leica *Cyclone Register 360 2022* software. The 4 point-clouds were horizontally aligned and the same cross-sections as those that were hand-measured were extracted in the *Cyclone 3DR software* for the 4 different dates. The surface elevations were then corrected for the ablation.

The point cloud cross-sections were compared to the hand measured cross-sections. From the scanned cross-sections, the different compounds of the erosion along the supraglacial channel were determined. These were the vertical incision in the stream, the horizontal incision of the stream under the ice cliff and the backwasting of the ice cliff.

3.4.3 Supraglacial Channel Incision: Theoretical Model A

The aim of the thesis is interlinking meteorological data, ablation, discharge and incision in the supraglacial channel. From the modelled ablation and discharge in the previous steps, channel incision was modelled with two different formulae.

Fountain and Walder (1998) base the incision on a supraglacial channel on heat dissipation. All energy produced in the water and at the ice-water-interface is used for melting. Incorporating gravity, they describe the downcutting rate, i.e. vertical incision, as

$$\dot{d} = \frac{1}{2}\left(\frac{\pi}{2\tilde{n}}\right)^{\frac{3}{8}} \frac{\rho_i}{\rho_w} \frac{g}{L_f} S^{\frac{19}{16}} Q^{\frac{5}{8}}, \quad (9)$$

where ñ $= 0.01$ s m$^{-1/3}$ is the Manning's roughness coefficient for a clean-ice channel, S is the slope along the channel and Lf the latent heat of ice melting. It is plausible that even though the channels on the debris-covered glacier are relatively clean, the roughness is higher than on a clean-ice glacier. The sensitivity of the roughness was analysed.

3.4.4 Supraglacial Channel incision: theoretical Model B

Another approach to model supraglacial channel incision is suggested by Ogier *et al.* (2021), relating the incision rate $\dot{m}$ (m m^{-1} hour^{-1}) to the heatflux q, which is defined as the thermal conductivity of water k_w, the Nusselt number Nu and the temperature difference between the stream water and ice ΔT divided by the length scale over which the heat flux occurs λ:

$$\dot{m} = \frac{q}{\rho_i L_f} = \frac{1}{\rho_i L_f} \frac{k_w \, Nu \, \Delta T}{\lambda} \tag{10}$$

L_f is the latent heat of fusion. The temperature difference between the water and ice with time, was measured with the *RBR duett* sensor, which was also used to measure the water pressure. As the water temperature correlates with the water level and therefore with the discharge, ΔT was thus extrapolated over the entire timespan as

$$\Delta T = 0.0128 \times Q - T_0. \tag{11}$$

The Nusselt number Nu indicating the heat transfer coefficient is defined by the Dittus–Boelter equation:

$$Nu = A \, Pr^{\alpha} \, Re^{\beta}, \tag{12}$$

where $A = 1.78$, $\alpha = 0.333$ and $\beta = 0.58$ as empirical parameters used by Ogier *et al.* (2021) and the Prandtl number $Pr = 13.5$ (at 0°C) (Clarke, 2003; Ogier *et al.*, 2021) and the Reynolds number, which quantifies turbulent flow:

$$Re = \frac{\upsilon D_H}{\nu}, \tag{13}$$

where $\upsilon = \frac{Q}{cs}$ with cs is the wetted cross-sectional area, ν the kinematic viscosity, and $D_H = \frac{4\,cs}{\lambda}$ is the hydraulic diameter.

The length scale over which the turbulent heat flux occurs λ is assumed to correspond to the wetted perimeter in the case of the supraglacial channel on Zmuttgletscher. The wetted perimeter was not measured in the field. Therefore, it had to be estimated from the average water level and the channel width detectable on photographs taken. The estimated wetted perimeter lies between 0.5 and 0.1 m. The sensitivity of $\dot{m}$ with different λ was tested. The cross-sectional area *cs* is derived from λ, approximated by the assumption that *cs* is a semicircle. As the channel is on the surface of the ice, the wetted perimeter as well as the wetted cross-sectional area are not expected to change with a constant discharge.

The modelled incision rates were compared to the cumulative channel incision measured in two cross-sections of the supraglacial channel. In a further step, the modelled incision was compared with the horizontal incision and the ice cliff backwasting.

4 Results

4.1 Meteorological Data

Air temperature, shortwave incoming radiation and precipitation were measured at the meteorological station (Figure 14). Shortwave incoming radiation (SW_{in}) and temperature (T) were needed as input data for the ETIM, precipitation as input or the discharge modelling. It is visible that both T and SW_{in} show a diurnal variation with peaks in the afternoon. SW_{in} decrease to 0 during the night. Lower temperatures in the beginning and end of July correlate with precipitation events.

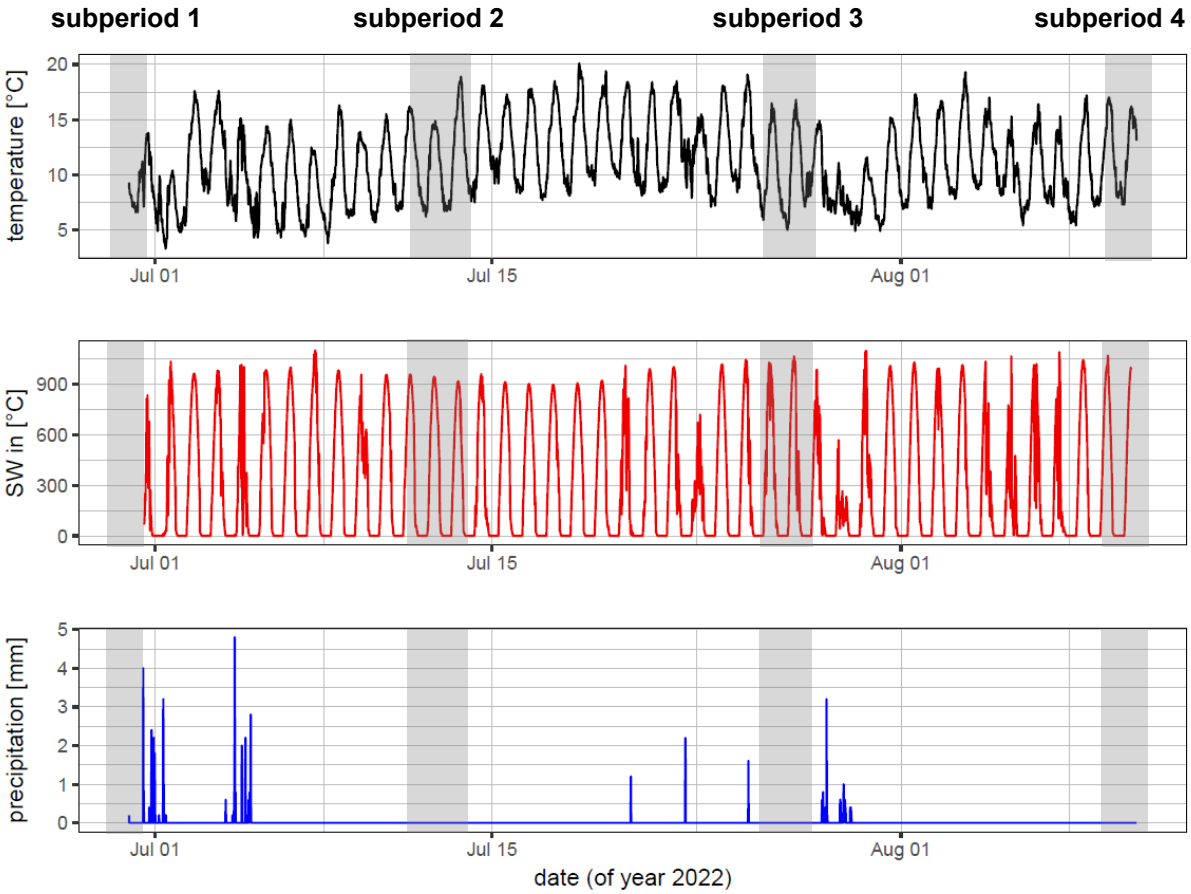

Figure 14: Temperature, shortwave incoming radiation, wind speed and precipitation measured at the meteorological station on Zmuttgletscher. These input data are also used for the ETIM and discharge modelling.

4.2 Ablation

4.2.1 Sub-Debris-Ablation Measurements

Ablation Stake Measurements

Ablation was measured for the total period of 41 days (Figure 15). 9 ablation stakes were used for the calibration of the ETIM (A1-A9). The total cumulative ablation ranged between 143 cm for stake A3 and 205.5 cm for stake A9. The average melt rate is 4.86 cm day^{-1} with a standard deviation of 3.75 cm day^{-1}. During the subperiods, ablation was measured twice a day at all stakes (morning and evening) and diurnal fluctuations in the melt rate are visible. Between the 2nd and 4th subperiod, melt rates are higher than between the 1st and the 2nd. The melt rates are summarised in

Table 5.

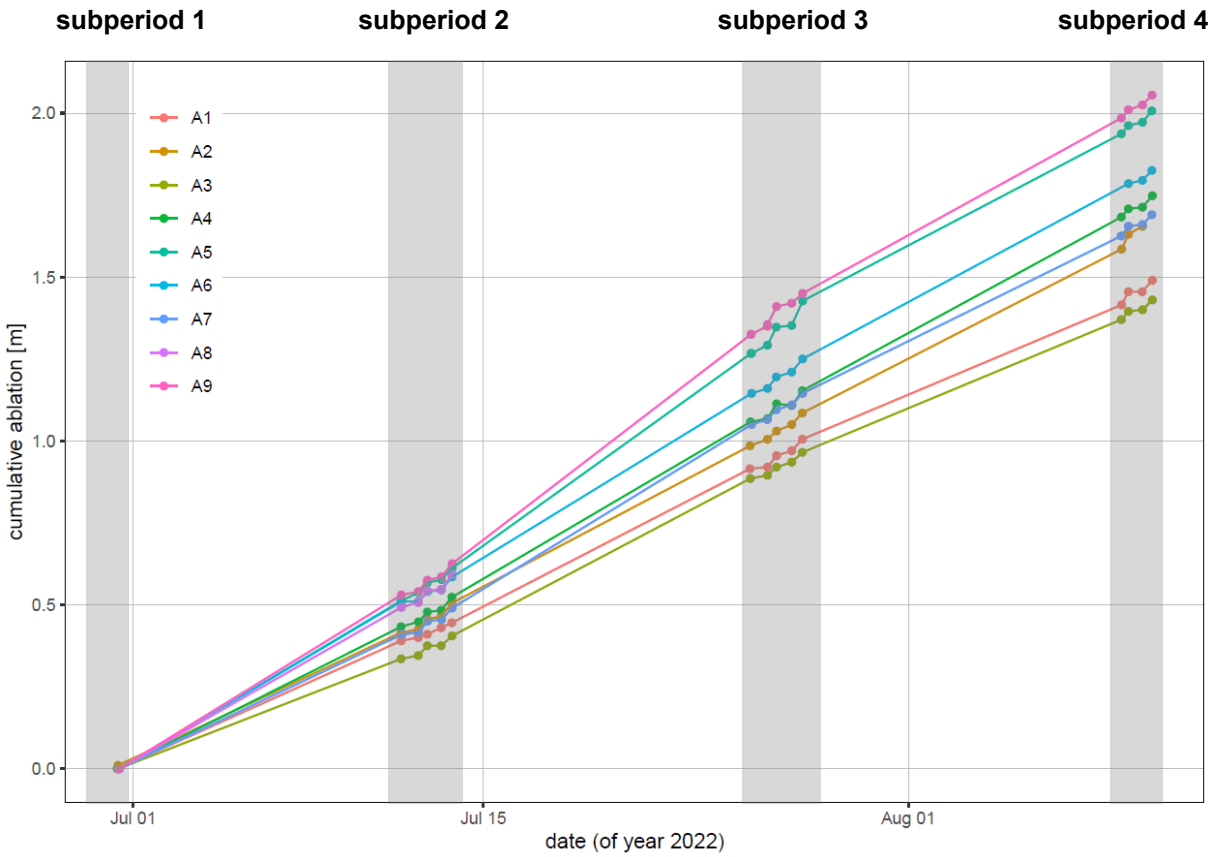

Figure 15: Cumulative ablation of the stakes considered for the ETIM. The total period is 41 days.

Ablation rate during the night was significantly smaller than during the day. Therefore, a typical step-like diurnal pattern is visible between the morning and evening measurements within the subperiods, for instance between July 11 and 13 (Figure 16). However, the diurnal variations are not equally pronounced for every ablation stake.

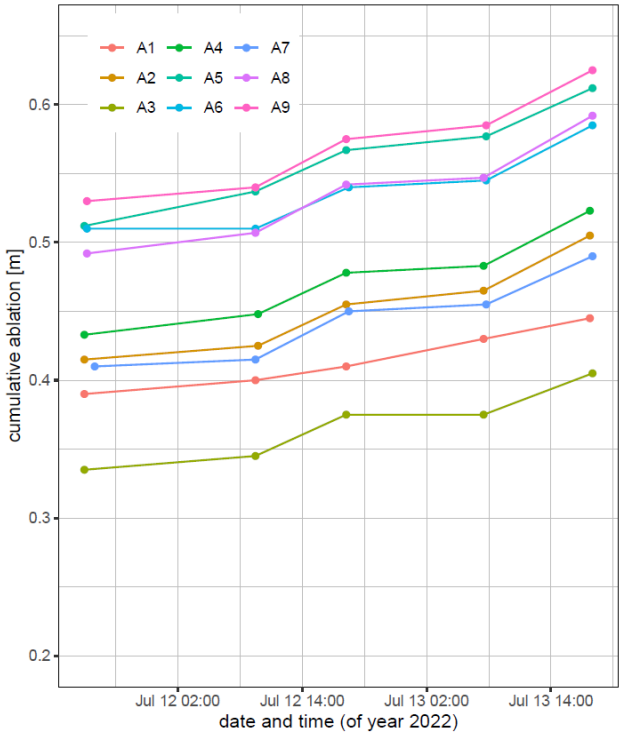

Figure 16: Zoom into subperiod 2, the melt rate variation between day and night is visible.

Ablation and Debris Cover Thickness

The measured ablation is expected to be influenced by the local debris cover thickness. Cumulative ablation is therefore coloured by the respective debris cover thickness at the ablation stake (Figure 17). The average debris cover thickness from all stakes measured is 7.88 ± 2.3 cm with a range from 5 to 13 cm. At stakes where a higher debris cover thickness was measured, ablation tends to be lower. However, there are some stakes that show an anomalous melt behaviour. This indicates that debris cover thickness is not the only factor influencing local ablation differences. The boxplot in Figure 17, where ablation stakes are grouped into 3 debris cover thickness classes, confirms the correlation between melt rate and debris cover thickness. There are still melt rate differences within the classes. The largest variance in melt rates shows the class of debris cover thicknesses between 5 and 7 cm.

To model the discharge at the location where discharge measurements were made on the glacier, the ablation rate average of the catchment was of greater interest than ablation rates at single stakes. Furthermore, the variation in debris cover thickness between the stakes relatively small. Therefore, the average debris cover thickness was used for the entire catchment. Accordingly, an average insulating factor F_{ins} of 0.567 was assumed.

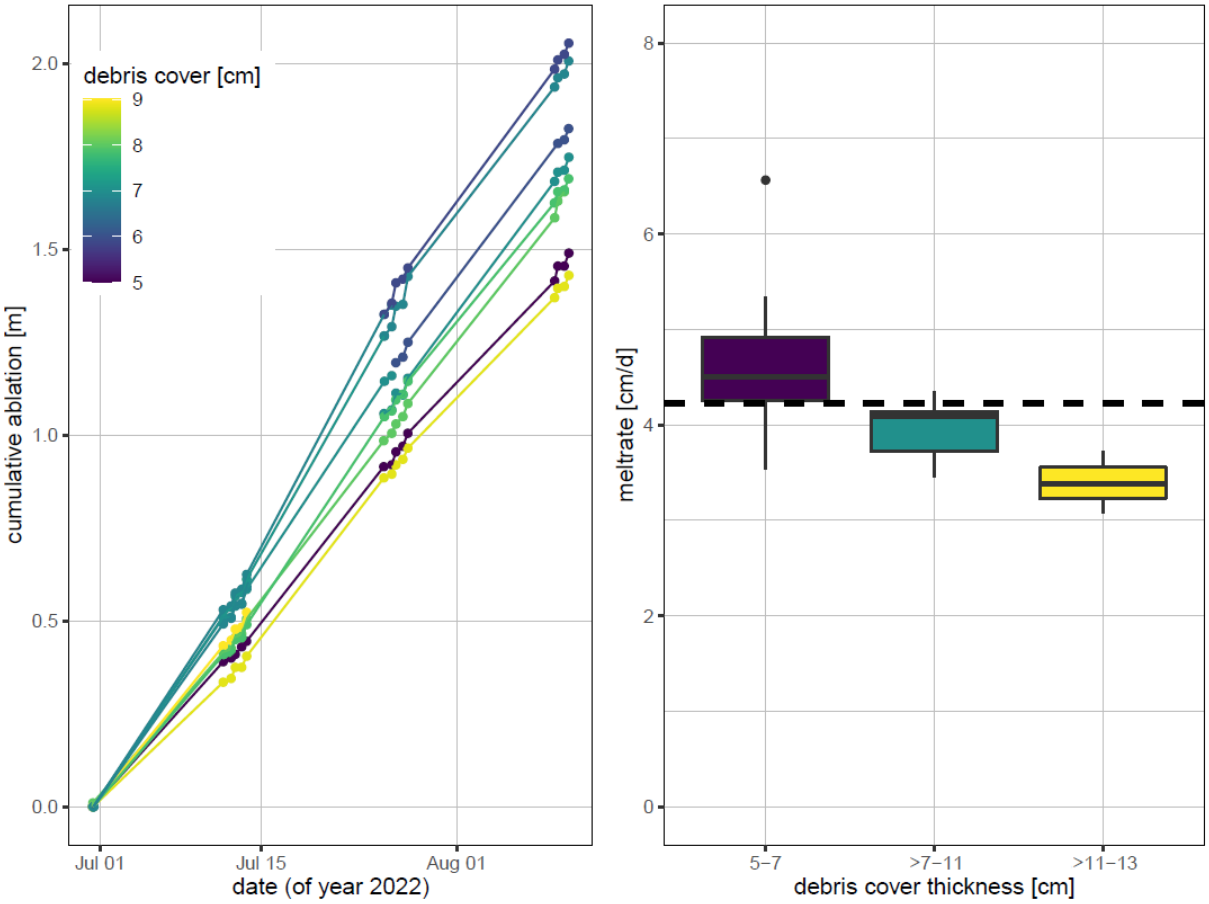

Figure 17: (a) Cumulative ablation measurements of the stakes considered for the ETIM with time, coloured by the supraglacial debris cover thickness measured at the site of each stake. (b) Boxplot of melt rates and different debris cover thicknesses, divided into 3 thickness classes of 5-7, >7-11 and >11-13 cm. The average melt rate (4.2 cm day^{-1}) of the average debris cover thickness (7.8 cm) is indicated as the dotted line.

The correlation between melt rate and debris cover thickness is shown in Figure 18. The measurements of the field campaign of this thesis on Zmuttgletscher in 2022 are depicted in green and compared to the melt rate of Zmuttgletscher in 2021 (blue, Farsky unpublished, 2021) and the melt rates measured in literature (compiled by Hardmeier, unpublished, 2021). In 2022, no clean ice ablation measurements were taken. Therefore, no clean ice reference was available for normalisation and in equation (2, the D_0 of 2021 was used. For this reason, the data could not be normalised and the effectively measured melt rates are shown in Figure 18. This makes comparison of the insulating effect between different glaciers and different years more difficult. Nevertheless, on Zmuttgletscher in 2022 the same trend is visible in the other datasets. The Østrem curve, which describes this relation of the decrease in ablation rate with increasing debris cover thickness, is visualised for Zmuttgletscher data of 2021, however, without the increased melt rate with a thin debris cover. In 2022, melt rates on Zmuttgletscher were significantly higher than in 2021. This can be explained by the high temperatures of the summer 2022, which increased melt rates in general (Hardmeier unpublished, 2021).

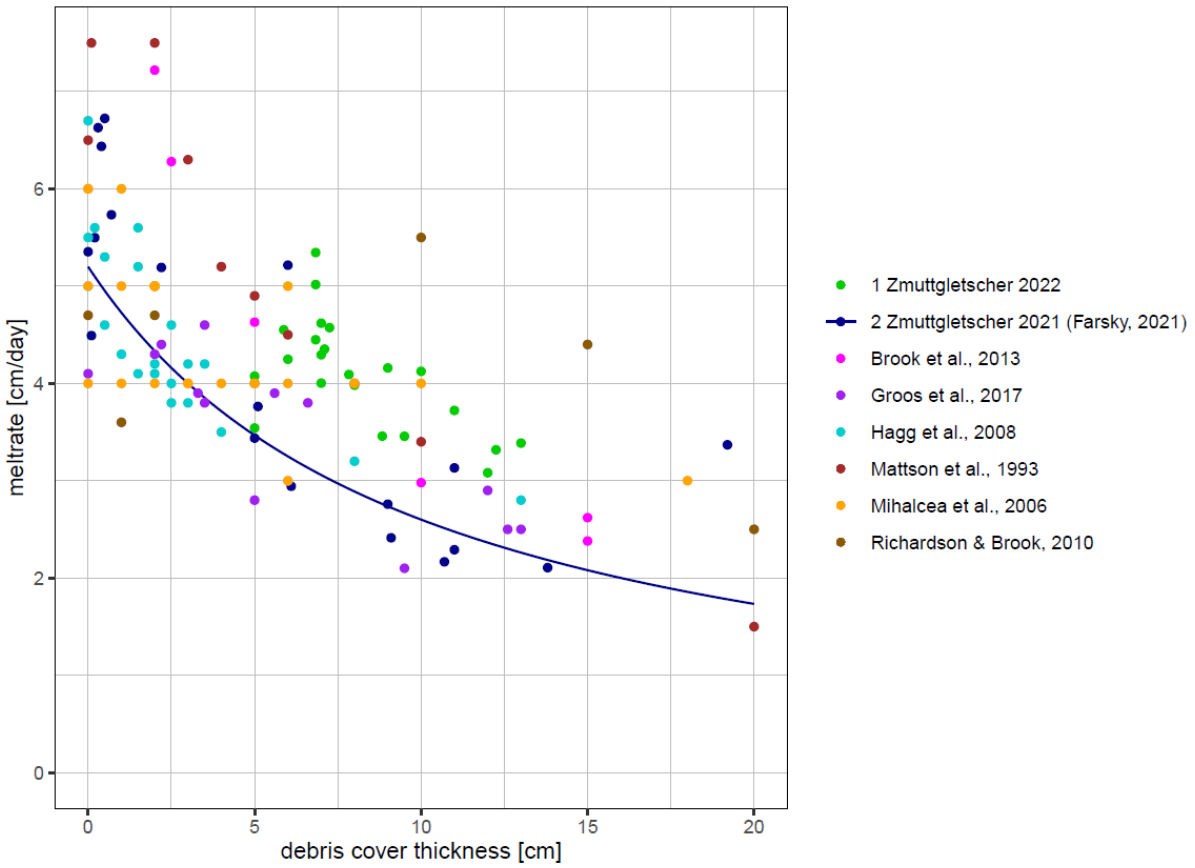

Figure 18: Melt rates with increasing debris cover thickness on Zmuttgletscher in 2022 and 2021 as well as values from literature (Mattson et al., 1993; Hagg et al., 2008; Richardson and Brook, 2010; Brook, Hagg and Winkler, 2013; Groos et al., 2017). The line for the 2021 data shows the Østrem curve (1959) with a D_0 of 0.1 (Farsky unpublished, 2021), omitting the increase in melt rate for a thin debris cover.

4.2.2 DEM Differencing

To compare the measurements of the ablation stakes with independent measurements, in each subperiod, a UAV image acquisition was conducted, from which an orthophoto and a DEM was produced. The different DEMs were corrected and differentiated to determine surface elevation loss rates within the 2-week intervals (Appendix I, Appendix II, Appendix III) and of the total period (June 29 to August 09, 2022) (Figure 19).

Surface elevation lowering is visible everywhere in the catchment. It is assumed to mostly correspond to ice loss. The area along the channel system shows a stronger melt rate than the areas further away from the channel. However, other areas with high melt rates are visible. The orographic left side of the channel shows a relatively uniform melt rate, whereas a higher variance and local higher ablation rates are visible on the right side of the channel. There are some artefacts, for instance some rocks which are identifiable as the DEMs do not match perfectly despite co-registration of the pre-processing.

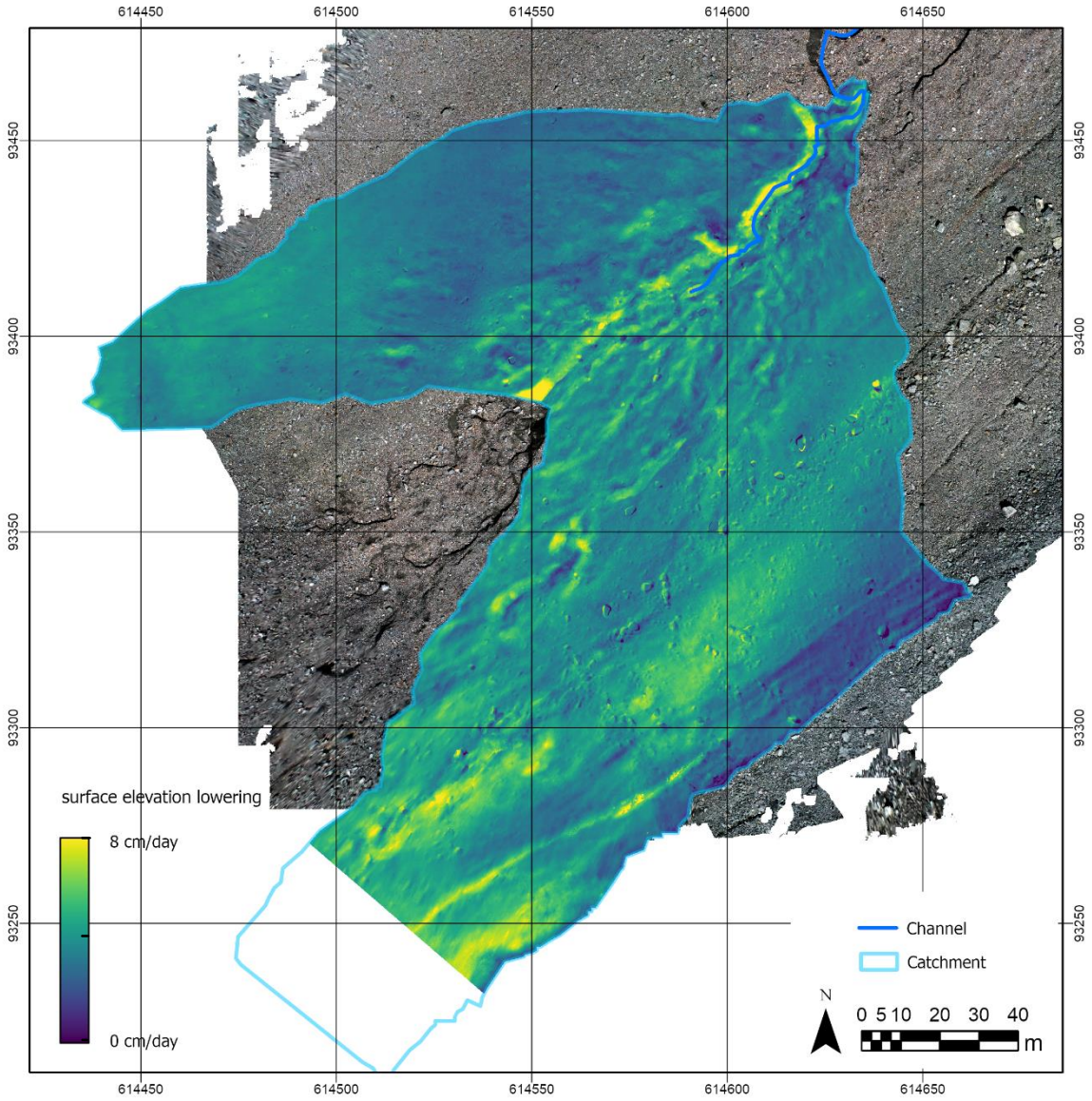

Figure 19: Melt rate determined from the surface elevation difference of the DEMs of June 29 and August 09. The time difference is 41 days.

Surface ablation in areas where there are no channels are split into orographic left and right side. Moreover, the surface ablation in ice cliff areas is extracted from the DEM and summarised in Table 5. Melt rates as well as cumulative ablation are 1.5-2 times higher in ice cliff areas than sub-debris meltrates. Furthermore, a difference in melt rates can be seen between the two sides of the catchment. The ablation determined from the DEM difference are compared to the average ablation measurements at the stakes.

Table 5: The ice elevation change rate is set equal to the ablation rate. The different ablation rates of the orographic left and right sides of the channel as well as in mapped ice cliff areas and the average ablation are extracted from the corrected DEM surface elevation differencing. Furthermore, the ablation stake measurements are complemented. The cumulative ablation is the surface elevation between the respective date to the DEM acquisition and June 29, whereas the melt rate is respective for the period of the prior 2-weeks to the indicated date.

	cumulative ablation DEM [m]	standard deviation DEM ablation [m]	melt rate DEM [m day^{-1}]	average cumulative ablation from stakes [m]	average melt rate from ablation stakes [m day^{-1}]
22-07-12					
left	0.453	0.112	0.0348		
right	0.436	0.134	0.0335		
ice cliff	1.337	0.306	0.1028		
average	0.452	0.151	0.0348	0.47	0.036
22-07-26					
left	1.111	0.159	0.0411		
right	1.024	0.257	0.0487		
ice cliff	2.116	0.259	0.0784		
average	1.137	0.246	0.0421	1.11	0.046
22-08-09					
left	1.596	0.205	0.0389		
right	1.799	0.362	0.0439		
ice cliff	2.998	0.210	0.0731		
average	1.746	0.348	0.0426	1.75	0.046

4.2.3 Enhanced Temperature Index Model (ETIM)

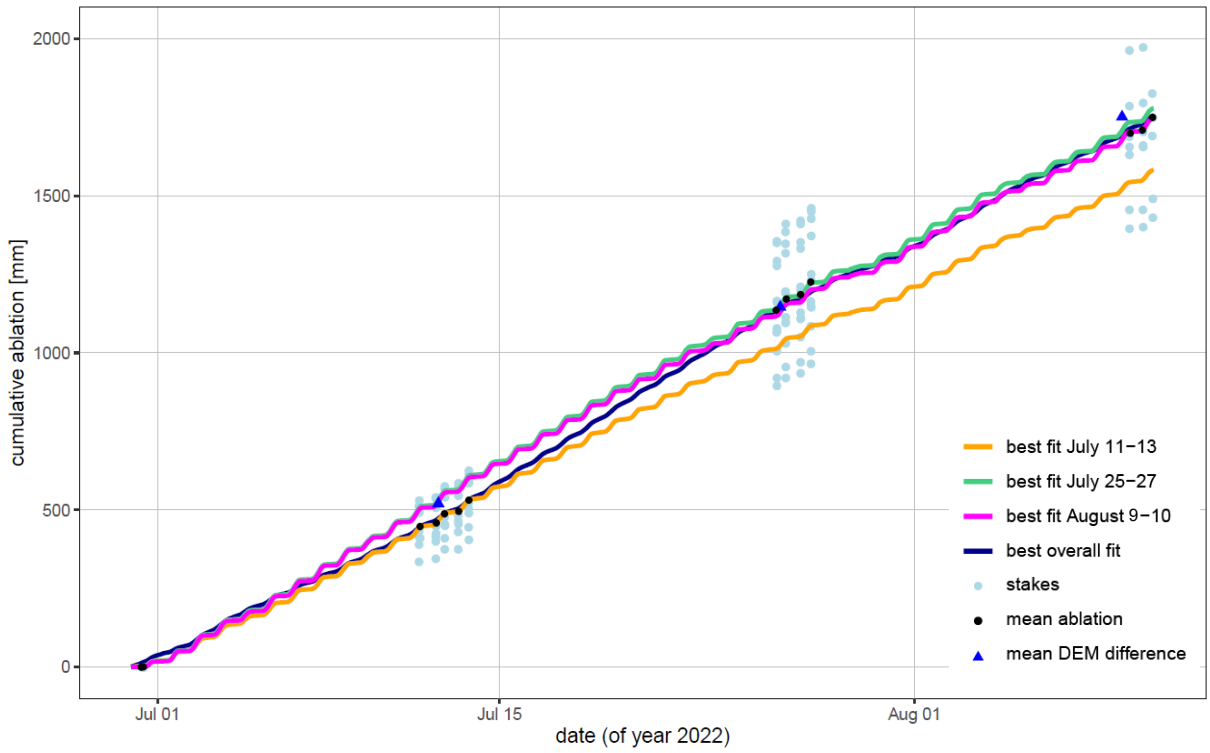

Figure 20: The individual cumulative ablation measurements of the stakes considered for the ETIM, the mean cumulative ablation from the measurement cycles and the mean height difference of the corrected DEM are plotted with time. With the ETIM, the mean ablation was approximated.

ETIM Fitted Against Overall Trend

The ablation rate was modelled with the ETIM and cumulated with time (Figure 20). The meteorological data were fitted against the measured ablation. In a first step, an overall ablation trend was modelled with the ETIM (dark blue line). From each measurement cycle, the average cumulative ablation from all stakes was calculated (black dots). The mean cumulative ablation is relatively close to the catchment average ice losses determined from the slope corrected DEM (summarised in

Table 5). The model was calibrated to the mean ablation measurement in each measurement cycle (black). The best resulting parameter combination (Table 6) used a small shortwave factor F_{SW} and temperature is the main forcing of the ETIM equation (2). However, short term large diurnal fluctuations are not well represented in this overall best fit.

ETIM Fitted Against the Subperiods

To better represent the diurnal variations, the ETIM was fitted against the individual subperiods 2, 3 and 4 (detailed in Figure 21). The fits of the ETIM against the subperiods show the diurnal ablation variation more accentuated.

The fit for subperiod 2 (orange line) represents the respective period well, however, the model underestimates later ablation measurements and results in a significant underestimation (158.2 cm) of the average total cumulative melt (174.9 cm). Hence, this fit could not be used to describe the measured ablation. The ablation modelled from the ETIM fits to subperiod 3 (green line) and 4 (magenta line) are very similar to each other. In the first two weeks of the measurement period, they behave almost identically and overestimate the measured cumulative ablation from subperiod 2. However, the ablation measurements of subperiods 3 and 4 are well represented by both fits. They give a good representation of the total cumulative ablation (177.8 cm and 174.7 cm, respectively), with the calibration to subperiod 4 representing the total cumulative ablation slightly better. Simultaneously, they show the desired variation in the ablation rate between day and night.

From the calibrations to the subperiods, the model fitted to the measurements from subperiod 4 showed the least RRS for the overall mean cumulative ablation rates and was used for the further calculations (Table 6).

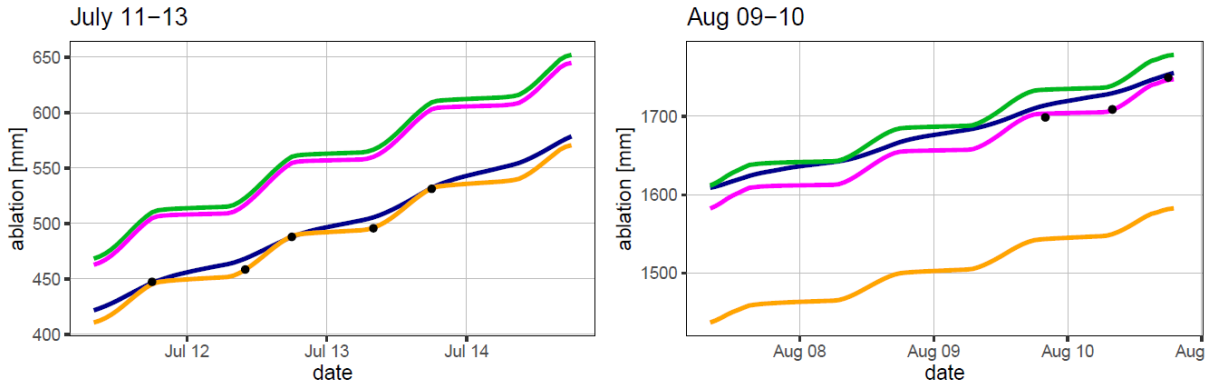

Figure 21: Zoom into the diurnal variations of the modelled ablation at the example of subperiods 2 and 4. The same colour code is used as in Figure 20.

Table 6: F_T and F_{SW} best fits for the different periods of frequent measurements as well as for the overall period with their residual sum of squares for the respective period as well as for the overall period.

	F_{ins}	F_T	F_{SW}	*RSS* for respective subperiod	*RSS* total period

Fit for subperiod 1 Jun 29-30 2022	0.568	-	-	-	-
Fit for subperiod 2 Jul 11-13 2022	0.568	0.073053	0.008038	5.412	145746.1
Fit for subperiod 3 Jul 25-27 2022	0.568	0.04666	0.01063	58.2	27459.63
Fit for subperiod 4 Aug 09-10 2022	**0.568**	**0.03218**	**0.01106**	**30.88**	**22329.31**
Overall fit general trend	0.568	0.2574931	0.0009591	-	2751.15

4.3 Supraglacial Discharge

The discharge was used to calibrate the ETIM to the modelled discharge. Therefore, salt dilution gauging and water level measurements were made in the subperiods. With the rating curve the salt dilution gauging and the water level monitoring were combined for a continuous discharge measurement.

4.3.1 Combination of Salt Dilution Gauging and Water Level Monitoring

Water Level Monitoring

From water pressure and air pressure, the water level was determined (formula (6); Figure 22). Similar as in the ablation measurements, the discharge varies diurnally. The water level increases rapidly in the morning and peaks at mid-day. In the afternoon, the water level decreases again, however, more gradually than it increased.

Water level in subperiod 2 (July 12-13) and in subperiod 4 (August 09-10) have similar maximum water levels of around 12 l s^{-1}, whereas the water level in subperiod 3 (July 26-28) is lower. The average water level of the subperiod 2 is 8.2 cm, for subperiod 3 it is 5.1 cm and for subperiod 4 it is 7.8 cm.

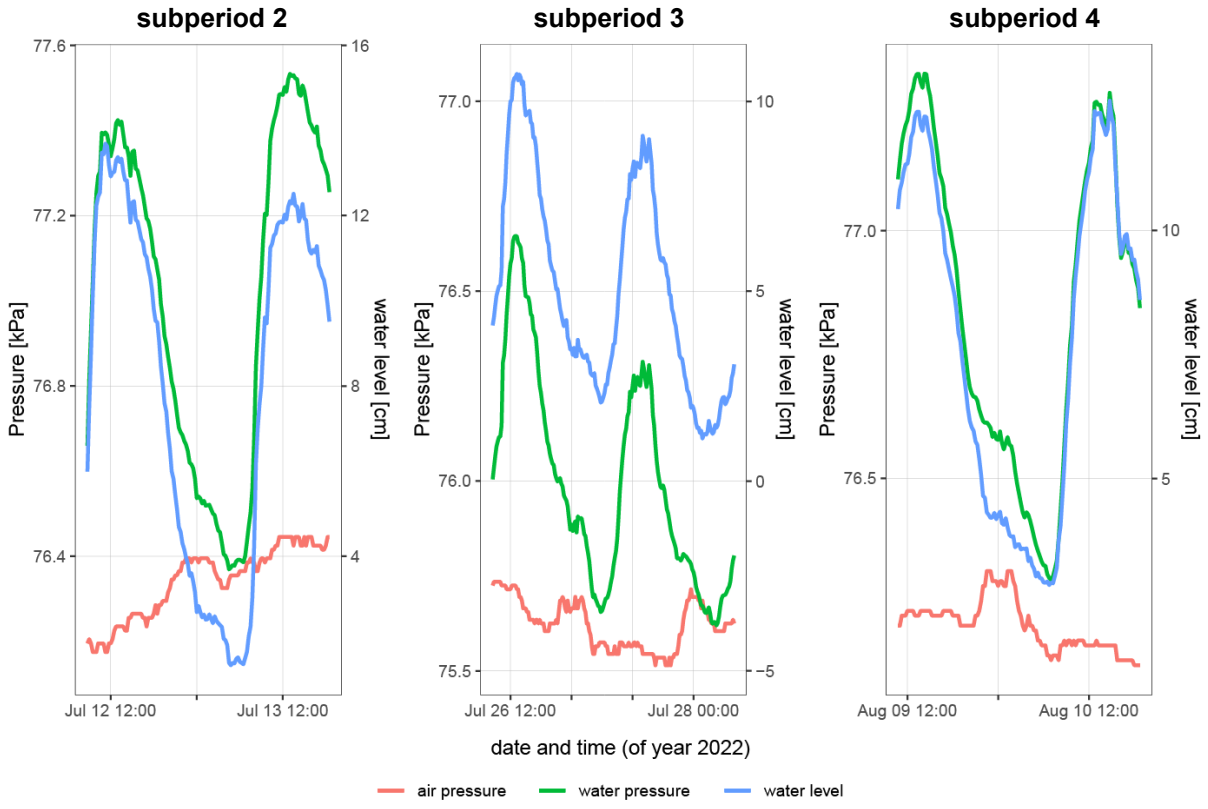

Figure 22: Air and water pressure in the measured supraglacial channel and the resulting calculated water level for the subperiods (except for June 29-30, where no water level measurements were made).

Salt Dilution Gauging

Discharge was measured intensively in a ~2-hour interval throughout the day on July 12 and August 09, using salt dilution gauging. On the other days of the subperiods, measurements were made but with a lower temporal resolution. The discharge values measured with the salt dilution gauging method are visualised in Figure 23 with Q_{meas}, which is deduced from the combination of water level measurements and the salt dilution gauging. The detailed results of the salt dilution gauging measurements and calibration parameters are found in Appendix IX.

Combining Salt Dilution Gauging and Water Level

The combination of the salt dilution gauging and the water pressure measurements through the rating curve resulted in continuous discharge estimates Q_{pot} in the subperiods 2, 3 and 4 (Figure 23). All three subperiods show a similar pattern with strong variations between morning and afternoon measurements. The two subperiods 2 and 4 show similar peak velocities of ~11-13 l s^{-1}, whereas in subperiod 3, they were larger with ~14-17 l s^{-1}. Discharge minima were in all subperiods between ~0.5 and 1.7 l s^{-1}.

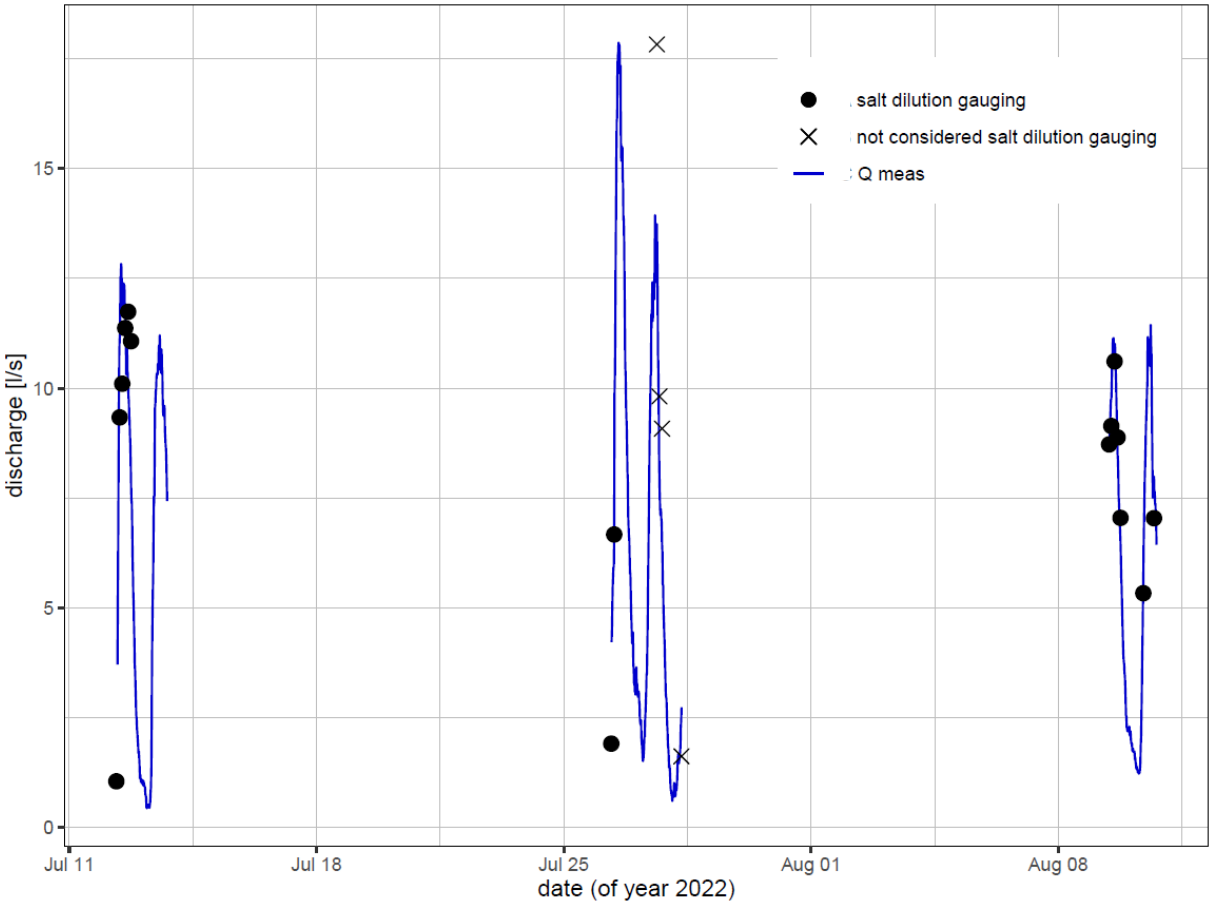

Figure 23: The modelled discharge Q from the measured water levels and salt dilution gauging with the Metrohm Conductometer and the Decagon CTD sensors measurements which were not considered for the rating curves.

4.3.2 Modelled Discharge Based on ETIM

From the ETIM, the average melt rate was modelled over time and the total potential discharge, which is the total melt of the entire catchment per second, determined. The meltwater and

precipitation were combined for a potential discharge Q_{pot} at the point of measurements (Figure 24). However, precipitation did not strongly contribute to Q_{pot}, as it there were only few rainfall events on Zmuttgletscher (Appendix X) during summer 2022. The cumulative discharge for the entire measured period is 45492 m^3, whereof precipitation only contributes 251 m^3 or 0.6%.

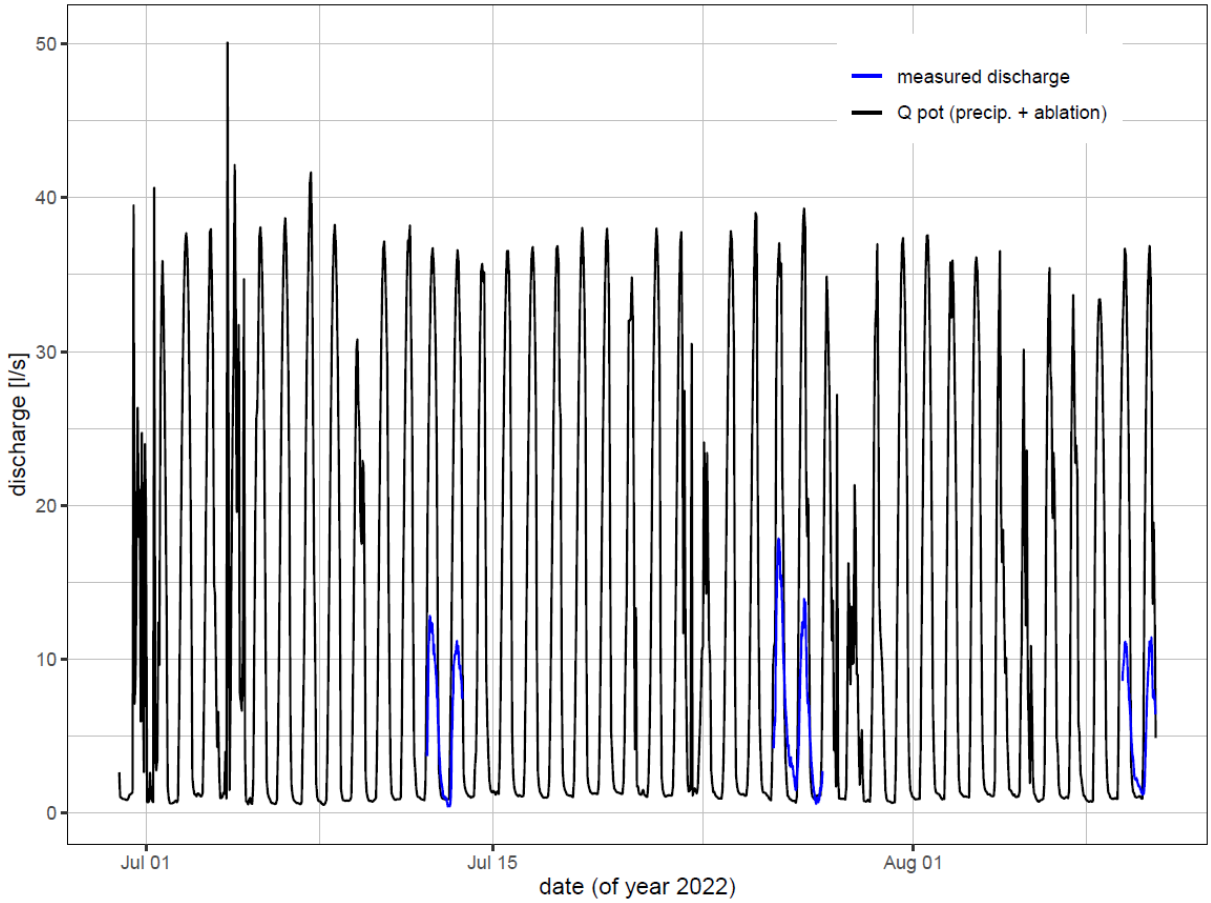

Figure 24: Measured discharge and modelled potential discharge Q_{pot} over the measurement period. The peaks of Q_{pot} are overestimated by 2/3 from the model.

Performance of Q_{pot} and Q_{mod} to Q_{meas}

In a next step, Q_{pot} was compared to Q_{meas}. Q_{meas} shows discharge peaks of 11-17 l s^{-1}. The modelled potential discharge Q_{pot}, which is the total meltwater and precipitation of the catchment per second, shows peak discharges that are approximately 3 times larger. Minimum measured discharges (0.5 l s^{-1}) are similar as the modelled ones (0.6 l s^{-1}). Q_{pot} was calibrated to Q_{meas} assuming that 2/3 of the meltwater gets lost on its way from melting to the supraglacial channel. The calibrated discharge, which corresponds to 1/3 of Q_{pot}, is subsequently called Q_{mod}. The diurnal discharge variations are well represented with Q_{mod} (Figure 25). In Q_{meas}, a left skewness is visible as the increase is rapid and the decrease more gradual than. This dissimilarity is not depicted by Q_{mod}.

Q_{mod} was plotted together with Q_{meas} of the 2nd, 3rd and 4th subperiod (Figure 25). The peaks are generally well represented by Q_{mod} with only minor divergences in the maximum discharge of ~1 l s^{-1}. In the subperiods 2 and 4 and the peak on July 27 in subperiod 3, it matches the peak of

Q_{meas} well. Q_{mod} underestimates maximum discharges on July 26 in subperiod 3. Q_{mod} generally underestimates minimum discharges at night with (by 0.5-2 l s^{-1}).

On both August 09 and 10, the increase and the peak of Q_{mod} are approximately 1 hour earlier than of Q_{mod}. Contrastingly, the peak of Q_{mod} in subperiod 2 is slightly delayed the peak of Q_{meas}. The modelled peaks in subperiod 3 represent the measured peaks well.

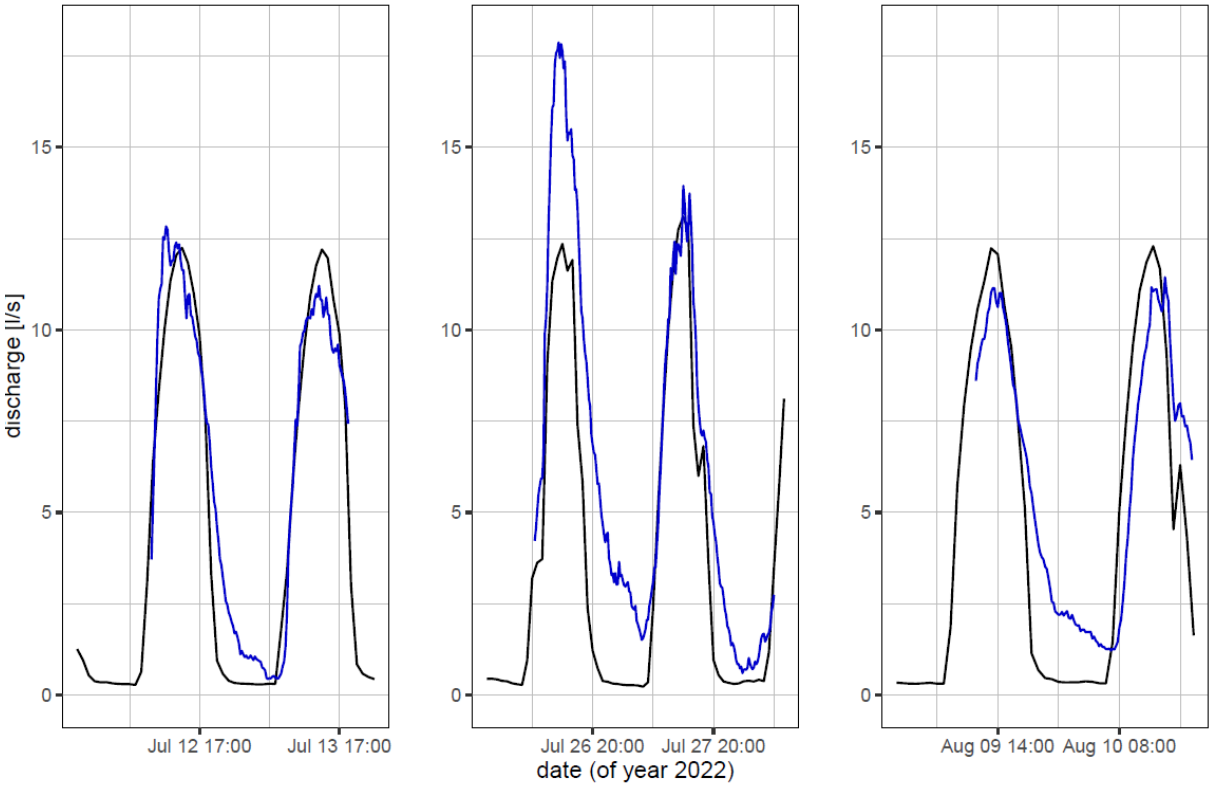

Figure 25: Short-term variation in modelled Q_{mod} (black) and measured discharge (blue). For the modelled discharge, the assumption was made that 2/3 of the meltwater get lost from the modelled potential discharge Q_{pot}.

4.4 Supraglacial Channel Incision and Ice Cliff Backwasting

The modelled discharge Q_{mod} was used to model incision rates in supraglacial channels and compare them to the measurements taken in the cross-sections. The modelled incision rates come with high uncertainties and are discussed in Chapter 5.3.

Incision and backwasting measurements at cross-sections

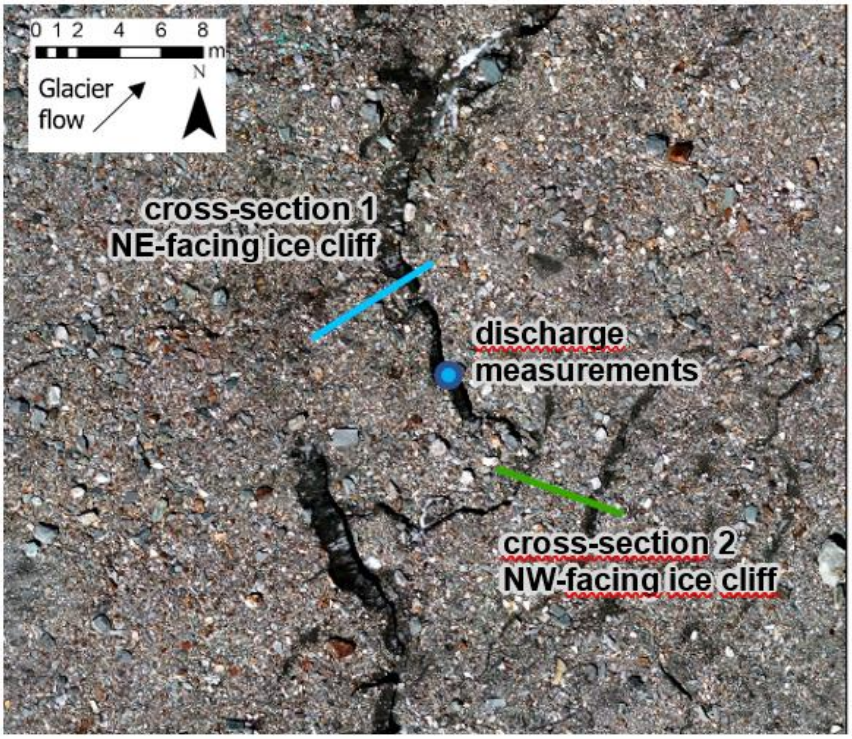

Figure 26: The two measured cross-sections along the channel. The spot where the discharge was measured is marked for orientation.

The supraglacial channel on Zmuttgletscher meanders similarly as channels on clean-ice glaciers (Pitcher and Smith, 2019). Distinct ice cliffs varying with aspect form. Two cross-sections with ice cliffs of opposing orientations were chosen to investigate in more detail (Figure 28 and Figure 27). Ice cliff 1 has an aspect of about 55° and is north-east (NE) oriented. Ice cliff 2 has an aspect of 300° and is north-west (NW)-oriented. In the NE-facing cross-section, a more accentuated ice cliff with a larger ice cliff area (upper and lower ice cliff edges are further apart) is visible in comparison to the NW-facing cross-section, where the upper and lower ice cliff edges are very close to one another. Between an aspect of 0° and 160°, ice cliffs similar to ice cliff 1 were observed. However, between 270° and 0°, ice cliffs similar to ice cliff 2 can be detected.

Cross-section 1: north-east-Facing Ice Cliff

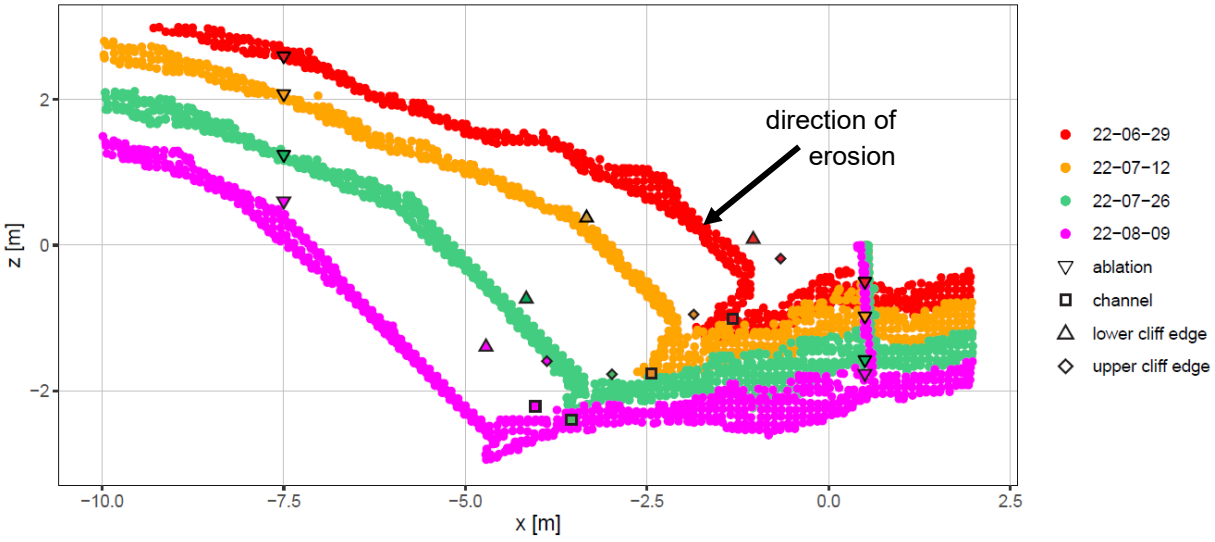

Figure 27: Change of the Laser-scanned cross-section and the hand-measured backwasting and incision of the channel at the NW facing ice cliff with time.

Cross-section 1 shows a constant incision rate of the channel in both the scan and the hand-measured data (Figure 27). The laser-scanned cross-section shows an increase in the ice cliff area as the upper ice cliff edge stays approximately at the same height while the lower edge follows the incision of the channel. The ablation measurements at the stakes match well with the surface lowering measured in the scans. However, the laser scan brings fewer uncertainties (Chapter 0). With increasing area, the ice cliff is also getting steeper. This cannot be observed in the hand-measurements.

Cross-section 2: north-west-Facing Ice Cliff

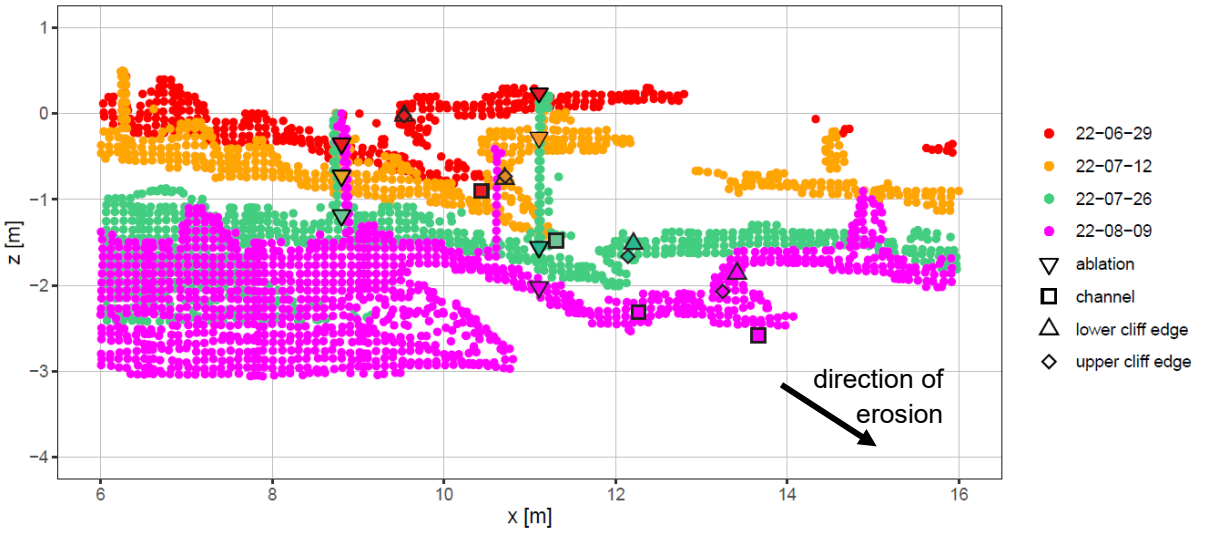

Figure 28: Change of the Laser-scanned cross-section and the hand-measured backwasting and incision of the channel at the NE facing ice cliff with time.

From June 29 to July 12 the ice cliff in cross-section 2 eroded back. Between July 12 and July 26, the NW-facing ice cliff seems to have collapsed and reformed as the ice cliff is significantly smaller

than before. At the same time, the incision and ice cliff backwasting rates are higher. In the hand-held measurements, a stronger vertical incision was measured in this period. However, this cannot be confirmed by the point cloud. Between July 26 and August 09, the shape of the ice cliff does not seem to have changed greatly and a constant melting of the ice cliff is observed.

Incision and Backwasting Rates

The lowest point of the laser scan point cloud within the area of the channel is indicated as z_{min}. The vertical incision was determined as difference of the point z_{min} with time. The horizontal incision rate is the change of the respective x coordinate at the point z_{min} with time. The resulting cumulative incision as well as incision rates are summarised in Table 7 for cross-section 1 and in Table 8 for cross-section 2, split into the x and z components. For cross-section 1, the mean incision rate (in horizontal and vertical direction together) is 7.4 cm day^{-1} and for cross-section 2, it is 9.4 cm day^{-1}.

The position of the lower ice cliff edges on both ice cliffs moves with a comparable rate as the channel incises horizontally. In the cross-section 1, a backwasting of the ice cliff is clearly visible and the ice cliff's normal vector is inclined about 45°-50°. For the cross-section 2, the ice cliff area is small. The cliff is neither visible from the UAV imagery (Figure 38). The ice cliff does not waste back but the channel rather undercuts the ice. Followingly, the ice cliff is melted away through surface ablation or the undercut ice breaks away.

The vertical incision rate in both cross-sections is relatively similar. Only for the scan of July 26, the channel in the cross-section 1 had incised 0.2 m less than the channel in cross-section 2. The total cumulative vertical incision is practically the same in both cross-sections. The incision rate $\dot{x}$ is about 1.5 times the incision rate $\dot{z}$ for the channel in the NE-facing cliff and about 2 times for the channel NW-facing cliff.

Table 7: Channel vertical incision and horizontal incision in cross-section 1 with the NE-facing ice cliff. The cumulative difference is to the first date measured (22-06-29) and the rate is for the period of the prior 2 weeks.

scanned cross-section 1 NE-facing ice cliff	cumulative Δx [m]	horizontal incision rate $\dot{x}$ [m day^{-1}]	cumulative Δz [m]	vertical incision rate $\dot{z}$ [m day^{-1}]
2022-06-29	0	-	0	-
2022-07-12	0.617	0.047	0.538	0.0414
2022-07-26	1.783	0.066	0.984	0.0365
2022-08-09	3.010	0.073	1.674	0.0408

Table 8: Channel vertical incision and horizontal incision in the cross-section 2 with the NW-facing ice cliff. The cumulative difference is to the first date measured (22-06-29) and the rate is for the period of the prior 2 weeks.

scanned cross-section 2 NW-facing ice cliff	cumulative incision Δx [m]	horizontal incision rate $\dot{x}$ [m day^{-1}]	cumulative incision Δz [m]	vertical incision rate $\dot{z}$ [m day^{-1}]

2022-06-29	0	-	0	-
2022-07-12	1.168	0.090	0.609	0.0468
2022-07-26	1.791	0.066	1.123	0.0416
2022-08-09	3.862	0.094f	1.651	0.0403

The hand-measured channel incision rates are summarised in Table 8. The hand-measurements of lower edge ice cliff do not match with the backwasting rates determined from the scans (Table 10). However, considering the low complexity and little use in equipment, the method gives a good estimate of the channel evolution.

The backwasting rate of the lower ice cliff edges is assumed to be representative for the backwasting rate of the ice cliff in general. The backwasting rate perpendicular to the surface at the lower ice cliff edge on the NE-facing ice cliff (cross-section 1) is 10.1 cm day^{-1} (extracted from the scans). For the NE-facing ice cliff (cross-section 2), this is 9.5 cm day^{-1}. Comparing this to the catchment average ablation of 3.4 cm day^{-1}, these values are approximately 3 times larger.

Comparing the backwasting rates of the ice cliffs to the incision of the channel, it is visible that these two processes are moving parallel to each other in the same direction with similar rates.

With an average supraglacial discharge of 4.0 l s^{-1} with daily peaks of approximately 12 l s^{-1} and minima of 0.5 l s^{-1}, a daily incision rate 4.1 cm day^{-1} of in vertical direction is found. The horizontal incision is dependent on the aspect, for the NW-facing ice cliff it is 6.2 cm day^{-1} and 8.3 cm day^{-1} for the NE-facing ice cliff.

Table 9: Horizontal and vertical change rates on the ice cliff and in the channel of the supraglacial cross-section measured by hand.

hand measurement	NW-facing ice cliff (cross-section 2)		NE-facing ice cliff (cross-section 1)	
	$\dot{x}$ [m day^{-1}]	$\dot{z}$ [m day^{-1}]	$\dot{x}$ [m day^{-1}]	$\dot{z}$ [m day^{-1}]
channel	0.066	0.029	0.079	0.041
lower edge	0.078	0.034	0.091	0.050
upper edge	0.090	0.036	0.095	0.045

Table 10: Horizontal and vertical change rates on the ice cliff of the supraglacial cross-section measured with from the point-cloud cross-section. The rates in the channel are in Table 7 and Table 8 and therefore omitted in this table.

	NW-facing ice cliff (cross-section 2)		NE-facing ice cliff (cross section 1)	
scan	$\dot{x}$ [m day^{-1}]	$\dot{z}$ [m day^{-1}]	$\dot{x}$ [m day^{-1}]	$\dot{z}$ [m day^{-1}]
lower edge	0.085	0.042	0.087	0.051
upper edge	0.09	0.04	0.107	0.024

5 Discussion

5.1 Ablation Measurements

Melt Rate of Zmuttgletscher in Comparison to other Debris-Covered Glaciers

The mean ablation rate measured was 3.4 cm day^{-1}. Differences in melt rate between the stakes were observable. Furthermore, melt rates differed between night and day. The diurnal variations in both measured and modelled ablation are induced by the change of temperature and shortwave incoming radiation (Pellicciotti *et al.*, 2005; Carenzo *et al.*, 2016). The conditions over the entire measurement period are relatively similar. As the modelled ablation is directly dependent temperature and incoming shortwave radiation, few days with lower ablation rates were modelled which correlate with lower incoming shortwave radiation rates and lower temperatures.

The melt rates of Zmuttgletscher in 2022 are compared to the melt rates of Zmuttgletscher in 2021 and to those of other debris-covered glaciers in Figure 18. The melt rates on Zmuttgletscher were those of the other glaciers and decreased with increasing debris-cover. This matches with the commonly observed relationship (Anderson and Anderson, 2016, Østrem, 1959). In comparison to the melt rates in 2021, the melt rates of 2022 were distinctly higher. This can be explained by warmer temperatures (Figure 14) throughout the measurement period.

Surface Difference from UAV DEMs

The mean catchment melt rates deduced from the DEM difference are an independent measurement which fits to the catchment average ablation measured on the ablation stakes. This indicates that the average ablation measurements, to which the ETIM is calibrated, represent the catchment well. Ablation from the DEM difference, however, could only be determined with a coarse temporal resolution (2-weeks in this thesis), which is why ablation stake measurements were needed for a higher temporal resolution.

In the DEM difference, the spatial variance of ablation is visible. Average ablation in proximity to the channel is higher than in areas further away from to the channels. On the orographic right side, a generally higher ablation rate is visible than on the left side, indicating that surface slope may influence ablation. This correlation was already found in other studies (e.g. Mihalcea *et al.*, 2006). Another reason for the higher melt rates on the right side could be the formation of small channels.

Over the entire timespan, the area around the channels shows a lower average ablation than within the 2-week differences of the DEMs (Appendix I, Appendix II, Appendix III). It shows that local melt hotspots are not staying in the same place but are moving on the surface through the incision of the channels and backwasting of the ice cliffs (Kneib, Miles, *et al.*, 2021).

Melt Rate and Debris Cover Thickness

Ablation rates decrease as expected (Østrem, 1959) with an increasing debris cover thickness. The behaviour seems similar when compared to other studies (Figure 18). However, the variation in debris cover thickness in the investigated catchment on Zmuttgletscher is relatively small and does not vary greatly as opposed to other studies (e.g. Nicholson and Benn, 2013; Carenzo *et al.*, 2016; Miles *et al.*, 2022). It was observed that debris cover thickness cannot be the only influence on the difference in ablation, but the slope aspect and proximity to the supraglacial channel could

play a role as well. This finding was also made by Mihalcea *et al.* (2006), who state aspect and slope as equally important factors as debris cover thickness influencing sub-debris melt.

Not only had debris cover thickness an influence on the melt rate but a correlation between the aspect and the melt rate was detected. The melt rates on the right side of the channel were higher than on the left side (Appendix VII, Appendix VIII). On both sides of the glacier, the slopes ascended towards the medial moraines, even though the right side is generally flatter than the left side. This means that the two sides have different aspects which could influence the melt rate. However, as the focus is on the average melt rate of the catchment, this correlation was not further investigated. Neither is the spatial variation of the debris-cover thickness nor its influence on the melt rate included in the input for the discharge model, as the input for the discharge estimation did not need to be in a spatially high resolution and an average insulating factor was sufficient. If the interest lies on a spatially high resolved model, then this factor should be considered.

Uncertainties of the Ablation Stake Measurements and DEM Surface Difference

The ablation stake measurements are expected to have a small error. As the measurements were done systematically with the ablation disc, measurement uncertainties for this method are relatively small. From repeated consecutive measurements, a deviation of $\pm 0.25\,cm$ was determined. Uncertainty tends to increase with an increased grain size of the local debris.

However, some further uncertainties arise with the ablation stake measurement which are hard to quantify: To drill the ablation stakes into the ice, the debris had to be removed. After the ablation stake was put in the ice, the spot was covered again with debris. The newly covered stake potentially has a different debris cover thickness than the immediate surroundings. This could lead to an incorrectly assumed debris cover thickness for a stake showing a certain melt rate and thus influence the average debris-cover and the Østrem correlation. Furthermore, some ablation stakes melted out completely or threatened to melt out, thus new stakes were installed as close to the old locations as possible. To include these measurements in the model calibration and to put them in context with the entire period, the best solution was subtracting the previous ice loss. This leads to a potential error. In addition, the average ablation (used to calibrate the ETIM) is dependent on the distribution of the ablation stakes over the catchment. The resulting average may not be the real average on the ice surface. The average ablation rate (for both space and time) from the ablation stakes was compared to the average ablation rate on the DEM surface difference and the discrepancy is relatively small, indicating that the biases coming with the hand measurements are relatively small.

As previously described, some ablation stakes close to the channels were not considered for the ETIM because these stakes were stabilised in a pile of rocks making measurements difficult and unprecise or were directly influenced by channels. In the latter case, the channel could either melt completely or partly through the stake making the stake fall into the channel (Figure 29). If an ablation stake got into the ice cliff front, where the local debris cover thickness changes, the melt rate suddenly increased strongly. To minimise unwanted influences and uncertainties, these stakes were omitted for the ETIM calibration.

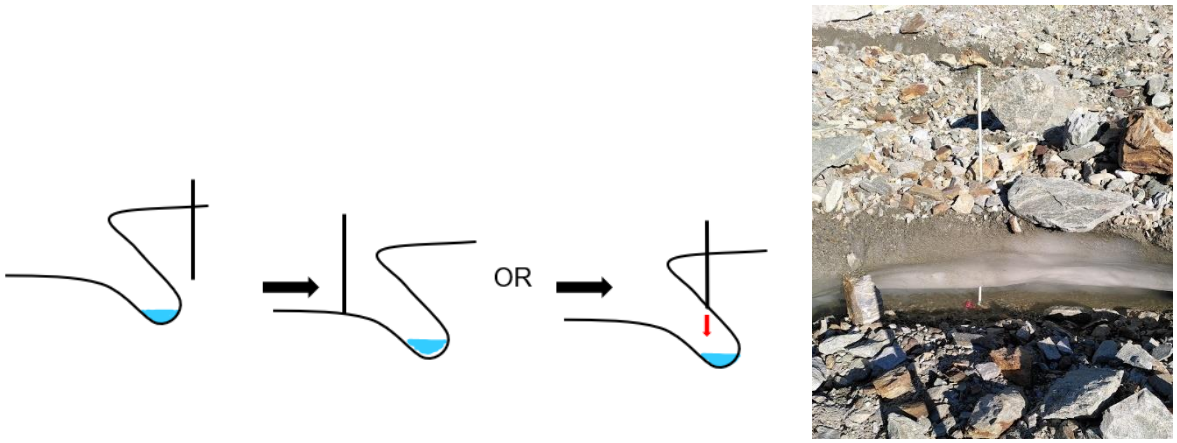

Figure 29: (a) Channel incision through the ablation stake, leading to increased ablation values through melt-through. (b) The melt-through observed in the field on Zmuttgletscher.

Furthermore, for the DEMs, there are uncertainties that come up with the acquisition of the UAV imagery. Considering the time spans, uncertainties are comparably small. The uncertainties of the camera position of the UAV acquisition are summarised in the following table:

Table 11: Uncertainties of the camera position of the UAV which lead to uncertainties in the DEMs.

	X error [cm]	Y error [cm]	Z error [cm]	XY error [cm]	Total error [cm]
22-06-29	2.047	6.962	7.902	7.257	10.729
22-07-12	6.513	5.725	9.519	8.671	12.876
22-07-26	1.575	1.570	1.691	2.224	2.794
22-08-09	11.801	8.485	16.033	14.535	21.641

The DEMs were co-registered to minimise errors through the downslope movement of the glacier. However, in the DEM (Figure 19), artefacts from boulders are still visible that influence the surface elevation difference but are not ablation.

5.1.1 ETIM Sensitivity Analysis

The aim of the ETIM was to model spatially averaged ablation rates of the catchment. Small-scale spatial effects like different debris cover thicknesses or a different aspect leading to local differences in melt rates are not important for averaged melt rate (Anderson *et al.*, 2021) and are included in the empirical parameters F_{ins}, F_{SW} and F_T. The long-term ablation trend seems to be mostly driven by temperature.

The process of the ice cliff backwasting is generally not considered in the ETIM, as it is a different process than surface sub-debris melt. However, the backwasting and channel undercutting process are still contributing to the total ablation and thus also to the discharge that is in turn important for the incision rate of the channel. However, this process was neglected for the ETIM and the average ablation is assumed to be larger than calibrated to the ablation stakes. As channel areas are relatively small in comparison to the total catchment, this process was neglected for the model calibration.

As the ablation in proximity of the channel is observed to be higher than elsewhere, the modelled discharge Q_{pot} should therefore be partly underestimated. It is clear, however, that Q_{pot} was

eventually largely overestimated. For further research, the two processes should be separately applied and then combined.

Not considered in the ETIM was the delay of atmospheric signals through the debris layer (Reid and Brock, 2010; Carenzo *et al.*, 2016). This could be considered including the thermal conductivity of debris which lies between 0.35 to 0.94 (Reid and Brock, 2010). However, comparing the melt rate modelled with the ETIM to the measured discharge, delays due to debris transmission seemed to be minor and were neglected in this thesis.

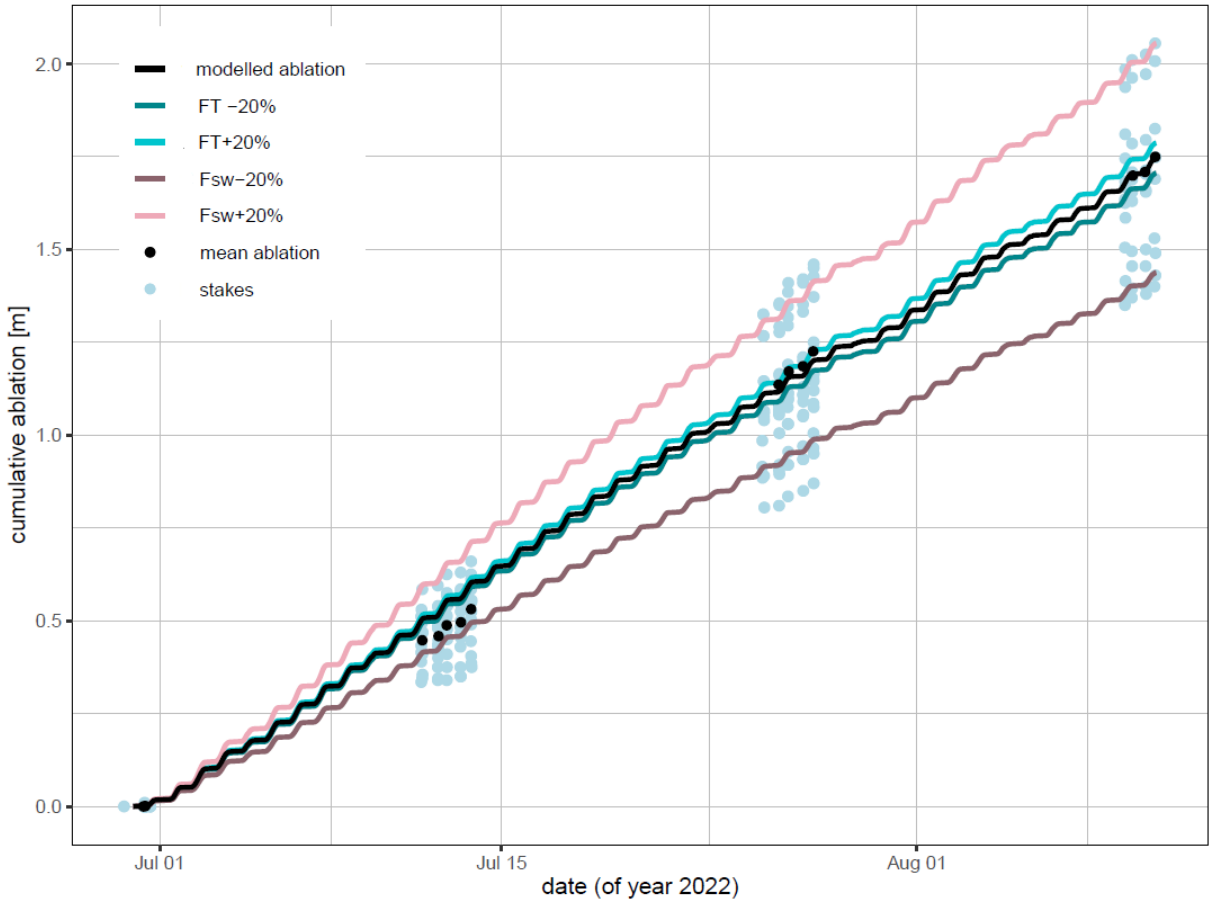

Figure 30: Sensitivity analysis of different F_{SW} with the same F_T and vice versa. Modelled ablation stands for the best fit for 09-10 August which was used for the further modelling.

The sensitivity of F_{SW} and F_T for the model of the best fit was evaluated. F_T used by Gabbi et al. (2014) range from 0.00 to 0.25 and F_{SW} between 0.0012 and 0.0100. Pellicciotti *et al.* (2005) tested the sensitivity for F_T between 0.01 and 0.09 and F_{SW} between 0.002 and 0.017 and their optimal parameter combination is $F_T = 0.05$ and $F_{SW} = 0.0094$ on a clean ice glacier. Carenzo *et al.* (2016) have optimal parameters $F_T = 0.0984$ and $F_{SW} = 0.0044$ for 5 cm debris cover thickness and $F_T = 0.0660$ and $F_{SW} = 0.0023$ for 10 cm debris cover thickness. As a comparison, the optimal parameter combination for the model applied to Zmuttgletscher is $F_T = 0.03218$ and $F_{SW} = 0.01106$ for an average debris cover thickness of 7.8 cm. The values used in this thesis are significantly smaller than those used by Carenzo *et al.* (2016).

Both parameters were decreased and increased by 20% while the other parameter stayed the same (

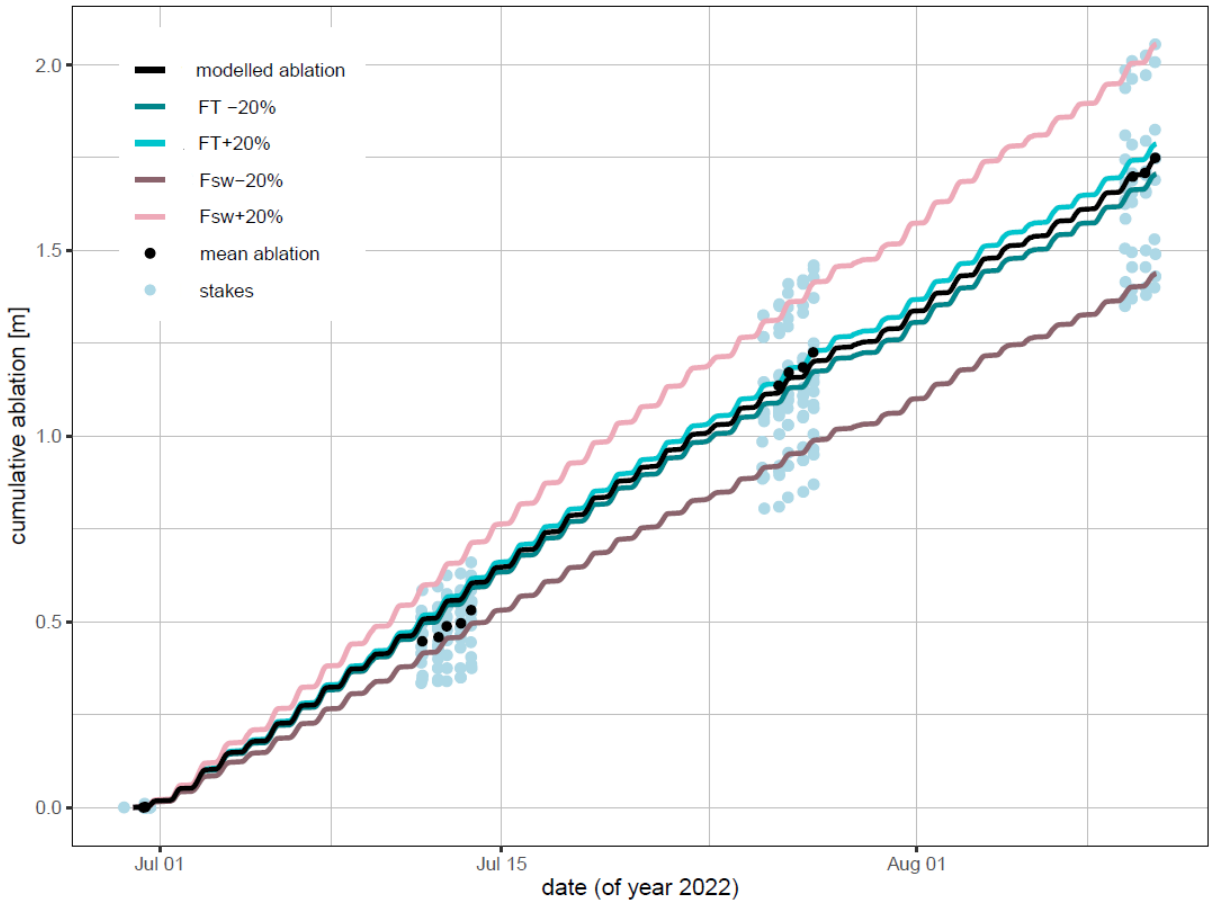

Figure 30). This created a range for F_{SW} of $0.008848 - 0.013272$ and for F_T of $0.025744 - 0.038616$. The variability in ablation for a changed F_{SW} is clearly larger than for a changed F_T. The sensitivity of the *SW*-term is therefore high. Therefore, the ablation modelled with the ETIM depends significantly more on the shortwave incoming radiation than on temperature on the debris-covered Zmuttgletscher. The same finding was made by Pellicciotti *et al.* (2005) on a clean ice glacier.

Additionally, the ideal parameter combinations of studies from Pellicciotti *et al.* (2005) and Carenzo *et al.* (2016) were applied to the meteorological data of Zmuttgletscher and compared to the parameter combination of the best fit. Carenzo *et al.* (2016) give different parameter combinations for different debris cover thicknesses. As the average debris cover thickness in the investigated catchment on Zmuttgletscher is 7.8 cm, the parameter combination of 5 cm and 10 cm by Carenzo *et al.* (2016) were compared, resulting in melt rates of 5.3 cm day^{-1} and 3.2 cm day^{-1}, respectively. Therefore, going with the parameter combination for a debris cover thickness of 5 cm slightly underestimates the ablation rate of the stake with the least ablation of 3.5 cm day^{-1} with a debris cover thickness of 8.3 cm (A3) and stake with most ablation of 5.0 cm day^{-1} (A9) with 6.3 cm debris cover thickness. It is important to mention again, that debris cover thickness is not the only factor determining the ablation and therefore, not the stakes with the thickest debris cover thickness is automatically the stake at which smallest ablation rates were measured and vice versa. Comparing the parameter combination of Pellicciotti *et al.* (2005) with the modelled ablation of Zmuttgletscher assuming F_{ins} to be 1, a similar result is obtained.

In general, the modelled ablation on Zmuttgletscher is well comparable to the parameter combinations of the other studies and is therefore expected to be reliable.

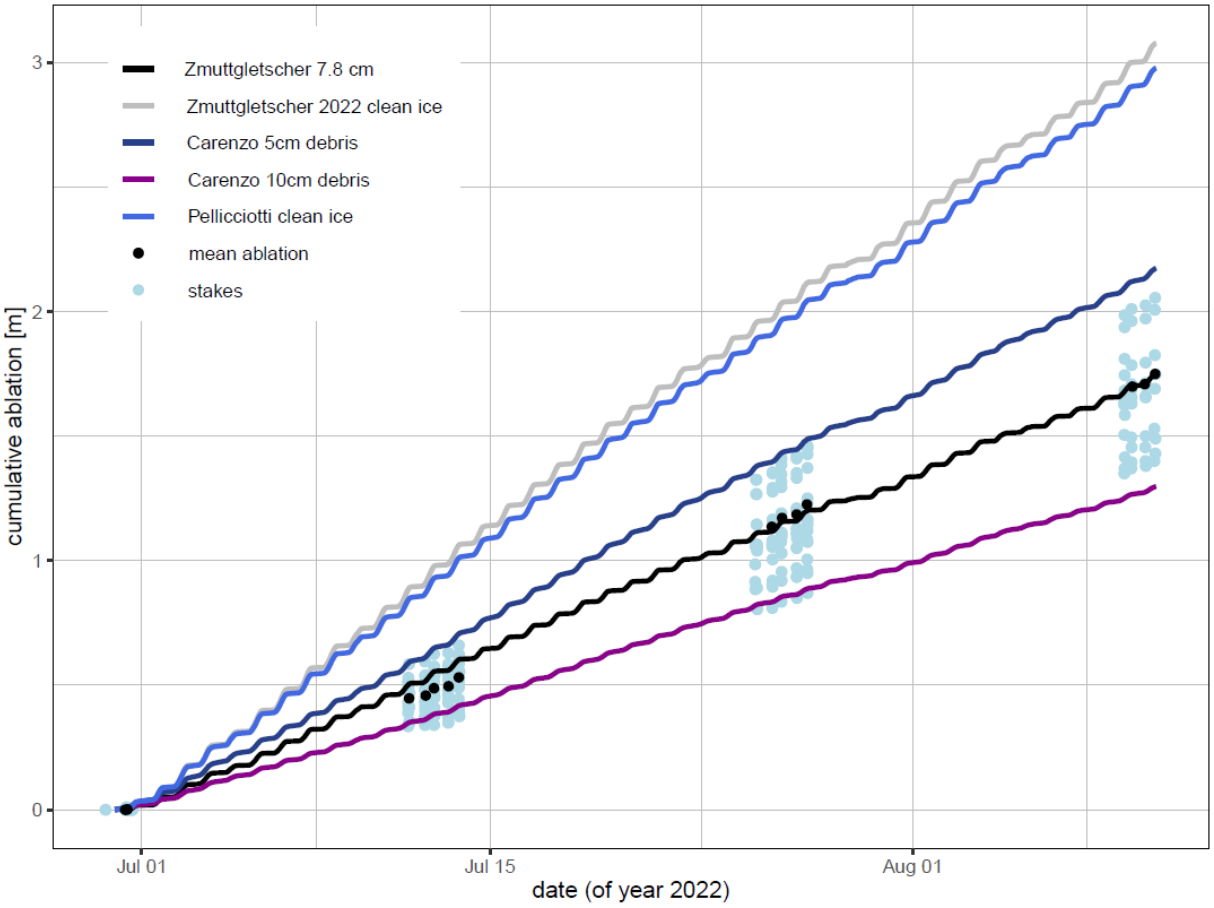

Figure 31: The modelled mean ablation for an average debris cover thickness of 7.8 cm, the best fitted model without the insulation factor (clean ice) and the best fitting model parameters of the studies of Carenzo et al. (2016) and Pellicciotti et al. (2005) applied to the meteorological data measured on Zmuttgletscher in 2022.

Furthermore, the sensitivity of the insulating factor of the debris cover was tested. The insulating effect of the minimum and maximum debris cover thickness measured at the stakes were implemented in the ETIM and compared, as well as the model without any insulating effect, i.e. if Zmuttgletscher was a clean ice glacier (Figure 32). The cumulative ablation of the modelled clean ice (3.077 m) represents the total amount of vertical ice loss in the ice cliffs measured in the DEM difference (2.998 m) quite well, however, still overestimates the vertical backwasting rates of the measured ice cliffs (2.0 m). With the minimum debris cover thickness, which is also the minimum insulation, the stakes with the strongest ablation were relatively well depicted and vice versa for the stakes with least ablation. However, the stakes with the highest ablation rates and the ones with the lowest do not necessarily have the highest or lowest debris cover thickness, respectively.

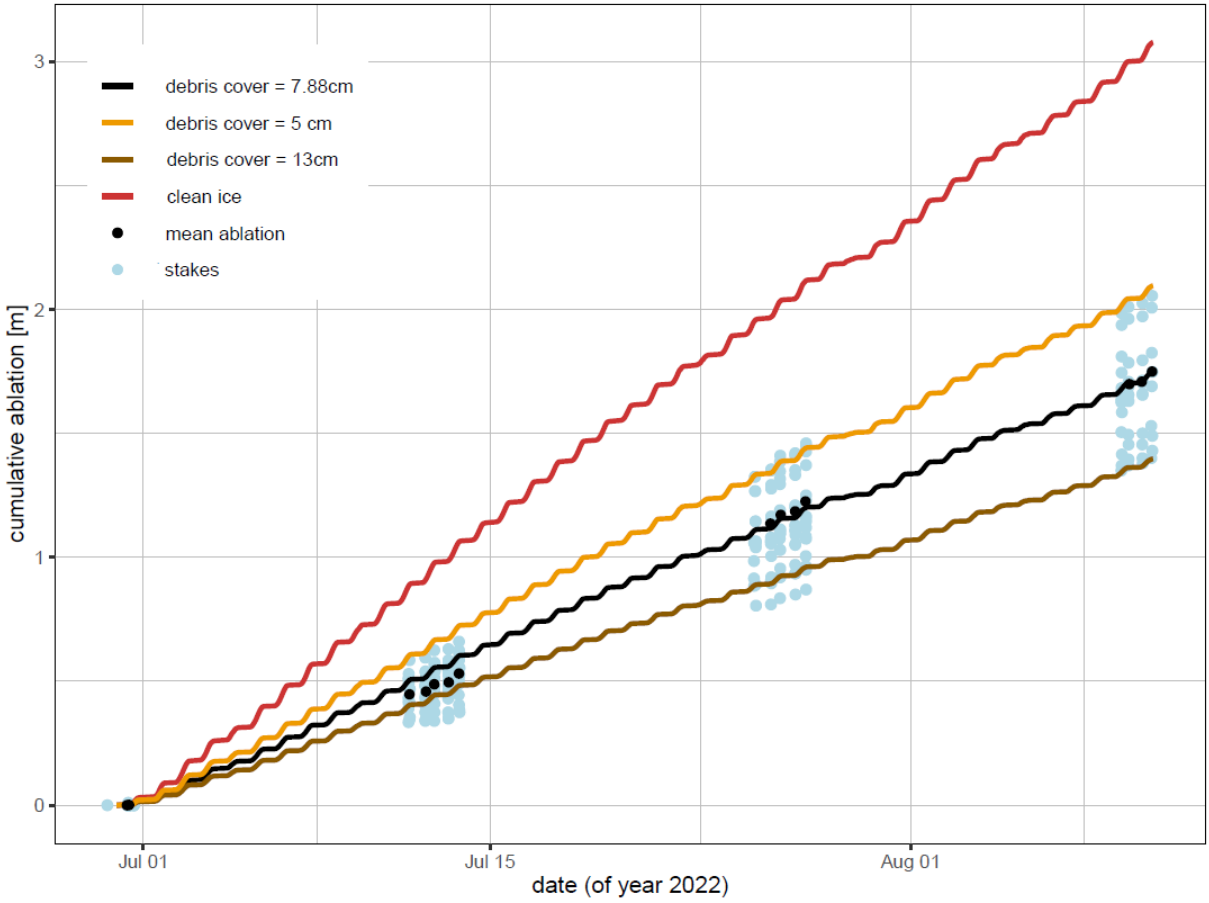

Figure 32: Sensitivity analysis of different the minimum (5 cm) and maximum (13 cm) debris cover thickness and for clean ice. Modelled ablation stands for the best fit for 09-10 August which used an average debris cover thickness of 7.88 cm.

5.2 Discharge

Diurnal Discharge Pattern and Performance of Modelled Discharge

Discharge was measured with salt dilution gauging and water level measurements and was modelled on the basis of the ETIM. Diurnal changes in the measured discharge Q_{meas} are visible. During the day, incoming shortwave radiation and temperatures increased, which enhanced ablation and resulted in a higher supraglacial discharge, while at night, temperatures were lower and shortwave radiation decreased to zero, which again decreased the ablation and accordingly the discharge. For this reason, the diurnal variations are also well visible in the modelled discharge. However, the uncalibrated modelled discharge Q_{pot} overestimates the peaks of the measured discharge by a factor of 3 (Figure 24). Therefore, it was calibrated to the measured discharge, assuming that only 1/3 of the melt water is actually flowing into the stream. The calibrated discharge Q_{mod} depicts diurnal variations and peaks well. Moreover, Q_{mod} is plotted against Q_{meas} in Figure 33. The discharge seems to be underestimated in general by about 1.25 l s^{-1}. For comparison, the 1.25 l s^{-1} were added to Q_{mod} and plotted with Q_{meas} over time (compare Figure 25 and Appendix XI), however, discharge peaks still seemed to be better represented by Q_{mod} and therefore, no further correction was made.

Generally, the discharge and its diurnal fluctuations can be modelled from an ETIM in a determined catchment, however, the discharge peaks need calibration. Even with calibration, small divergences between the measured and the modelled discharges are seen, minimum discharges tend to be underestimated and short-term fluctuations on a smaller scale than a few hours are barely represented. Over the total investigated time, these divergences should play a minor role and therefore not strongly influence the theoretically modelled incision rates.

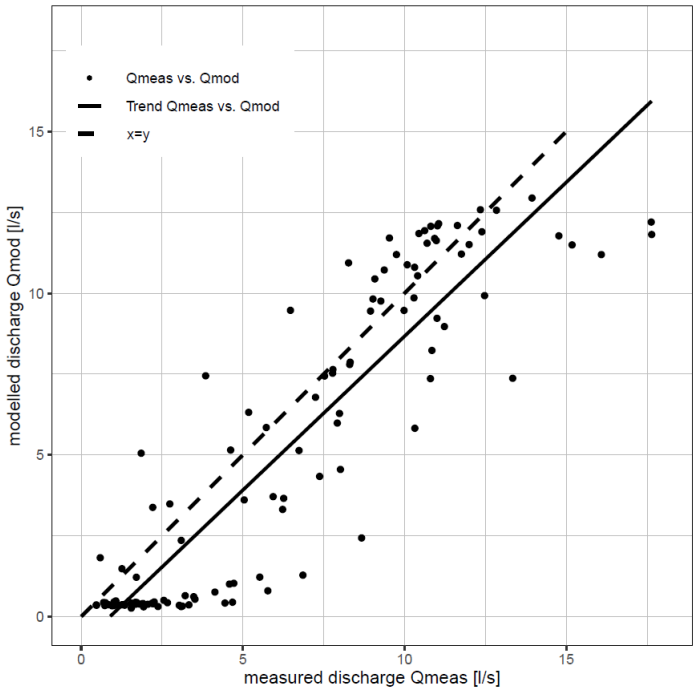

Figure 33: Q_{mod} plotted against Q_{meas}. The trendline of the data is visualised with a solid stroke, for a perfect fit, the data would lie on the dashed line.

Discrepancy Between Modelled Potential Q_{pot} and Measured Discharge Q_{meas}

The uncalibrated discharge Q_{pot} overestimated measured discharge peaks largely, so it was assumed, that 66% of the meltwater does not flow into the supraglacial channel, where discharge was measured. This assumption is not universal but needs calibration on individual supraglacial catchments and is not adaptable for other glaciers. Furthermore, the reasons to explain the loss are diverse, for instance meltwater could flow in a permeable near-surface layer of the glacier (Fountain and Walder, 1998) and not flow into the supraglacial channel. Small crevasses or microfractures could lead meltwater into the glacier or subglacial (Fountain and Walder, 1998). Evaporation of the surface ablation could also reduce the subsurface meltwater flow. However, Evatt *et al.* (2015) investigated ablation through evaporation on debris-covered glaciers and concluded that this effect is minor. Smith *et al.* (2015) found in their study, in which they modelled surface drainage from a regional atmospheric model and DEMs, that their modelled discharge also overestimated the discharge and supposed, that the incorporation of subglacial processes is important for runoff estimates. The catchment determined from the DEM suggests that the meltwater flows into the main channel. However, the DEM-defined catchments are created from the debris-covered surface. Hence, the mapped catchments could differ from the sub-debris surface flow and meltwater could flow in different paths.

Limitations of Q_{mod}

First of all, Q_{mod} needs calibration against the modelled catchment. The transferability should be assessed by modelling the discharge on other glaciers and in other melt seasons.

Precipitation does not greatly contribute to the total discharge of the measured period. The assumption was made that precipitation is uniform over the entire catchment because the size of the catchment is very small. Nevertheless, there could be small scale undulations. There have not been any continuous measurements during a rainfall event, so the reaction of the catchment on rainfall could not be determined. The assumption was made, that it uniformly contributed to the discharge in the same way as the surface ablation did. Since precipitation was rare, this should not heavily influence the modelled discharge.

The delay caused by the debris-cover was not incorporated in the ETIM on Zmuttgletscher. Carenzo *et al.* (2016) do not incorporate any lag in their melt model for debris cover thicknesses of 5 cm either, for a thickness of 10 cm, they used a delay of 1 hour. As the average debris cover thickness in the investigated catchment on Zmuttgletscher is 7.8 cm, a delay of 0-30 minutes could be expected. The ETIM used for this thesis does not consider the delay in melt induced by of the debris cover. Nevertheless, the peaks of the modelled discharge Q_{mod} match relatively well with the peaks of the measured discharge.

The measured discharge showed a left skewness and a more gradual decrease than increase. To incorporate these factors into the modelled discharge, a Gaussian correction could have been applied (Cicoira *et al.*, 2019). However, as this had needed a parameter calibration, it would have brought up additional uncertainties. Due to the uncertainties and the already decent model representation of the measured discharge, a Gaussian correction was omitted.

Moreover, the catchment area is based on the DEM of July 26 with 1 m resolution. Choosing a DEM a different date or a different resolution may have resulted in different discharge estimates. The catchment determined from the DEM of August 09 with a 1 m resolution and the catchment of July 26 with a 2 m resolution is in the Appendix. The difference in area between the used catchment and the catchments determined from another date and other resolution is small with only ~1%.

Limitations of Q_{meas}
Not only is the modelled discharge overestimated but also measured discharge could be underestimated. It is likely that not all of the salt dilution flew downstream during the measured period (Day, 1977). Hence, it can be assumed that the discharge was always slightly overestimated. The bias is hard to quantify in the investigated catchment on Zmuttgletscher. However, it most likely does not compensate for the total divergence.

In the 3rd subperiod, only 2 measurements to calibrate the rating curve with were made. The water level of this subperiod it is lower than in the other two periods, whereas the modelled discharge in this period turns out higher. As the amount of salt dilution gauging measurements used to calibrate the discharge in this period was small, the Q_{meas} of subperiod 3 is expected not to be as reliable as the Q_{meas} from the other subperiods. Having several subperiods with Q_{meas} increases the reliability for the calibration of Q_{mod} to Q_{meas}.

5.3 Supraglacial Channel Incision and Ice Cliff Backwasting

Zmuttgletscher shows similar melt hotspots along the supraglacial channel as other debris-covered glaciers (e.g. Buri *et al.*, 2016; Kneib, Miles, *et al.*, 2021; Sato *et al.*, 2021). Additionally, at the glacier terminus, massive ice loss was qualitatively observed in the field campaigns. However, there are no ponds.

Channel undercutting and ice cliff backwasting along the channels are well developed. These two processes were measured in two cross-sections and set into context of modelled incision rates. Vertical incision was modelled by two different models. The ice cliff backwasting follows the channel incision.

5.3.1 Channel Incision Modelling

Channel incision from Observations
The observed channel incision rates are divided into the horizontal and vertical incision components. The vertical incision rate components are similar in both cross-sections and the channel incised approximately 4 cm day^{-1}. Other than the vertical incision rate component, the horizontal component varies slightly with aspect, being ~7 cm day^{-1} for cross-section 1 and ~ 9 cm day^{-1} for cross-section 2. The ice cliff backwasting rates components are similar as those of the channel incision. The observed horizontal component of the ice cliff backwasting at the lower edge (cross-section1: ~8 cm day^{-1} and cross-section 2: ~9 cm day^{-1}) also differ slightly with aspect. So do the ratios of horizontal to vertical incision components between the cross-sections. In both cross-sections horizontal incision rate is higher than the vertical incision rate by a factor of 1.5 to 2.

Even though the incision rates are similar in both catchments, in cross-section 2, almost no ice cliff area is observed, whereas in cross-section 1, the ice cliff area is large (i.e. upper and lower ice cliff edges are distinctly apart). This suggests that the channel undercutting is not influencing the size of the ice cliff area. Aspect seems to be more decisive, as the shortwave incoming radiation is varying with aspect. Nevertheless, the backwasting rates of the lower ice cliff edges are similar to the incision rates of the channel, suggesting that the channel dictates the movement of the ice cliff.

In general, the horizontal incision rate is about 1.5 to 2 times as high as the vertical incision rate for the measured cross-section 1 and cross-section 2, respectively. The high horizontal incision rates could come from the meandering of the stream, which induces a horizontal incision on the impact on the convex channel bank (Pitcher and Smith, 2019).

With the channels undercutting sideways, the ice cliff is overhanging the channel. While the inclined ice cliff is backwasting, debris resting on top is falling into the channel. It is conceivable that debris deposited on the opposite side of the channel could additionally push the water, enhancing the lateral incision (Figure 34). The debris deposits in the channel slimmer the length scale on which the erosive potential of the water acts, enhancing incision rate per unit length. The mentioned debris deposition has been observed in the field along most undercut channels. The connection between the amount of debris and the rate of horizontal incision in the channel has to be investigated more thoroughly to make a clear statement.

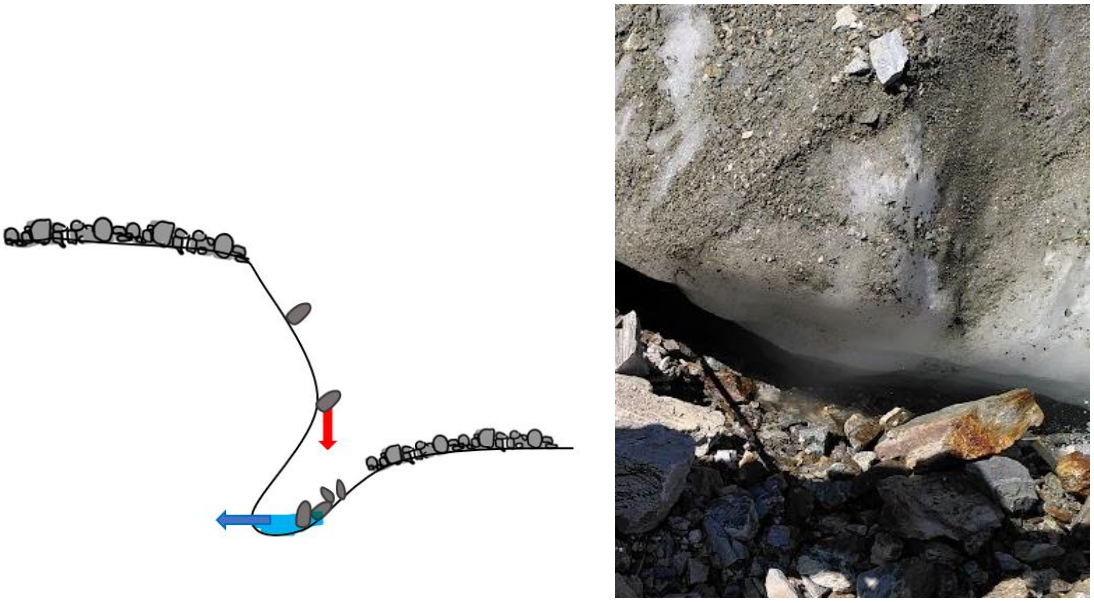

Figure 34: (a) Sketch of the debris that falls off the ice cliff pushing the water flow additionally sideways. (b) frontal view of an ice cliff with debris and boulders sliding into the underlying channel.

Limitations of the Hand-Measured Incision and Backwasting

The hand-measurements of the erosional processes in the cross-sections brings limited precision and considerable inaccuracies, especially with the angle measurements. The technique can be a good method to estimate trends. However, various independent and repetitive measurements of the same cross-section are needed to have a more reliable result. The laser scans offer a more objective method to observe the evolution of the ice cliffs. They have a spatial error of 1 cm. As the point cloud is 3 dimensional, the profile does not result in one perfect line but gives various points, increasing the uncertainty of measurements such as the determination of upper and lower ice cliff edge and channel incision.

Theoretical Incision Based on Model A

Channel incision was attempted to estimate with two different approaches on the basis of the supraglacial discharge. The theoretical incision of formula (9) describes the downcutting rate, i.e. vertical incision component, based on heat dissipation. The main input parameters are discharge,

hydraulic slope, Manning's roughness coefficient, latent heat of melting and gravitational acceleration. Including the gravitational acceleration, the model describes only the vertical incision rate component ($\dot{z}$) and not the total incision rate ($\dot{x}z$). The hydraulic slope along the channel was measured along the flow path but is not well constrained. This brings some uncertainties. Furthermore, the estimation of Manning's roughness coefficient is difficult, as it is rather variable and occasional debris in the channel further obstructs the flow. To assess the sensitivities to these parameters, the cumulative incision is visualised for different of these parameters (Figure 35).

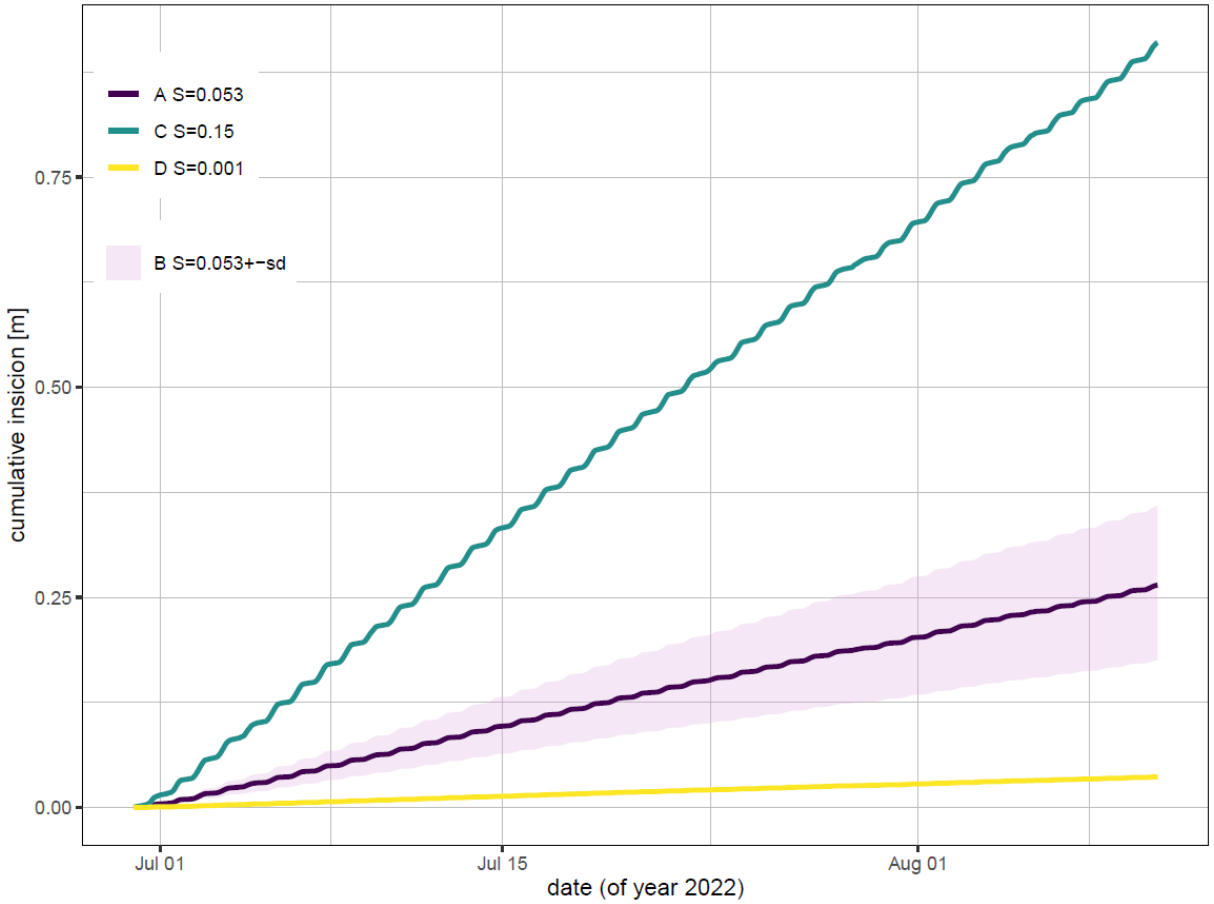

Figure 35: The modelled cumulative incision from the modelled discharge using the model introduced by Fountain and Walder (1998) which uses different hydraulic slopes S and a constant Manning's roughness coefficient of ñ=0.01.

The slope was measured in the DEM along the mapped channel. For a hydraulic slope S of 0.053 ± 0.015, an incision rate of 6.45 mm day^{-1} is modelled. The maximum possible slope is $S = 0.15$ along the straight flowline of the glacier. This corresponds to an incision rate of 22.19 mm day^{-1}, which is still only half of the incision measured. A constant Manning's roughness of $\tilde{n} = 0.01$ s m$^{-1/3}$ is used. With an increasing S, the incision rate increases, as there is more potential energy available (Table 12).

Table 12: Resulting incision rates and cumulative erosion using different hydraulic slopes S in the model FW. The timespan for the cumulative incision is 41 days.

S	incision rate [mm day^{-1}]	cumulative incision [m]

0.053±0.015	6.45± 0.15	0.265 ± 0.061
0.01	0.89	0.037
0.15	22.19	0.904

As the discharge Q_{mod} is one of the model input parameters, the general pattern is similar with varying parameters and resembles the cumulative ablation. Hence, a higher incision rate during the day than at night is visible in the model result.

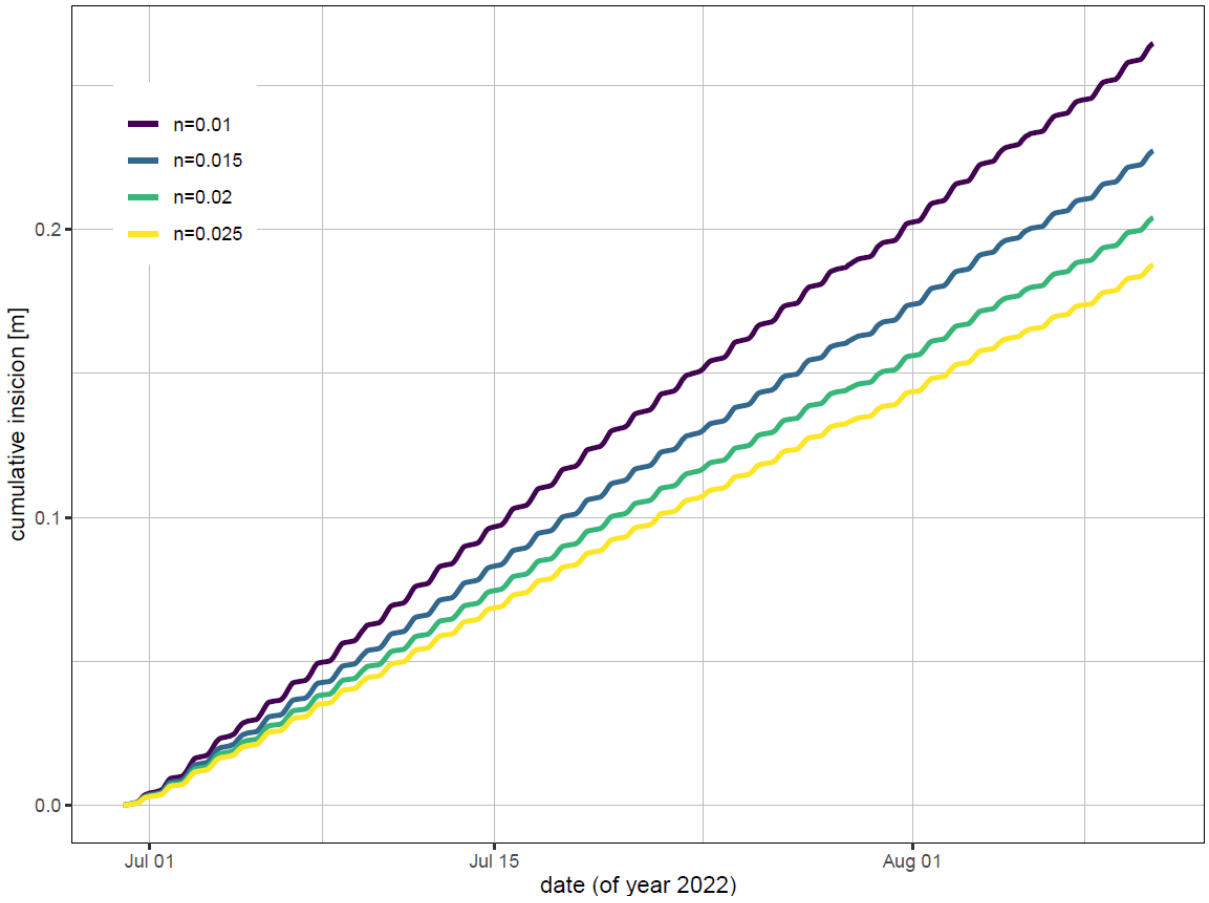

Figure 36: The modelled cumulative incision from the modelled discharge using the model proposed by Fountain and Walder (1998) using different Manning's roughness coefficients ñ in 0.005 steps. A constant slope S of 0.053 is assumed.

The sensitivity of the Manning's roughness coefficients *ñ* was assessed with a constant $S = 0.053$ over time (Figure 36). Values between 0.01 is for a smooth (clean-ice) channel (Fountain and Walder, 1998) and maximum expected channel roughness values (Church, 2006) were explored. No studies about Manning's roughness coefficient in channels on debris-covered glaciers were found. A maximum possible ñ of 0.25 s $m^{-1/3}$ was assumed based on Church (2006), who investigated proglacial streams, and Engineering ToolBox where different ñ for different surfaces are classified (*Engineering ToolBox. Manning's Roughness Coefficients.*, 2004). With an increasing ñ, the incision rate decreases (Table 13) as ñ is inversely proportional to the flow velocity (Pitcher and Smith, 2019). However, the general variance of the incision rate is small and underestimates observed incision rates greatly.

On a debris-covered glacier, one could assume that the debris in the channel has an additional erosive effect. However, the increasing roughness decreases modelled flow velocities and therefore decreases also incision rates. Sediments have been observed to have an additional abrasive effect and can increase channel incision (Church, 2006; Pitcher and Smith, 2019). However, this is not included in the theoretical model A, which may be a reason why incision rates are greatly underestimated even with the parameter combination resulting in the highest modelled incision rate.

The incision of Model A proposed by Fountain and Walder (1998) is based on heat dissipation. The energy produced by the turbulent water flow and the friction at the ice-water interface is assumed to be directly responsible to melt the ice and downcutting the channel. Combining the measured hydraulic slope of 0.053 with the Manning's roughness coefficient of 0.01 s $m^{-1/3}$, a vertical incision rate of ~1 cm day^{-1} is estimated. Comparing this to the measured vertical incision rate of ~4 cm day^{-1}, model A clearly underestimated vertical incision. It does not include the melt capacity through the temperature difference between the stream water to ice (ΔT). The significant underestimation of the incision with this model makes clear that heat dissipation is not the only driver of incision.

Table 13: Resulting incision rates and cumulative incision using different roughness coefficients ñ in the model FW. The timespan for the cumulative incision is 41 days.

ñ	incision rate [cm day^{-1}]	cumulative incision [m]
0.01	1.007	0.422
0.015	0.865	0.363
0.02	0.777	0.326
0.025	0.714	0.299

Theoretical Incision Based on Model B

The ice incision based on the total heat flux corresponds to formula (10). The model is composed by the Nusselt number, representing the energy emitted by the turbulent flux, and the temperature difference between the water and the ice and is dependent on the length scale on which the heat flux occurs λ. As there were no measurements made of the t λ, this parameter had to be estimated. Based on photographs and water level measurements, λ was estimated to be between 0.5 m and 1 m. Due to the high uncertainty of λ, its sensitivity on the cumulative incision was assessed in Figure 37. Using a λ of 0.6 m or 0.5 m, which corresponds to an incision rate of 7.3 cm day^{-1} or 9.7 m, respectively, give reasonable representations of the measured incision rate of the NE-facing channel (7.4 cm day^{-1}) and NW-facing channel (9.4 cm day^{-1}). It becomes clear that the incision is highly influenced by λ and without exact measurements of the wetted perimeter, there are large uncertainties already with small variations. Without the incision measurements done in the cross-sections, it would be hard to estimate incision rates from the theoretical model B. Furthermore, it was assumed that the length scale on which heat flux occurs in the channel corresponds to the wetted perimeter. However, these two parameters may also differ (Sommers and Rajaram, 2020).

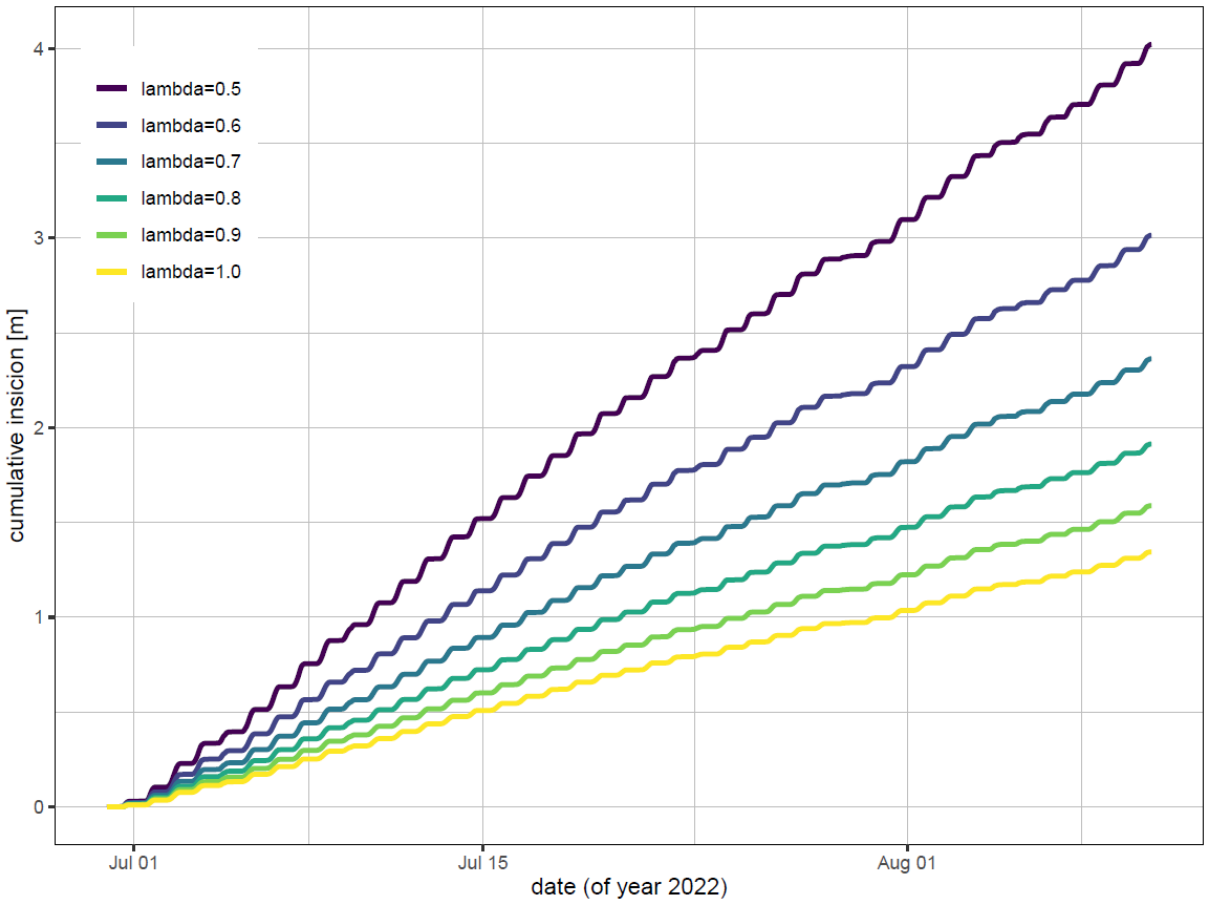

Figure 37: The modelled cumulative incision from the modelled discharge using the model proposed by Ogier et al. (2021) using different λ in 0.1 m steps.

Table 14: Resulting incision rates and cumulative incision with different λ from the model Ogier. The timespan for the cumulative incision is 41 days.

λ [m]	incision rate [cm day^{-1}]	cumulative incision [m]
0.5	9.479	3.973
0.6	7.107	2.979
0.7	5.570	2.335
0.8	4.511	1.891
0.9	3.745	1.570
1.0	3.171	1.329

5.3.2 Ice Cliff Backwasting

Vertical ablation on ice cliffs is about 1.5 to 2 times as high as ablation under the debris cover. Ablation perpendicular to the ice cliff surface is up to 3 times as high as sub-debris melt. However, melt rates on ice cliffs in other studies are found to be 10 to 20 times higher than on debris-covered surfaces (Buri *et al.*, 2021; Miles *et al.*, 2022). Therefore, the melt rate at ice cliffs is less elevated than the sub-debris melt rate on Zmuttgletscher compared other glaciers. This could be because ice cliffs are comparably small or because of different radiation angles. Another possible reason is that the investigated area is influenced by the channels and the forming ice cliffs and has therefore already higher sub-debris ablation rates, similarly as found by Sato *et al.* (2021) Further differences may evolve through the different methodologies (aerial remote sensing vs. in situ measurements).

All ice cliffs in the investigated area are adjacent or in proximity of a channel. This suggests that channels are necessary for the ice cliff formation. In general, channel incision and ice cliff backwasting are observed to occur in the same direction, indicating that there is a link between these two processes. The fact that the lower edge of the ice cliff shows similar incision rates confirms the importance of the channel for the ice cliff formation and preservation and suggests, that the ice cliffs may follow the channel undercut.

As found in other studies (Sakai, Nakawo and Fujita, 2002; Buri *et al.*, 2016), the ice cliff aspect strongly influences the shape of the ice cliffs, which can be explained through the importance of direct shortwave radiation on backwasting (Buri *et al.*, 2016). Comparing the two ice cliffs of opposing aspect (Figure 28 and Figure 27) monitored in this thesis, a clear difference is observable. At the cross-section 1 (NE-facing), the upper and lower ice cliff edges are clearly apart from each other and an inclined ice cliff shows a large area prone to backwasting Observing the other NE-facing ice cliffs downstream of the supraglacial channel, ice cliff with even larger areas are detectable. In the field, the amount of water in the channel was observed to increase further downstream. This could indicate that the amount of water in the channel also influences the size of the ice cliff. However, this should be investigated in more detail.

Ice cliffs were also observed to decouple from the channel (Figure 38). In this case, backwasting is the driving process of the ice loss and there is no more influence of the channel undercutting the cliff. Nevertheless, these ice cliffs are still in proximity to the channel or above channel remnants, which corresponds to the finding of (Kneib *et al.*, 2023).

As opposed to the NE-facing ice cliffs, the ice cliff in the cross-section 2 (NW-facing), the ice cliff has a relatively small area of 0-0.3 m (distance from the lower to the upper ice cliff edge) and is rather pointy. It is assumed, that there is no backwasting process on this ice cliff, unlike on the ice cliff in cross-section 1 and the ice cliff forms solely through channel undercutting. As the vertical melt rates of the upper and lower ice cliff were remarkably similar to the surface ablation rates nearby, the ice cliff is assumed to melt away mainly because of vertical ablation and not because of backwasting of the ice cliff area as in cross-section 1.

Between subperiod 2 and 3, the ice cliff in cross-section 2 broke off and formed newly as the horizontal incision of the supraglacial channel went on. This suggests, that if the undercutting continues with a higher rate than the ablation of the ice cliff, the ice cliff becomes increasingly unstable. Eventually, it reaches a point where it can no longer support its own weight, causing it to break off.

5.3.3 Long-Term Evolution of Supraglacial Channels

The meandering of the channel and the ice cliff evolution are visible in Figure 38. Ice cliffs form along the channel. Those oriented towards NE and east show ice cliff areas (similar as in cross-section 1) and form a characteristic ice cliff with a backwasting behaviour. Those cliffs are also detectable from the UAV imagery. Ice cliffs on the left side of the channel are close to the medial moraine, where the terrain is getting steeper. There are also several ice cliffs on the left side of the channel that have decoupled from the channel but are still actively backwasting. Ice cliffs facing north-west develop by channel undercutting solely and do not form an ice cliff face that wastes back (as in cross-section 2). Only few of those ice cliffs are visible from the UAV imagery. However, the channel incising towards the right side indicates that there are additional ice cliffs of the type of cross-section 2. The

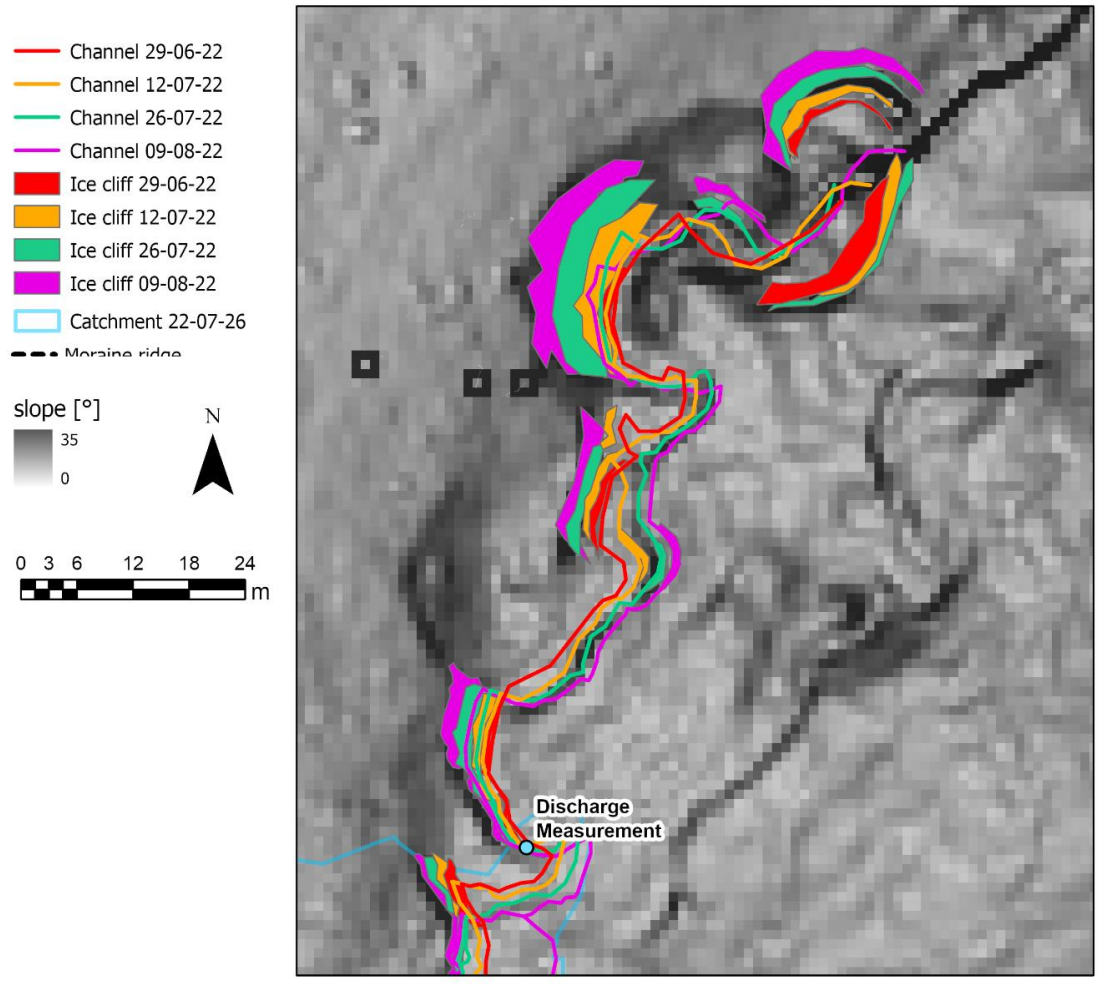

Figure 38: Ice cliff areas and channels were mapped in the orthophotos and are displayed with surface slope. In black, the moraine ridges are mapped.

Therefore, ice cliffs which show a large detectable area are NE and east-facing. This is contrasting to other studies. Buri *et al.* (2021) compared ice cliff area with aspect on different glaciers in High Mountain Asia and found, that there are more ice cliff areas with a NW-facing aspect than with a NE-facing aspect. Sato *et al.* (2021) and Kneib *et al.* (2023) find that ice cliffs in the Himalayas are predominantly north-west facing. Similarly as on Zmuttgletscher, the other studies detected only

few ice cliffs facing south. There are no systematic investigations on ice cliff orientation on debris-covered glaciers in the Alps so far. However, the different aspect found on cliffs on Zmuttgletscher may be explained by the steepness of the surface as the channel is approaching the moraine. The formation of the ice cliff may also be related to the steepness of the surface, which was higher on the left side of the channel than on the right, as debris stability is related to surface steepness (Moore, 2018). This would match the observations of the ice cliff on the orographic left side being in steeper terrain than the ice cliffs on the right side.

On Zmuttgletscher, a supraglacial valley confined by two medial moraines evolved. Within this supraglacial valley, a supraglacial channel surrounded by ice cliffs is observable. This morphology is also observed on other debris-covered glaciers (Kneib *et al.*, 2023; Sato *et al.*, 2021) and on Zmuttgletscher in an earlier study (Mölg *et al.*, 2020). Most of the ice cliffs are found within the supraglacial valley, which coincides with the presence of the supraglacial channel.

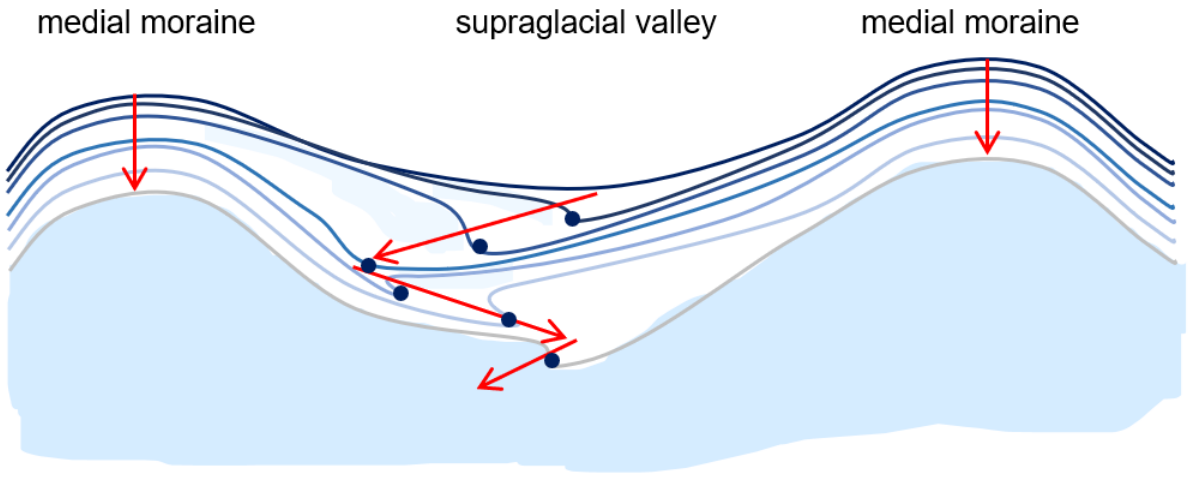

Figure 39: Schematic illustration of the ablation and the additional ice loss through the channel acting as a wiper in the supraglacial valley undercutting the ice and creating the ice cliff. With a dark blue dot, the channel position is marked. For a better readability, the debris cover is not displayed.

The channels are incising sideways and the ice cliffs are following. While in cross-section 1 the channel incises to the orographic left side, the slope is getting steeper as it is approaching the medial moraine. Hence, the ice cliff area is getting larger and its surface steeper (Figure 27). It is possible that as soon as the slope is too steep, debris will cover it and the channel cannot incise further towards the moraine. Subsequently, the channel starts incising in the other direction and the ice cliff detaches from the stream. Through the incision in the other direction, the surface within the supraglacial valley gets eroded (Figure 39). Mölg *et al.* 2020 suggest that through local meltwater accumulation, the supraglacial valley was formed in the first place. As the channel incision continues, a complex channel system with ice cliffs is formed , which preserves the valley (Mölg *et al.*, 2020; Kneib *et al.*, 2023).

6 Conclusion

In this thesis, an area-averaged ETIM calibrated against ablation measurements at stakes was applied to represent the diurnal variations in the ablation rates and cumulative ablation on the debris-covered Zmuttgletscher. Based on the ETIM, the total meltwater input was constrained within a supraglacial catchment. The modelled discharge was corrected with the measured discharge. With two different models, the theoretical vertical channel incision was estimated using the corrected discharge. Incision model A clearly underestimates the vertical incision, as it is only based on heat dissipation and therefore ignores the fact that additional melt energy is available from the temperature difference between the meltwater and ice, as it is incorporated in model 2. With model B, which additionally includes the temperature difference between the stream water and ice, uncertainties are high due to the high sensitivity of the length scale on which the heat is transferred (λ). If λ is between 0.5 m and 0.6 m – which is likely – the model reasonably estimates the channel to incise with a rate of 7.3-9.7 cm day^{-1}. Even small alterations of the wetted perimeter result in great differences in the incision rate and thus, systematic measurements are needed to decrease the uncertainty of the model.

The modelled theoretical incision is compared to the incision and backwasting measured in two cross-sections, where the incision rate is 7.4 and 9.4 cm day^{-1} for a channel at a NE-facing ice cliff and for a channel at a NW-facing ice cliff, respectively. The ratio between the vertical and horizontal incision rate components remains uniform over time within the same ice cliff, namely 1:1.5 in the cross-section 1 with the NE-facing ice cliff and 1:2 in cross-section 2 with the NW-facing ice cliff. The horizontal incision rate component is 1.5 to 2 larger when the channel undercuts the ice cliff. In cross-section 1, the ice cliff has an inclined area that wastes back with a similar rate as the channel incision, which suggests that the ice cliff follows the channel incision. In cross-section 2, the ice cliff does not show the same backwasting area but is formed by channel undercutting and the ice cliff melts away through surface ablation. Ice cliffs of similar aspects as the ones from the investigated surfaces have been observed to show similar shapes, respectively. Independent from the aspect, ice cliffs are found mostly at the supraglacial channel or in proximity, indicating that supraglacial channels are essential for the formation of ice cliffs on Zmuttgletscher. Furthermore, the aspect of the ice cliff seems to be decisive for the ice cliff formation. Therefore, it is suggested that the ratio of the vertical to the horizontal incision rate component is dependent on the discharge and the aspect of the cross-section, i.e. on the aspect of the ice cliff of the cross-section.

The following research questions were answered in this thesis:

Can supraglacial discharge be modelled based on an enhanced temperature-index glacier melt model (ETIM)?
To answer this question, in a first step, an ETIM had to be calibrated against ablation stakes. Analysing the sensitivities and comparing it to other studies, the modelled ablation seems to be a good representation of the actual ablation including diurnal variations within the catchment. On the basis of the ETIM, diurnal variations can be well modelled as observed in the measured discharge. The ablation modelled by the ETIM, but also measured at the stakes, which shows lower rates at night than during the day, seems to have a direct influence in the discharge. However, the determination of a supraglacial catchment on the basis of a DEM and calibration of the modelled discharge to the measured discharge is necessary to reasonably model discharge peaks.

How does the diurnal supraglacial discharge vary and how is it related to the incision?
Clear diurnal patterns are visible in all subperiods in the discharge with minima in the early morning of 0.5 l s^{-1} and maxima in the late afternoon of around 11-13 l s^{-1}. The discharge pattern remains similar over the entire period. The modelled discharge was calibrated against the measured discharge and used as a basis to model supraglacial channel incision rates. As discharge is observed and modelled to be higher during the day, a corresponding increased incision is anticipated with a higher discharge. Hence, most of the incision is expected to occur during the day and only an almost negligible part of the incision should occur at night. However, further investigations are needed to model incision from supraglacial discharge on debris covered glaciers.

Is there a connection between supraglacial channel incision and ice cliff backwasting?
Ice cliffs have been observed to follow the channel incisions. The channel undercut the ice with an incision, which is higher than the ablation rate and 1.5-2 times stronger in horizontal than in vertical direction. Hence, ice cliffs are formed, which backwaste at a similar, even though not equal, rate as the incision occurs. It appears that channel incision dictates backwasting of the ice cliffs. Ice cliffs were detected along or in close proximity to the supraglacial channel. Therefore, the connection between channel incision and ice cliff backwasting could be confirmed.

7 Acknowledgements

First of all, I want to thank Prof. Dr. Andreas Vieli, who guided me through this thesis, answered my questions, gave useful inputs, took his time for many meetings and guided and assisted in the field. A big thank you also goes to Boris Ouvry for co-supervising me, answering my questions and for working together in the field. I also want to thank Dr. Ilja van Meerveld and Dr. Alessandro Cicoira for taking their time to answer questions. Further thanks go to Flo, Jan, Vanessa and Johannes, who assisted us in the field campaigns on Zmuttgletscher. Thanks also to Jonny, Nici and Jan for proofreading this thesis. At this point I also want to thank my family and friends, who always supported me throughout my studies and this thesis.

8 Literature

Anderson, L.S. *et al.* (2021) 'The Causes of Debris-Covered Glacier Thinning: Evidence for the Importance of Ice Dynamics From Kennicott Glacier, Alaska', *Frontiers in Earth Science*, 9, p. 680995. Available at: https://doi.org/10.3389/feart.2021.680995.

Anderson, L.S. and Anderson, R.S. (2016) 'Modeling debris-covered glaciers: response to steady debris deposition', *The Cryosphere*, 10(3), pp. 1105–1124. Available at: https://doi.org/10.5194/tc-10-1105-2016.

Bolch, T., Pieczonka, T. and Benn, D.I. (2011) 'Multi-decadal mass loss of glaciers in the Everest area (Nepal Himalaya) derived from stereo imagery', *The Cryosphere*, 5(2), pp. 349–358. Available at: https://doi.org/10.5194/tc-5-349-2011.

Brook, M., Hagg, W. and Winkler, S. (2013) 'Debris cover and surface melt at a temperate maritime alpine glacier: Franz Josef Glacier, New Zealand', *New Zealand Journal of Geology and Geophysics*, 56(1), pp. 27–38. Available at: https://doi.org/10.1080/00288306.2012.736391.

Bryn Hubbard and Glasser, Neil (2005) *Field Techniques in Glaciology and Glacial Geomorphology*. John Wiley & Sons.

Buri, P. *et al.* (2016) 'A grid-based model of backwasting of supraglacial ice cliffs on debris-covered glaciers', *Annals of Glaciology*, 57(71), pp. 199–211. Available at: https://doi.org/10.3189/2016AoG71A059.

Buri, P. *et al.* (2021) 'Supraglacial Ice Cliffs Can Substantially Increase the Mass Loss of Debris-Covered Glaciers', *Geophysical Research Letters*, 48(6). Available at: https://doi.org/10.1029/2020GL092150.

Carenzo, M. *et al.* (2016) 'An enhanced temperature index model for debris-covered glaciers accounting for thickness effect', *Advances in Water Resources*, 94, pp. 457–469. Available at: https://doi.org/10.1016/j.advwatres.2016.05.001.

Church, M. (2006) 'Bed material transport and the morphology of alluvial river channels', *Annual Review of Earth and Planetary Sciences*, 34(1), pp. 325–354. Available at: https://doi.org/10.1146/annurev.earth.33.092203.122721.

Cicoira, A. *et al.* (2019) 'Water controls the seasonal rhythm of rock glacier flow', *Earth and Planetary Science Letters*, 528, p. 115844. Available at: https://doi.org/10.1016/j.epsl.2019.115844.

Clarke, G.K.C. (2003) 'Hydraulics of subglacial outburst floods: new insights from the Spring–Hutter formulation', *Journal of Glaciology*, 49(165), pp. 299–313. Available at: https://doi.org/10.3189/172756503781830728.

Collier, C.G. (2016) *Hydrometeorology*. Chichester, West Sussex, United Kingdom: Wiley Blackwell.

Compagno, L. *et al.* (2022) 'Modelling supraglacial debris-cover evolution from the single-glacier to the regional scale: an application to High Mountain Asia', *The Cryosphere*, 16(5), pp. 1697–1718. Available at: https://doi.org/10.5194/tc-16-1697-2022.

Day, T.J. (1977) 'Field procedures and evaluation of a slug dilution gauging method in mountain streams', 16(2).

Engineering ToolBox. Manning's Roughness Coefficients. (2004). Available at: https://www.engineeringtoolbox.com/mannings-roughness-d_799.html (Accessed: 20 April 2022).

Evatt, G.W. *et al.* (2015) 'Glacial melt under a porous debris layer', *Journal of Glaciology*, 61(229), pp. 825–836. Available at: https://doi.org/10.3189/2015JoG14J235.

Ferguson, J. and Vieli, A. (2020) *Modelling steady states and the transient response of debris-coveredglaciers*. preprint. Glaciers/Numerical Modelling. Available at: https://doi.org/10.5194/tc-2020-228.

Fountain, A.G. and Walder, J.S. (1998) 'Water flow through temperate glaciers', *Reviews of Geophysics*, 36(3), pp. 299–328. Available at: https://doi.org/10.1029/97RG03579.

Fyffe, C.L. *et al.* (2014) 'A distributed energy-balance melt model of an alpine debris-covered glacier', *Journal of Glaciology*, 60(221), pp. 587–602. Available at: https://doi.org/10.3189/2014JoG13J148.

Gabbi, J. *et al.* (2014) 'A comparison of empirical and physically based glacier surface melt models for long-term simulations of glacier response', *Journal of Glaciology*, 60(224), pp. 1140–1154. Available at: https://doi.org/10.3189/2014JoG14J011.

Gardelle, J. *et al.* (2013) 'Region-wide glacier mass balances over the Pamir-Karakoram-Himalaya during 1999–2011', *The Cryosphere*, 7(4), pp. 1263–1286. Available at: https://doi.org/10.5194/tc-7-1263-2013.

'Global Glacier Change Bulletin No. 4 (2018-2019)' (no date).

Groos, A.R. *et al.* (2017) 'A first attempt to model region-wide glacier surface mass balances in the Karakoram: findings and future challenges', *Geografia Fisica e Dinamica Quaternaria*, (40), pp. 137–159. Available at: https://doi.org/10.4461/GFDQ.2017.40.10.

Hagg, W. *et al.* (2008) 'Sub-debris melt rates on southern inylchek glacier, central tian shan', *Geografiska Annaler: Series A, Physical Geography*, 90(1), pp. 55–63. Available at: https://doi.org/10.1111/j.1468-0459.2008.00333.x.

Hardmeier, F. (no date) 'Modelling climate sensitivity of debris-covered glaciers'.

Herreid, S. and Pellicciotti, F. (2020) 'The state of rock debris covering Earth's glaciers', *Nature Geoscience*, 13(9), pp. 621–627. Available at: https://doi.org/10.1038/s41561-020-0615-0.

Hock, R. (2003) 'Temperature index melt modelling in mountain areas', *Journal of Hydrology*, 282(1–4), pp. 104–115. Available at: https://doi.org/10.1016/S0022-1694(03)00257-9.

Hock, R. *et al.* (2019) 'GlacierMIP – A model intercomparison of global-scale glacier mass-balance models and projections', *Journal of Glaciology*, 65(251), pp. 453–467. Available at: https://doi.org/10.1017/jog.2019.22.

Huss, M. and Hock, R. (2018) 'Global-scale hydrological response to future glacier mass loss', *Nature Climate Change*, 8(2), pp. 135–140. Available at: https://doi.org/10.1038/s41558-017-0049-x.

Kääb, A. *et al.* (2012) 'Contrasting patterns of early twenty-first-century glacier mass change in the Himalayas', *Nature*, 488(7412), pp. 495–498. Available at: https://doi.org/10.1038/nature11324.

King, O. *et al.* (2020) 'Morphometric evolution of Everest region debris-covered glaciers', *Geomorphology*, 371, p. 107422. Available at: https://doi.org/10.1016/j.geomorph.2020.107422.

Kneib, M., Miles, E. S., *et al.* (2021) 'Interannual Dynamics of Ice Cliff Populations on Debris-Covered Glaciers From Remote Sensing Observations and Stochastic Modeling', *Journal of Geophysical Research: Earth Surface*, 126(10). Available at: https://doi.org/10.1029/2021JF006179.

Kneib, M., Miles, E.S., *et al.* (2021) 'Mapping ice cliffs on debris-covered glaciers using multispectral satellite images', *Remote Sensing of Environment*, 253, p. 112201. Available at: https://doi.org/10.1016/j.rse.2020.112201.

Kneib, M. *et al.* (2023) 'Controls on Ice Cliff Distribution and Characteristics on Debris-Covered Glaciers', *Geophysical Research Letters*, 50(6), p. e2022GL102444. Available at: https://doi.org/10.1029/2022GL102444.

Lambrecht, A. *et al.* (2011) 'A comparison of glacier melt on debris-covered glaciers in the northern and southern Caucasus', *The Cryosphere*, 5(3), pp. 525–538. Available at: https://doi.org/10.5194/tc-5-525-2011.

Mihalcea, C. *et al.* (2006) 'Ice ablation and meteorological conditions on the debris-covered area of Baltoro glacier, Karakoram, Pakistan', *Annals of Glaciology*, 43, pp. 292–300. Available at: https://doi.org/10.3189/172756406781812104.

Mihalcea, C. *et al.* (2008) 'Spatial distribution of debris thickness and melting from remote-sensing and meteorological data, at debris-covered Baltoro glacier, Karakoram, Pakistan', *Annals of Glaciology*, 48, pp. 49–57. Available at: https://doi.org/10.3189/172756408784700680.

Miles, E.S. *et al.* (2022) 'Controls on the relative melt rates of debris-covered glacier surfaces', *Environmental Research Letters*, 17(6), p. 064004. Available at: https://doi.org/10.1088/1748-9326/ac6966.

Mölg, N. *et al.* (2019) *The role of debris cover in the evolution of Zmuttgletscher, Switzerland, since the end of the Little Ice Age*. preprint. Glaciers/Alpine Glaciers. Available at: https://doi.org/10.5194/tc-2018-292.

Mölg, N. *et al.* (2020) 'On the influence of debris cover on glacier morphology: How high-relief structures evolve from smooth surfaces', *Geomorphology*, 357, p. 107092. Available at: https://doi.org/10.1016/j.geomorph.2020.107092.

Moore, P.L. (2018) 'Stability of supraglacial debris', *Earth Surface Processes and Landforms*, 43(1), pp. 285–297. Available at: https://doi.org/10.1002/esp.4244.

Nicholson, L. *et al.* (2021) 'The Challenge of Non-Stationary Feedbacks in Modeling the Response of Debris-Covered Glaciers to Climate Forcing', *Frontiers in Earth Science*, 9, p. 662695. Available at: https://doi.org/10.3389/feart.2021.662695.

Nicholson, L. and Benn, D.I. (2006) 'Calculating ice melt beneath a debris layer using meteorological data', *Journal of Glaciology*, 52(178), pp. 463–470. Available at: https://doi.org/10.3189/172756506781828584.

Nicholson, L. and Benn, D.I. (2013) 'Properties of natural supraglacial debris in relation to modelling sub-debris ice ablation: PROPERTIES OF SUPRAGLACIAL DEBRIS', *Earth Surface Processes and Landforms*, 38(5), pp. 490–501. Available at: https://doi.org/10.1002/esp.3299.

Ogier, C. *et al.* (2021) 'Drainage of an ice-dammed lake through a supraglacial stream: hydraulics and thermodynamics', *The Cryosphere*, 15(11), pp. 5133–5150. Available at: https://doi.org/10.5194/tc-15-5133-2021.

Pellicciotti, F. *et al.* (2005) 'An enhanced temperature-index glacier melt model including the shortwave radiation balance: development and testing for Haut Glacier d'Arolla, Switzerland', *Journal of Glaciology*, 51(175), pp. 573–587. Available at: https://doi.org/10.3189/172756505781829124.

Pitcher, L.H. and Smith, L.C. (2019) 'Supraglacial Streams and Rivers', *Annual Review of Earth and Planetary Sciences*, 47(1), pp. 421–452. Available at: https://doi.org/10.1146/annurev-earth-053018-060212.

Reid, T.D. and Brock, B.W. (2010) 'An energy-balance model for debris-covered glaciers including heat conduction through the debris layer', *Journal of Glaciology*, 56(199), pp. 903–916. Available at: https://doi.org/10.3189/002214310794457218.

Reid, T.D. and Brock, B.W. (2014) 'Assessing ice-cliff backwasting and its contribution to total ablation of debris-covered Miage glacier, Mont Blanc massif, Italy', *Journal of Glaciology*, 60(219), pp. 3–13. Available at: https://doi.org/10.3189/2014JoG13J045.

Richardson, J.M. and Brook, M.S. (2010) 'Ablation of debris-covered ice: some effects of the 25 September 2007 Mt Ruapehu eruption', *Journal of the Royal Society of New Zealand*, 40(2), pp. 45–55. Available at: https://doi.org/10.1080/03036758.2010.494714.

Röhl, K. (2008) 'Characteristics and evolution of supraglacial ponds on debris-covered Tasman Glacier, New Zealand', *Journal of Glaciology*, 54(188), pp. 867–880. Available at: https://doi.org/10.3189/002214308787779861.

Sakai, A., Nakawo, M. and Fujita, K. (2002) 'Distribution Characteristics and Energy Balance of Ice Cliffs on Debris-covered Glaciers, Nepal Himalaya', *Arctic, Antarctic, and Alpine Research*, 34(1), pp. 12–19. Available at: https://doi.org/10.1080/15230430.2002.12003463.

Sato, Y. *et al.* (2021) 'Ice Cliff Dynamics of Debris-Covered Trakarding Glacier in the Rolwaling Region, Nepal Himalaya', *Frontiers in Earth Science*, 9, p. 623623. Available at: https://doi.org/10.3389/feart.2021.623623.

Scherler, D., Wulf, H. and Gorelick, N. (2018) 'Global Assessment of Supraglacial Debris-Cover Extents', *Geophysical Research Letters*, 45(21), p. 11,798-11,805. Available at: https://doi.org/10.1029/2018GL080158.

Smith, L.C. *et al.* (2015) 'Efficient meltwater drainage through supraglacial streams and rivers on the southwest Greenland ice sheet', *Proceedings of the National Academy of Sciences*, 112(4), pp. 1001–1006. Available at: https://doi.org/10.1073/pnas.1413024112.

Sommers, A.N. and Rajaram, H. (2020) 'Energy Transfer by Turbulent Dissipation in Glacial Conduits', *Journal of Geophysical Research: Earth Surface*, 125(10). Available at: https://doi.org/10.1029/2019JF005502.

Steiner, J.F. *et al.* (2015) 'Modelling ice-cliff backwasting on a debris-covered glacier in the Nepalese Himalaya', *Journal of Glaciology*, 61(229), pp. 889–907. Available at: https://doi.org/10.3189/2015JoG14J194.

Swisstopo (2023) *Bundesamt für Landestopographie*. Available at: https://map.geo.admin.ch.

Zemp, M. *et al.* (2019) 'Global glacier mass changes and their contributions to sea-level rise from 1961 to 2016', *Nature*, 568(7752), pp. 382–386. Available at: https://doi.org/10.1038/s41586-019-1071-0.

9 Appendix

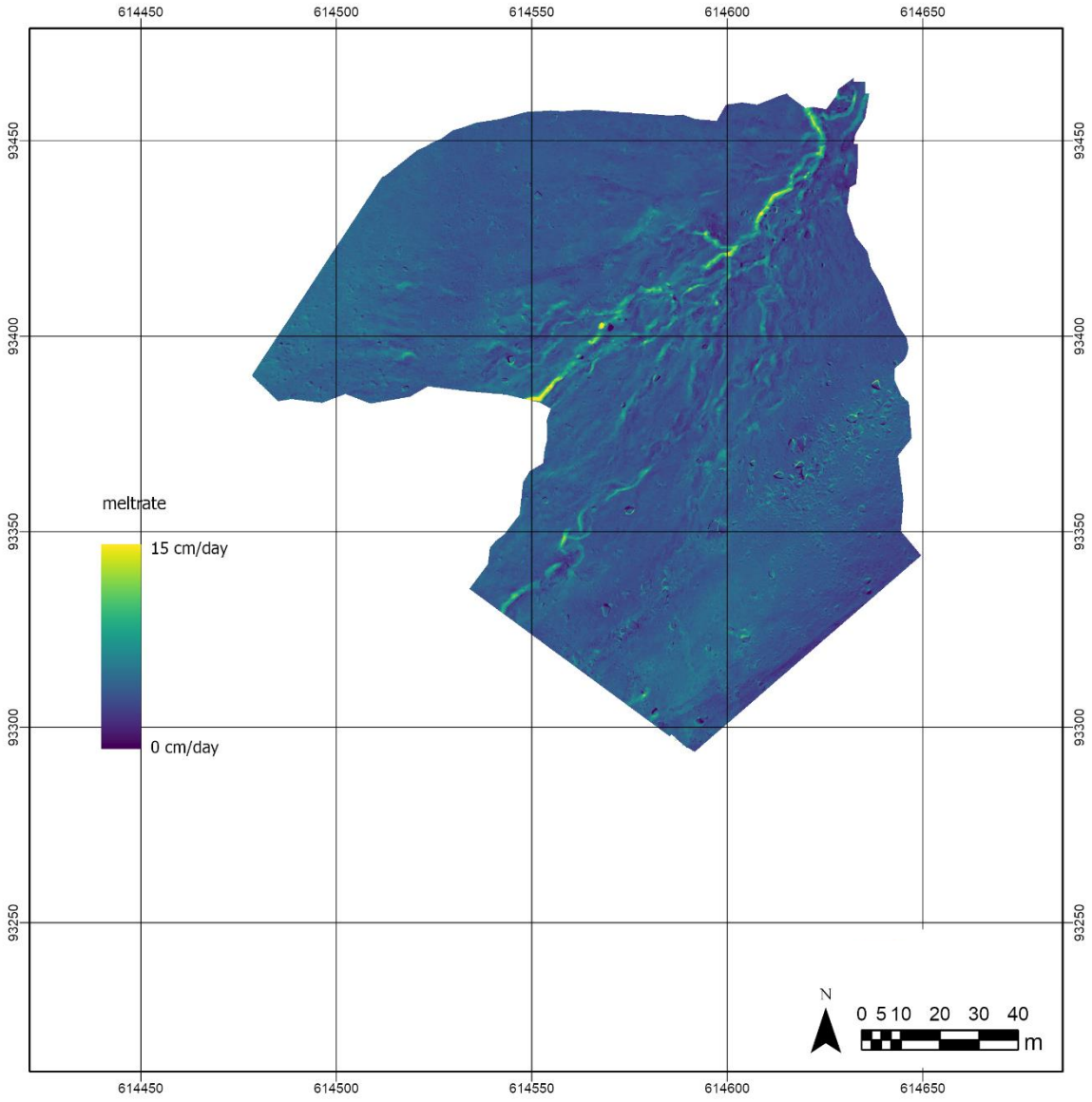

Appendix I: Surface elevation loss on the catchment between June 29 and July 12.

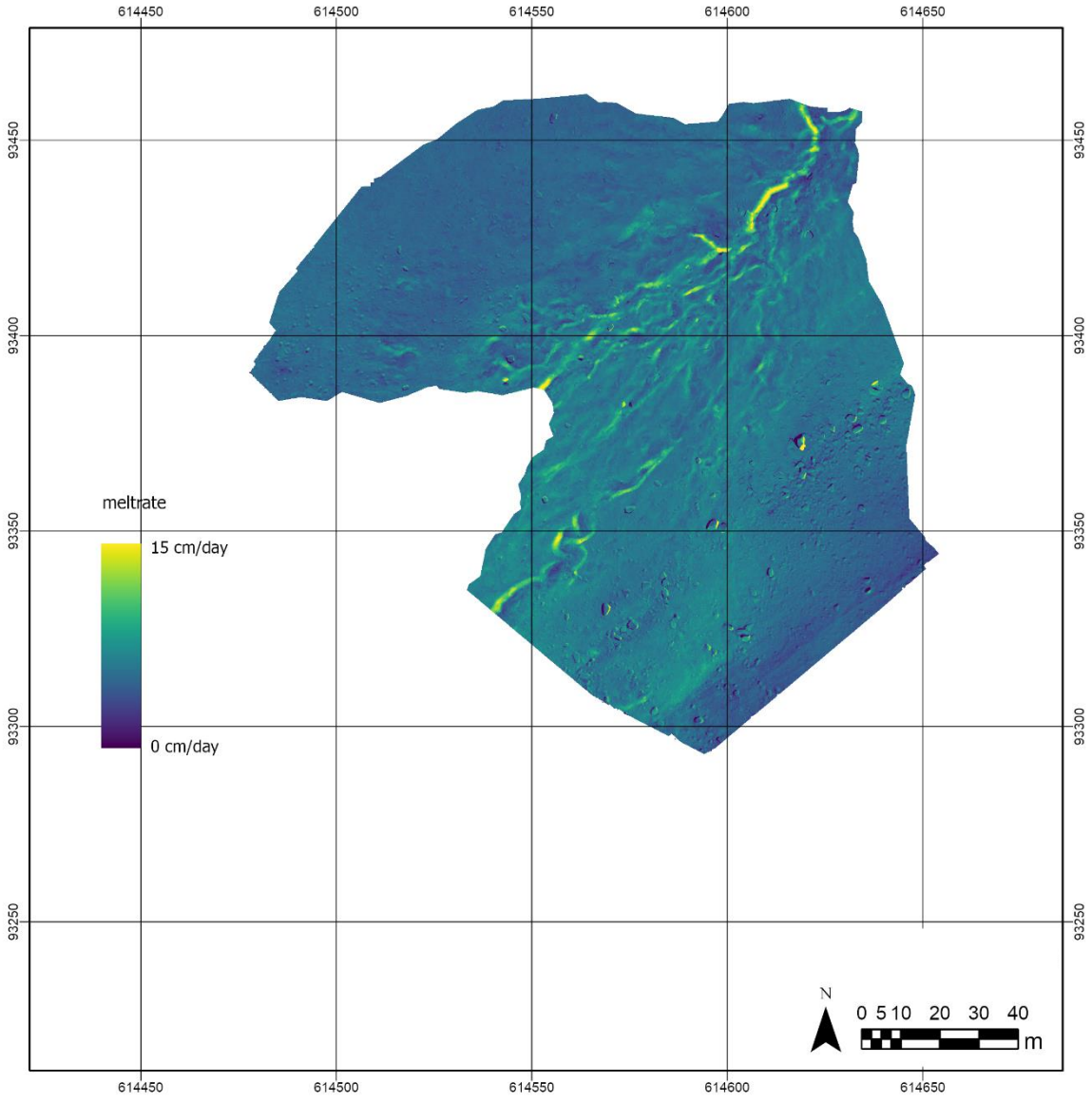

Appendix II: Surface elevation loss on the catchment between July 12 and July 26.

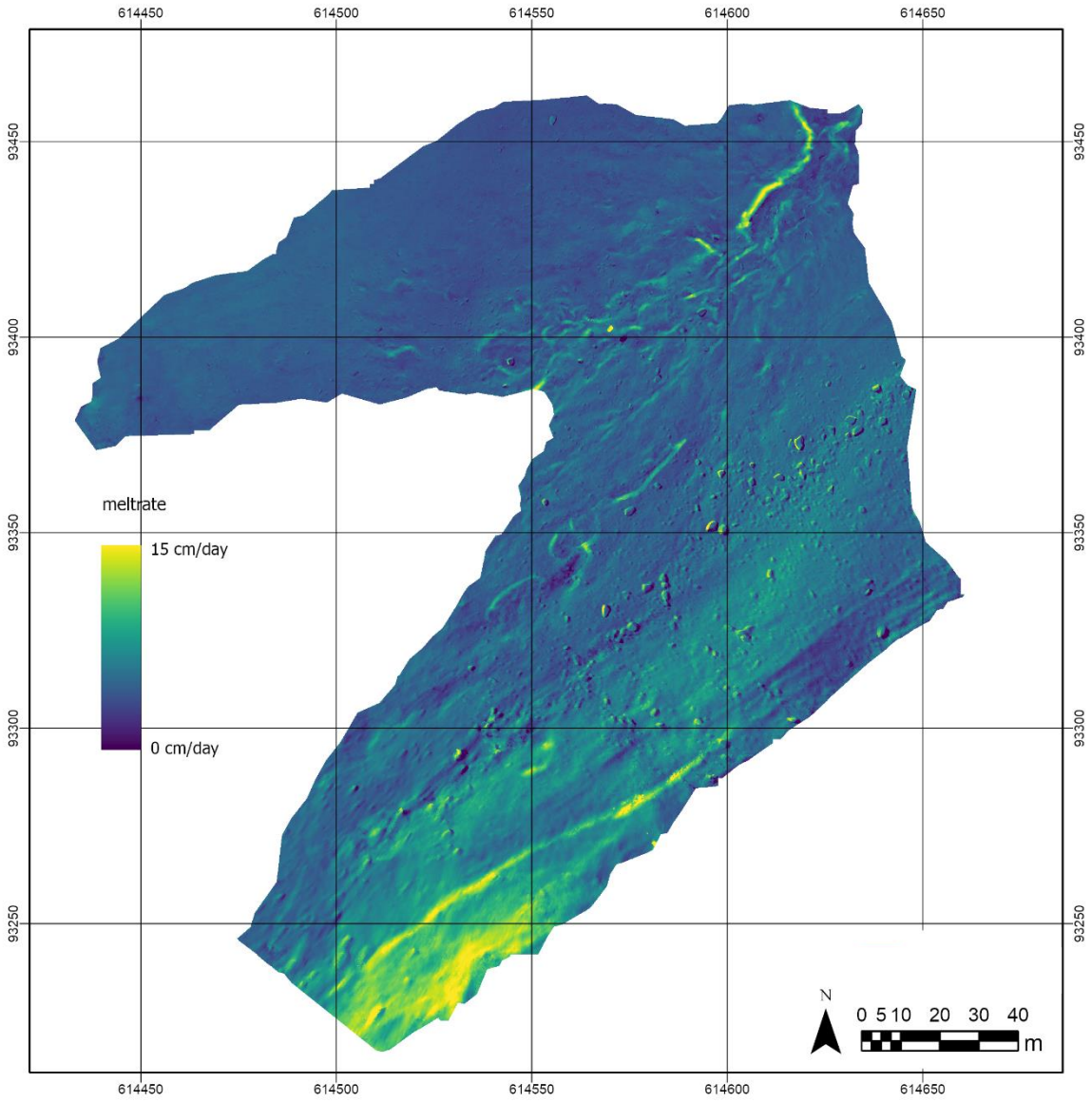

Appendix III: Surface elevation loss on the catchment between July 26 and August 09.

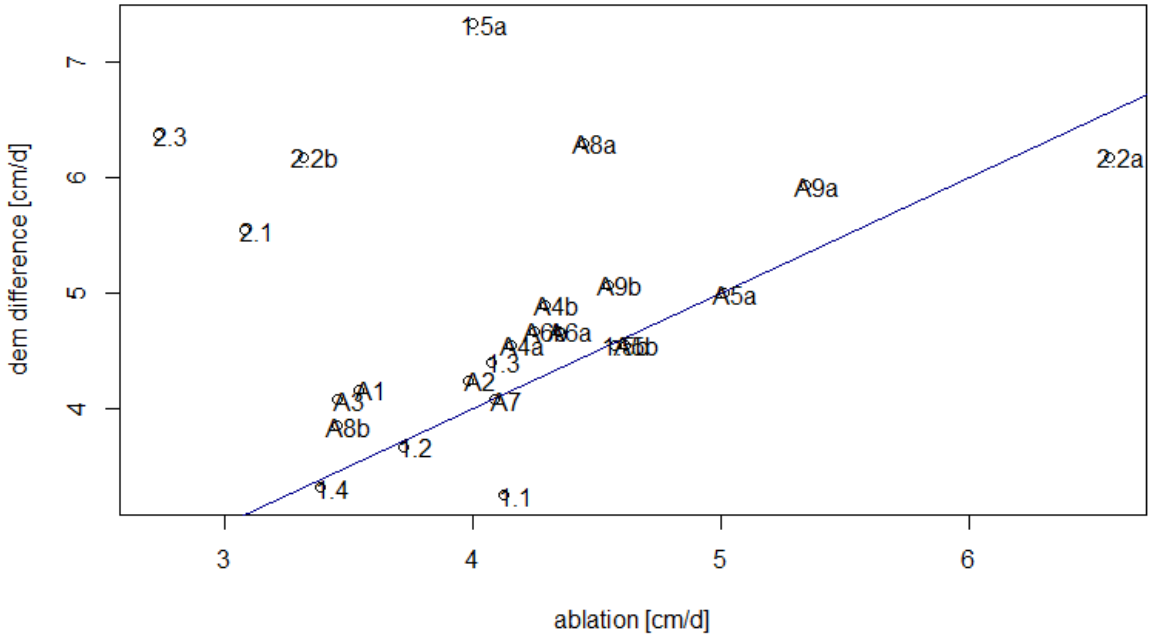

Appendix IV: DEM difference at the stakes plotted against the ablation measured at the stakes.

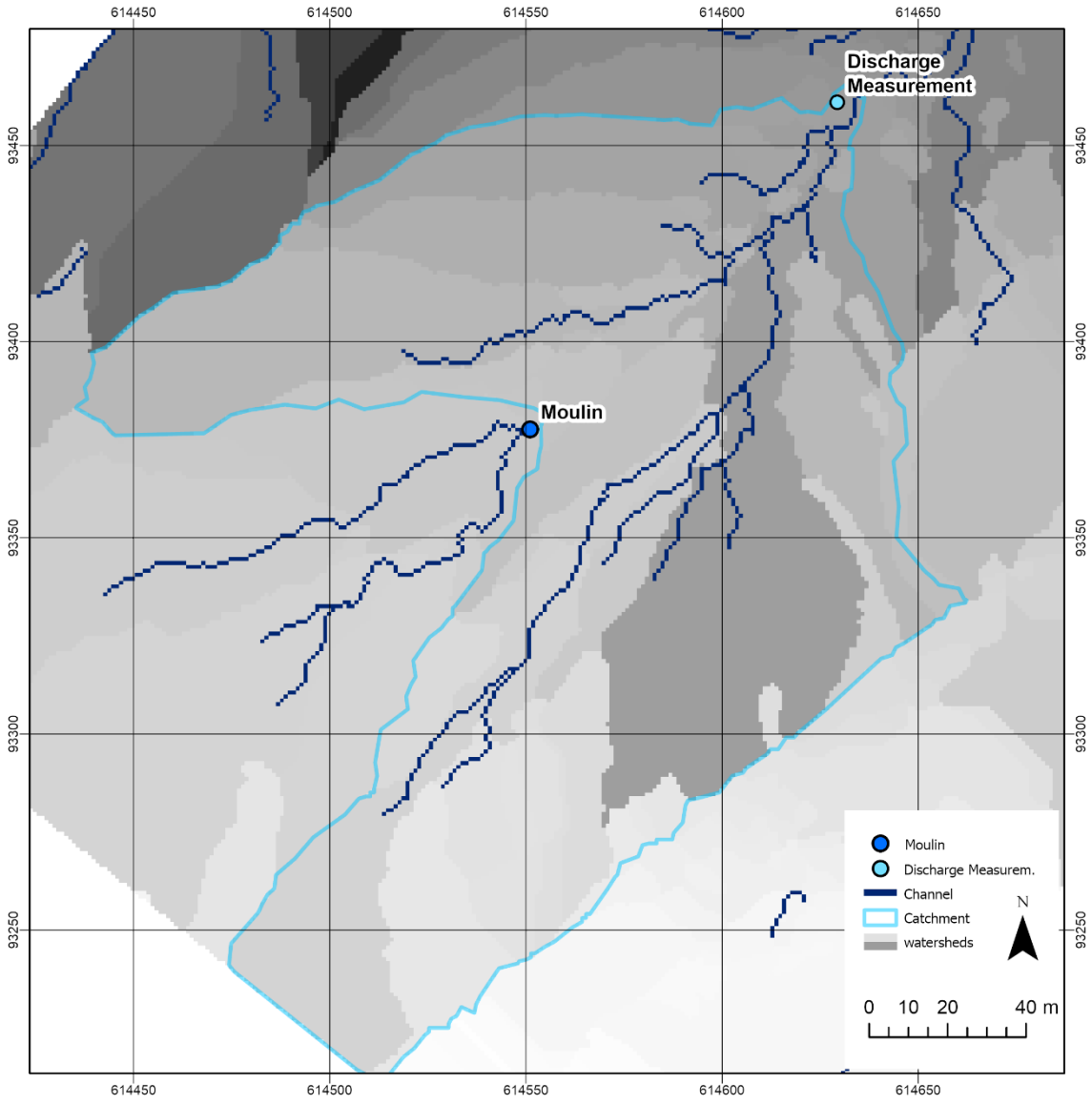

Appendix V: Catchment defined from the DEM of August 09. The catchment area is 27182 m² in comparison to the catchment area used from the DEM of July 26 of 27592 m².

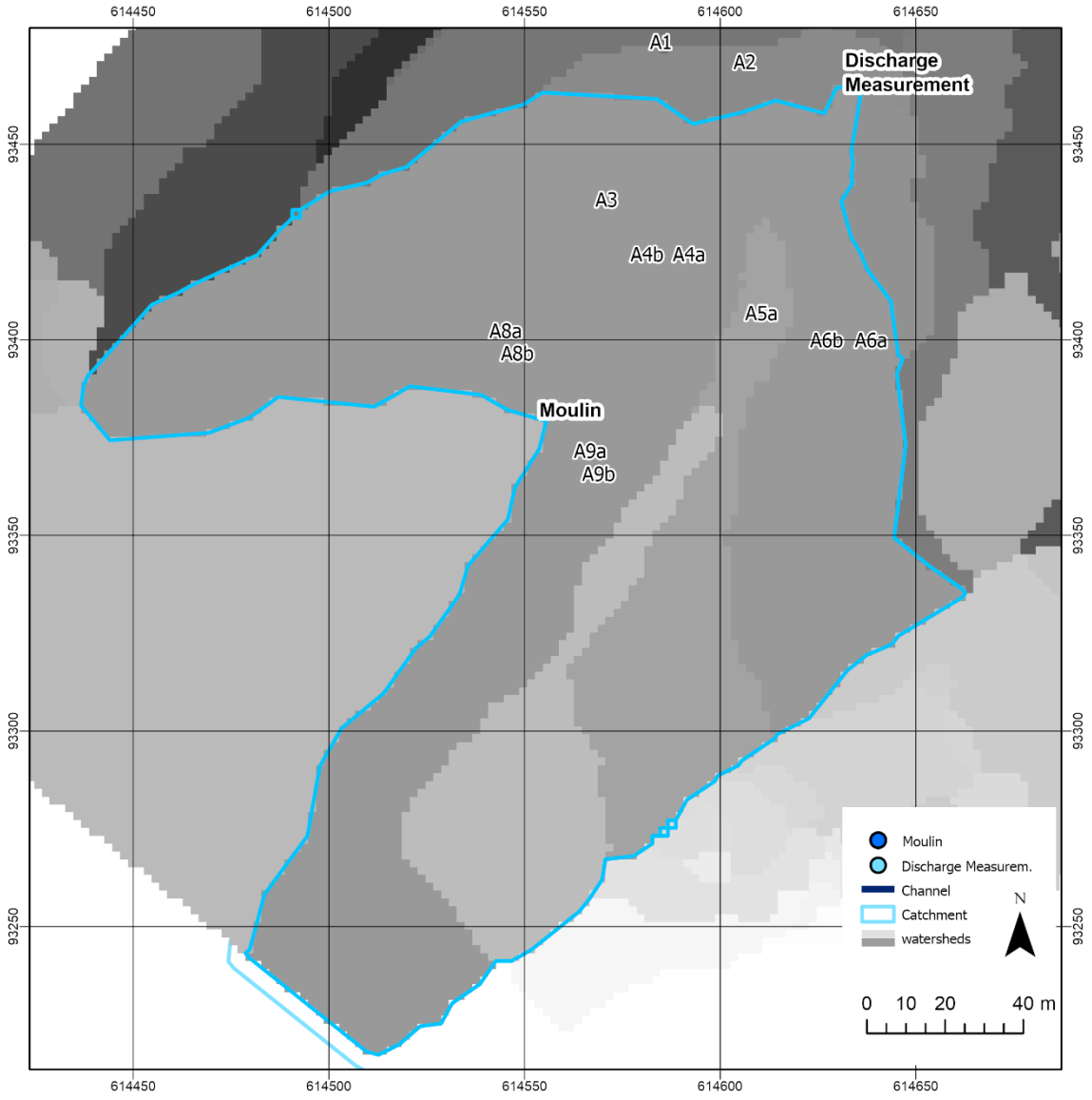

Appendix VI: Catchment defined from the DEM of August 09. The catchment area is 27532 m² in comparison to the catchment area used from the DEM of July 26 of 27592 m².

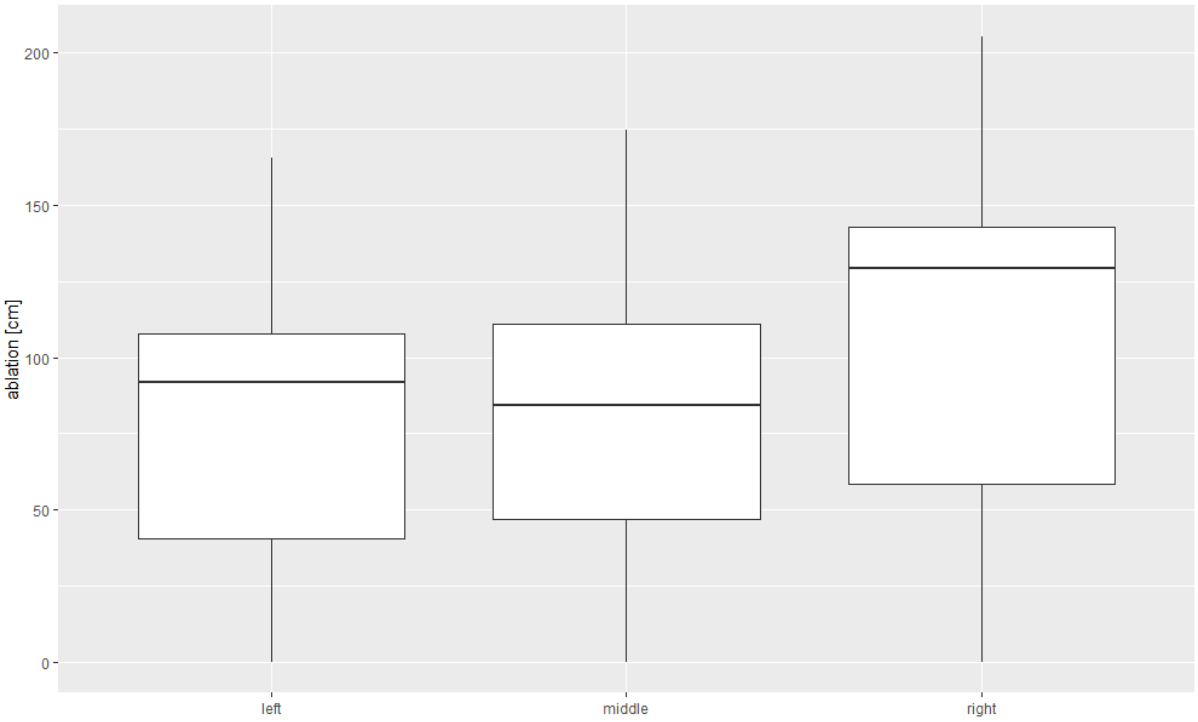

Appendix VII: ablation by location of the ablation stake within the catchment. "Middle" is the area around the channel.

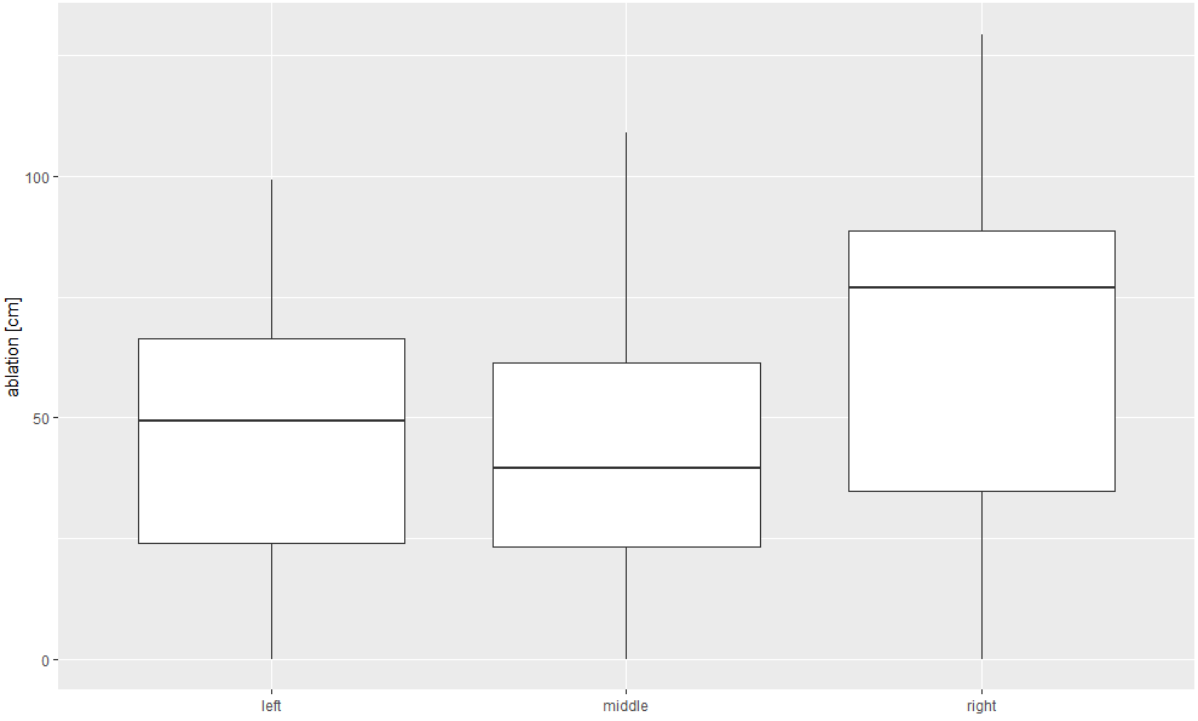

Appendix VIII: ablation by location in catchment (corrected for Fins of respective stakes). "Middle" is the area around the channel.

date	time	summed conductivity [µS]	m	q	tracer volume [ml]	salt concentration [ ]	discharge [l/s]
22-06-30	07:30	58221.52	3.13E-05	-0.0029	5000	1.818	2.747
22-06-30	12:30	5263.79	3.45E-05	-0.0019	5000	0.180	27.782
22-07-12	08:00	111442	1.71E-05	-0.0023	2000	1.900	1.050
22-07-12	10:15	15648.73	3.45E-05	-0.0054	5000	0.535	9.336
22-07-12	12:00	14388.98	3.45E-05	-0.0023	5000	0.495	10.102
22-07-12	14:00	11999.93	3.70E-05	-0.0039	5000	0.440	11.370
22-07-12	16:00	13875.73	3.09E-05	-0.0023	5000	0.426	11.740
22-07-12	18:00	14881.08	3.05E-05	-0.0023	5000	0.452	11.071
22-07-26	08:15	32432.76	3.24E-05	-0.0039	2000	1.046	1.908
22-07-26	10:15	27978.4	2.69E-05	-0.0046	5000	0.749	6.670
22-07-27	15:15	4985	5.67E-05	-0.0022	5000	0.280	17.827
22-07-27	17:00	8190	6.25E-05	-0.0024	5000	0.509	9.814
22-07-27	18:45	8492.5	6.52E-05	-0.0034	5000	0.550	9.080
22-07-28	08:00	23785	5.20E-05	-0.0027	2000	1.233	1.619
22-08-09	10:30	11024.89	5.23E-05	-0.004	5000	0.573	8.721
22-08-09	12:00	13154.96	3.76E-05	-0.0028	4500	0.492	9.140
22-08-09	14:15	12622.76	3.38E-05	-0.0023	4500	0.424	10.611
22-08-09	16:15	17196.27	3.29E-05	-0.0023	5000	0.563	8.880
22-08-09	18:15	21800.89	3.27E-05	-0.0035	5000	0.709	7.049
22-08-10	09:45	28623.22	3.28E-05	-0.0032	5000	0.937	5.333
22-08-10	17:00	19438.43	3.66E-05	-0.0014	5000	0.710	7.041

Appendix IX: The calibration parameters and the resulting discharges measured on Zmuttgletscher. In grey are the excluded measurements that were done with another device.

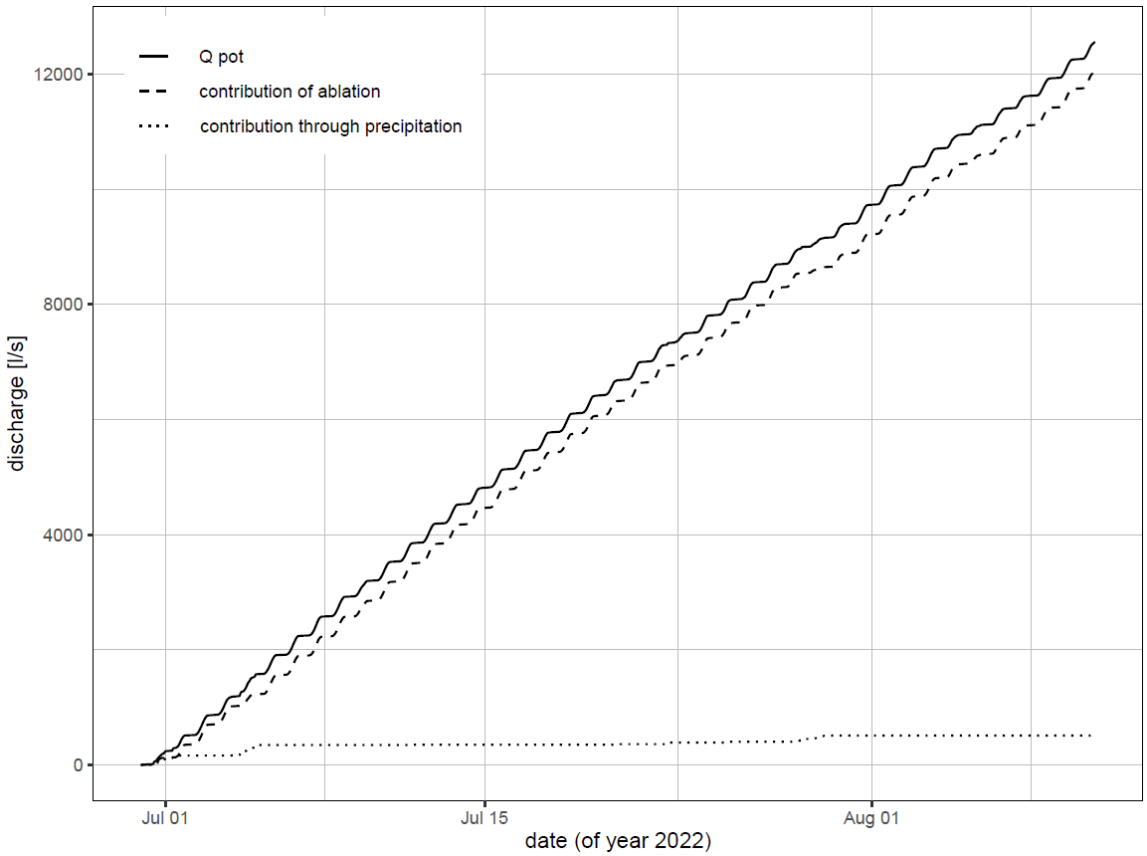

Appendix X: cumulative Q_{pot} and the cumulative discharge components ablation and precipitation.

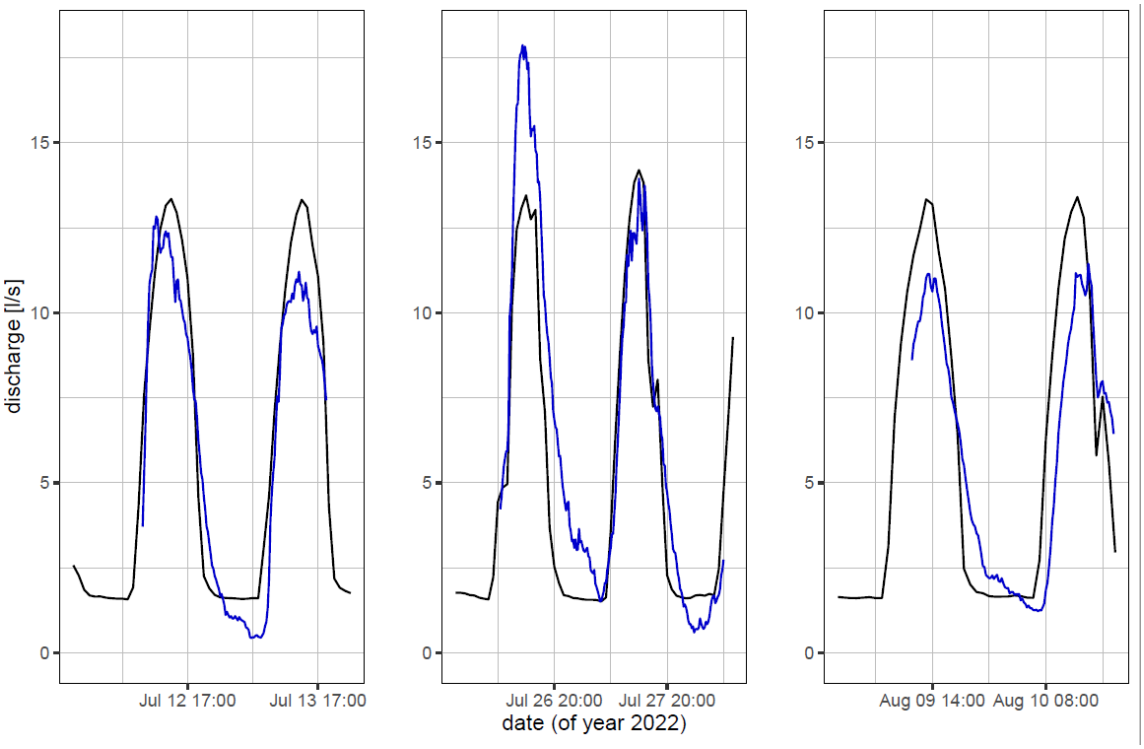

Appendix XI: Modelled (black) and measured (blue) discharge Q_{mod}. For the modelled discharge Q_{mod}+1.25 l/s were used (see Figure 25, Figure 33).

	upper edge				lower edge			
	cumulative		cumulative		cumulative		cumulative	
	Δx [m]	$\dot{x}$ [m]	Δz [m]	$\dot{z}$ [m]	Δx [m]	$\dot{x}$ [m]	Δz [m]	$\dot{z}$ [m]
22-07-12	1	0.077	0.300	0.023	1.000	0.077	0.300	0.023
22-07-26	2.6	0.096	1.400	0.052	2.300	0.085	1.600	0.059
22-08-09	4	0.098	1.900	0.046	3.800	0.093	1.750	0.043

Appendix XII: NW-facing ice cliff backwasting rates from the point cloud cross-section.

	upper edge				lower edge			
	cumulative		cumulative		cumulative		cumulative	
	Δx [m]	$\dot{x}$ [m]	Δx [m]	$\dot{z}$ [m]	Δx [m]	$\dot{x}$ [m]	Δx [m]	$\dot{z}$ [m]
22-07-12	1	0.077	0.600	0.046	1.100	0.085	0.700	0.054
22-07-26	3.3	0.122	0.400	0.015	2.400	0.089	1.300	0.048
22-08-09	5	0.122	0.500	0.012	3.600	0.088	2.100	0.051

Appendix XIII: NE-facing ice cliff backwasting rates from the point cloud cross-section.

Personal Declaration

I hereby declare that the submitted thesis is the result of my own, independent work. All external sources are explicitly acknowledged in the thesis.

Zürich, 2023-06-07 Céline Walker